Layer Structured Gallium Chalcogenides: Controlled Synthesis and Emerging Properties

by

Hui Cai

A Dissertation Presented in Partial Fulfillment
of the Requirements for the Degree
Doctor of Philosophy

Approved June 2018 by the
Graduate Supervisory Committee:

Sefaattin Tongay, Chair
Christian Dwyer
Houlong Zhuang

ARIZONA STATE UNIVERSITY

August 2018

ABSTRACT

Layer structured two dimensional (2D) semiconductors have gained much interest due to their intriguing optical and electronic properties induced by the unique van der Waals bonding between layers. The extraordinary success for graphene and transition metal dichalcogenides (TMDCs) has triggered a constant search for novel 2D semiconductors beyond them. Gallium chalcogenides, belonging to the group III-VI compounds, are a new class of 2D semiconductors that carry a variety of interesting properties including wide spectrum coverage of their bandgaps and thus are promising candidates for next generation electronic and optoelectronic devices. Pushing these materials toward applications requires more controllable synthesis methods and facile routes for engineering their properties on demand.

In this dissertation, vapor phase transport is used to synthesize layer structured gallium chalcogenide nanomaterials with highly controlled structure, morphology and properties, with particular emphasis on GaSe, GaTe and GaSeTe alloys. Multiple routes are used to manipulate the physical properties of these materials including strain engineering, defect engineering and phase engineering. First, 2D GaSe with controlled morphologies is synthesized on Si(111) substrates and the bandgap is significantly reduced from 2 eV to 1.7 eV due to lateral tensile strain. By applying vertical compressive strain using a diamond anvil cell, the band gap can be further reduced to 1.4 eV. Next, pseudo-1D GaTe nanomaterials with a monoclinic structure are synthesized on various substrates. The product exhibits highly anisotropic atomic structure and properties characterized by high-resolution transmission electron microscopy and angle resolved Raman and photoluminescence (PL) spectroscopy. Multiple sharp PL emissions

below the bandgap are found due to defects localized at the edges and grain boundaries. Finally, layer structured $GaSe_{1-x}Te_x$ alloys across the full composition range are synthesized on GaAs(111) substrates. Results show that GaAs(111) substrate plays an essential role in stabilizing the metastable single-phase alloys within the miscibility gaps. A hexagonal to monoclinic phase crossover is observed as the Te content increases. The phase crossover features coexistence of both phases and isotropic to anisotropic structural transition.

Overall, this work provides insights into the controlled synthesis of gallium chalcogenides and opens up new opportunities towards optoelectronic applications that require tunable material properties.

DEDICATION

I dedicate my dissertation to my parents, for their continued emotional support during my PhD

and to my grandparents, for their deep and pure love.

ACKNOWLEDGMENTS

First of all, I would like to give my most sincere gratitude to my advisor Prof. Sefaattin Tongay for giving me the opportunity to pursue my PhD degree under his guidance. I started as a master student working in Prof. Tongay's lab, but he generously recommended me for the PhD program and constantly supported my research thereafter both financially and mentally. Prof. Tongay provided enough flexibility and freedom for me to pursue research projects of my choice and interests, even when we had different opinions on certain projects. Besides supporting my research, Prof. Tongay also served as a role model for me in my pursuit of an academic career. I was always amazed and inspired by his great passion and immense knowledge toward science when we had our discussions. When I was stuck with my research, he also showed infinite patience in guiding me through the difficult times. When it comes to professional development and achieving my career goals, Prof. Tongay offered his immense help in every way possible. Finally, my research relied on both internal and external collaborations established by Prof. Tongay.

I would like to thank Prof. Christian Dwyer for being my defense committee member. The invaluable fundamental insights and advice he provided are of great help toward my research projects. I also thank the final member of my defense committee: Prof. Houlong Zhuang, for our close collaboration on the DFT calculations that helped me gain a deeper understanding for my experimental results.

I would like to thank Dr. Toshihiro Aoki and Prof. Shery L.Y. Chang and Dr. Emmanuel Soignard for being excellent internal collaborators. Dr. Toshihiro Aoki and Prof. Shery L.Y. Chang provided generous help on the TEM measurements and also data

interpretation of our samples. Dr. Emmanuel Soignard offered invaluable assistance on Raman spectroscopy, high pressure setup and XRD experiments.

I would like to extend my gratitude to a number of external collaborators including Prof. Jeffrey Grossman from MIT and his group members for their contribution in DFT calculations, Prof. Xavier Marie and Prof. Bernhard Urbaszek from Université de Toulouse and their group members for their help on low temperature optical properties measurements, Dr. D. Frank Ogletree from Lawrence Berkeley National Laboratory and Dr. Changhyun Ko from University of California, Berkeley for their help on nano-Auger spectroscopy measurements. None of my research would have been possible without the kind help offered by them.

My gratitude also goes to my fellow group mates including Dr. Aslihan Tuna, Dr. Yuxia Shen, Dr. Sijie Yang, Bin Chen, Kedi Wu, Ying Qin, Yi Zhou, Han, Li, Kentaro Yumigeta, Dipesh Trivedi, Anupum Punt, Xi Fan, Ashutosh Agarwal, and Wilson Kong, for their direct and indirect contributions to this project. I would like to specially thank Bin Chen who spent much time and effort on taking huge amount of high quality TEM data.

I would like to thank my girlfriend Qian Wang, who is also a PhD student and provided irreplaceable emotional support during my PhD studies.

Finally, I would like to thank my parents Yanli Jiang and Hongfeng Cai, for their immense support throughout my life that made this work possible.

TABLE OF CONTENTS

Page

LIST OF FIGURES x

CHAPTER

1 INTRODUCTION TO LAYER STRUCTURED GALLIUM CHALCOGENIDES 1

1.1 Introduction to Layer Structured Two Dimensional (2D) Semiconductors...... 1

1.2 Gallium Chalcogenides and Their Emerging Properties 2

1.2.1 Crystal and Electronic Structure 3

1.2.2 Synthesis Methods 5

1.2.3 Characterization, Properties and Applications................................. 8

1.3 Motivation and Significance of This Work 11

2 SYNTHESIS AND PHYSICAL PROPERTIES ENGINEERING IN 2D MATERIALS.. 14

2.1 Principles of Synthesis Methods for 2D Materials 14

2.1.1 Mechanical Exfoliation.. 14

2.1.2 Vapor Phase Transport... 15

2.2 Principles of Physical Properties Engineering in 2D Materials...................... 20

2.2.1 Strain Engineering 20

2.2.2 Defect Engineering 22

2.2.3 Phase Engineering in Heterostructural Alloys 24

2.3 Experimental Methods.. 26

2.3.1 Optical Properties and Lattice Dynamics Characterization 26

CHAPTER Page

2.3.2 Morphology and Thickness Characterization 27

2.3.3 Composition and Crystal Structure Characterization 27

2.3.4 Density Functional Theory Calculations 28

3 CONTROLLED SYNTHESIS AND BAND ENGINEERING OF GaSe 31

3.1 Synthesis of 2D GaSe on Si (111) 31

3.2 Band Gap Engineering by Lateral Strain 36

3.3 Effect of the Vertical Compressive Strain 42

3.4 Summary 46

4 SYNTHESIS AND NOVEL PROPERTIES OF GaTe 47

4.1 Synthesis and Structural Characteristics of Nanostructured GaTe 47

4.2 Optical Properties of VPT Deposited GaTe.. 52

4.3 Anisotropy of VPT Synthesized GaTe 58

4.4 Summary 62

5 SYNTHESIS AND PHASE CROSSOVER IN GaSeTe ALLOYS 63

5.1 Synthesis of $GaSe_{1-x}Te_x$ Alloys Across the Full Composition 63

5.2 Signature of Phase Transition in Raman Spectroscopy 68

5.3 The Phase Crossover and Abnormal Band Bowing....................................... 70

5.4 Isotropic to Anisotropic Phase Transition... 75

5.5 Coexistence of the Hexagonal and Monoclinic Phase in the Crossover Region 80

5.6 Summary 83

6 CONCLUSIONS AND OUTLOOK... 84

5.1 Conclusions 84

5.2 Outlook 85

REFERENCES 89

LIST OF FIGURES

Figure Page

1.1 **(a)** Side and top view of the crystal structure of hexagonal GaX such as GaS and GaSe. **(b)** Side and top view of the crystal structure of monoclinic GaTe. 3

1.2 **(a)** The electronic band structure of bulk GaSe, calculated using a DFT-LDA method. **(b)** The electronic band structure of monolayer GaSe, calculated using a DFT-LDA method. (Figure taken from Ref. 36) 4

1.3 **(a)** The mechanical exfoliation method using a scotch tape. **(b)** Optical image of few layered GaSe on Si/SiO_2 prepared by mechanical exfoliation. (Figure taken from Ref. 9) **(c)** Vapor phase transport method for synthesizing 2D GaSe. **(d)** 2D GaSe flake synthesized by vapor phase transport. (Figure taken from Ref. 38) 7

1.4 **(a)** Schematics of the Raman modes of GaSe. The colored arrows designate the vibrational directions of selenium atoms (orange) and gallium (green) atoms. **(b)** Raman spectra of GaSe with different layer numbers. **(c).** Zoom-in of the A_{1g} peak of GaSe. (Figure taken from Ref. 51) 9

1.5 **(a)** Raman spectrum of GaTe calculated by density functional perturbation theory (DFPT). **(b)** Experimental Raman spectrum of a bulk GaTe single crystal. **(c)** The Raman intensity *vs* polarization angle for the A_g mode (115 cm^{-1}). **(d)** The Raman intensity *vs* polarization angle for the B_g mode (161 cm^{-1}). (Figure taken from Ref. 25) 10

2.1 Schematics of the boundary layer on the substrate in a typical VPT process. (Figure taken from Ref. 62) 16

2.2 Free energy change as a function of the radius of the nucleus. (Figure taken from Ref. 63) 17

Figure Page

2.3 Schematics of the (a) Volmer-Weber growth mode, (b) Stranski-Krastanov growth mode and (c) Frank-van der Merwe growth mode. (Figure taken from Ref. 64). 18

2.4 Schematic diagram of the VPT system and growth process............................... 19

2.5 Schematic of the Electron energy levels in diamond structured carbon as a function of the lattice constant. (Figure taken from Ref. 65).. 21

2.6 Schematic of the harmonic oscillator formed in a bi-atomic molecule before and after strain. 22

2.7 Schematics of edge dislocation and screw dislocation. (Figure taken from Ref. 66) 23

2.8 Bandgap vs lattice constant of common semiconductor alloys. (Figure taken from Ref. 68) 24

2.9 Calculated critical temperatures for the GaInAs alloy as a function of composition. The solid dark lines correspond to strain-free material. The other results assume the strains that would be induced by pseudomorphic heteroepitaxial growth on the noted substrates. (Figure taken from Ref. 70)... 26

3.1 **(a)** Schematics of the interatomic displacement in Si (111) face. **(b)** Schematics of the interatomic displacement in GaSe (0001) face. 32

3.2 **(a)** Temperature profiles during the cooling process used in the VPT growth of GaSe. **(b)** Optical images of flat triangle, pyramid and spiral flakes of GaSe obtained by corresponding cooling process. **(c)** Optical image of VPT grown GaSe on sapphire. 33

Figure Page

3.3 AFM images and height profiles of flat triangle **(a)**, pyramid **(b)** and spiral **(c)** GaSe flakes. The height profiles are taken from positions indicated by the yellow arrows. 34

3.4 **(a)** EDS spectrum of a VPT grown GaSe pyramid on Si. **(b)** EDS mapping of a VPT grown GaSe pyramid on Si. **(c)** Low magnification image of a VPT grown GaSe triangle. **(d)** HAADF image of the selected area in (c). **(e)** Intensity profile along the yellow line in (d), indicating the ABAB stacking of GaSe........ 34

3.5 **(a)** Optical image of a VPT synthesized GaSe triangle flake. **(b)** PL peak position and intensity mapping of the GaSe flake in (a). **(c)** PL spectra of the exfoliated flake and the VPT synthesized triangle, taken at locations pointed in (a) and (d) by dots with corresponding colors. **(d)** Optical image of an exfoliated GaSe flake. **(e)** PL peak position and intensity mapping of the GaSe flake in (d). **(f)** Normalized PL spectra of bulk GaSe, GaSeTe alloy and GaTe crystals........ 37

3.6 **(a)** PL peak position and intensity mapping of the pyramid and spiral shaped GaSe flake. **(b)** Distribution of PL FWHM as a function of peak position for each case. The quadrilaterals are for eye-guidance........ 38

3.7 **(a)** Raman spectra of the VPT synthesized GaSe triangle taken at locations indicated by the dots in Figure 3.5a with corresponding colors. The result is compared to an exfoliated (unstrained) GaSe flake in Figure 3.5d. **(b)** Fitted spectra of the vibration modes of A_{1g}^1, E_{2g} and A_{1g}^2 on exfoliated and VPT synthesized triangle. **(c)** The shift of each vibration mode as a function of PL peak position as shown in Figure 3.5c. **(d)** Schematics of the vibrational property of in-plane biaxial strained GaSe........ 39

Figure Page

3.8 **(a)** DFT calculated bandgap as a function of strain. **(b)** Schematic diagram of the funnel effect caused by non-uniform strain. 41

3.9 **(a)** Schematic of the experimental setup using a diamond anvil cell. **(b-c)** Pressure-dependent Raman spectra of the Si substrate for exfoliated GaSe (b) and VPT grown spiral GaSe (c). The pressure is estimated by the shift amount of the Si peak using a previously established relation[89]. 43

3.10 **(a)** Pressure-dependent Raman spectra of exfoliated GaSe. **(b)** Pressure-dependent Raman spectra of VPT synthesized spiral flake. **(c)** Pressure-dependent PL spectra of exfoliated GaSe. **(d)** Pressure-dependent PL spectra of VPT synthesized spiral flake.. 44

3.11 **(a)** Band gap as a function of pressure for exfoliated and VPT synthesized triangle and spiral flakes. Dashed lines are linear fits to each set of data. **(b)** Ratio of band gap change as a function of vertical pressure obtained from (a). **(c)** DFT calculated band gap as a function of pressure for strained and unstrained GaSe. **(d)** Ratio of band gap change as a function of vertical pressure obtained from (c). 45

4.1 **(a-b)** Optical (a) and false colored SEM (b) images of GaTe synthesized on GaAs (111) substrate. **(c-d)** Optical (c) and false colored SEM (d) images of GaTe synthesized on Si (111) substrate... 48

4.2 **(a)** XRD spectrum of GaTe grown on GaAs (111). **(b)** Pole figure XRD spectra of the GaTe (002) plane and the GaAs (111) plane system. **(c)** The atomic structure of both planes shown in (b). 49

Figure Page

4.3 **(a)** SEM image of GaTe grown at the edge of the GaAs (111) substrate. inset: Zoom-in view of a GaTe nanowire grown on GaAs (111). **(b)** HRTEM image of the VPT grown GaTe that shows the chain structure. **(c)** atomic structure of the GaAs (111) surface with the GaTe nanowire growth direction labeled by blue arrows. **(d)** 3D atomic model of the GaTe nanowires grown on GaAs (111). 51

4.4 **(a).** Optical image of GaTe synthesized on c-cut sapphire substrate. **(b)** Photoluminescence spectra of GaTe synthesized on various substrates. **(c)** Raman spectra of GaTe synthesized on various substrates. **(d)** Low magnification TEM image and HRTEM image of the B area (inset). **(e)** selected area electron diffraction (SAED) pattern of a GaTe flake synthesized on sapphire. The SAED patterns are taken at three different regions marked by the squares in the TEM image. **(f)** EDS mapping of Ga and Te taken on the GaTe flake. 53

4.5 **(a)** Optical image of two typical GaTe flakes grown on sapphire. **(b)** PL intensity mapping at 1.39 eV and 1.66 eV for the two flakes. **(c)** AFM images of the two flakes. yellow dashed lines show the position for the 1.39 eV emission. **(d)** Line scan of the PL spectra taken along the white arrow at flake #2 shown in (b). 54

4.6 **(a)** Temperature dependent PL spectra measured at the spot with 1.39 eV emission. **(b)** PL and photo reflectance spectra measured at the spot with the intermediate band emission at 4 K. **(c)** log-scale plot of the PL spectrum in (b) to show the X_{def}........ 55

4.7 **(a)** Power dependent PL spectra measured at the spot with the intermediate band emission at room temperature. **(b)** PL spectra of the GaTe flakes excited by different laser energies at 4 K. 57

Figure Page

4.8 **(a)** Schematics of the crystal structure of hexagonal and monoclinic GaTe. **(b)** Angle resolved PL and reflectance intensity of the GaTe flake. The optical (scale bar = 5μm) and HRTEM images (scale bar = 2 nm) corresponding to 0o, 90o, 180o and 270o are shown around, with red arrows pointing toward the <010> chain direction. The blue spot shows the location where the PL and HRTEM are measured. 59

4.9 **(a-d)** Optical image and angle resolved Raman intensity of the 116 cm^{-1}, 164 cm^{-1} and 212 cm^{-1} peaks of the same GaTe flake, with a red spot showing the location where the angle resolved Raman spectroscopy is measured. The domain structure is indicated by the rectangles in (a). The solid lines in (a) are fitted curves. 60

5.1 Phase diagram of the GaSe-GaTe system. (Figure taken from Ref. 102) 64

5.2 Schematic of the VPT growth process of GaSeTe and InGaSe alloys. 65

5.3 EDS spectra of the $GaSe_{1-x}Te_x$ nanostructures and the calculated composition . 66

5.4 Optical images of the $GaSe_{1-x}Te_x$ nanostructures grown at different d between GaTe and GaSe source. Corresponding x values are shown on the top left corner of each image. Scale bar=5 μm for x=0.28, 0.49 and 0.56; 10 μm for x=0.57 and 0.8................ 66

5.5 **(a)** Low magnification TEM image of a $GaSe_{1-x}Te_x$ nanowire with x=0.63. **(b)** SAED pattern of the nanowire taken from zone axis [102]. **(c)** HRTEM image of the nanowire with zone axis of [102]... 68

5.6 **(a)** Raman spectra of $GaSe_{1-x}Te_x$ nanostructures at different compositions. Monoclinic and hexagonal structures are separated by different background colors **(b)** Peak positions of different Raman modes as a function of Te content in $GaSe_{1-x}Te_x$. Blue background indicates the hexagonal side and yellow background indicates the monoclinic

Figure Page

side. (c) Raman spectrum of the GaAs (111) substrate showing the transverse optical (TO) mode and the longitudinal optical (LO) mode. 69

5.7 **(a)** PL spectra of $GaSe_{1-x}Te_x$ nanostructures at different compositions **(b)** Bandgap as a function of Te content in $GaSe_{1-x}Te_x$. (c) PL spectrum of the GaAs (111) substrate. 71

5.8 **(a)** Formation energies of both hexagonal and monoclinic phases of the GaSeTe alloy at various compositions. **(b)** Cluster expansion predictions and DFT calculations of the formation energies of GaSeTe alloys at different composition. 72

5.9 Optical images of GaSeTe nanomaterials grown on HOPG (**a**) and sapphire (**b**). 73

5.10 Evolution of angle resolved Raman peak intensity of the 128 cm^{-1} mode as Te content decreases. 76

5.11 TEM and FFT patterns for $GaSe_{1-x}Te_x$ with **(a)** x=0 , **(b)** 0.28, **(c)** 0.57, and **(d)** x=1. The zone axis, interplanar distance and angle between planes are indicated in each image. 77

5.12 **(a)** Optical images of the GaSeTe devices based on the monoclinic (top, scale bar=10 μm) phase and hexagonal (bottom, scale bar=5 μm) phase. **(b)** Angle resolved photocurrent as a function of light polarization (E field) direction measured on both devices. **(c)** Time resolved photoresponse of the device based on monoclinic GaSeTe (V_{ds}=-0.2 V). The light polarization is alternatively switched between parallel and perpendicular to the b-axis. 78

Figure Page

5.13 **(a)** Optical image of a $GaSe_{1-x}Te_x$ flake with both hexagonal (region-I) and monoclinic (region-II) phase grown simultaneously. **(b)** SEM image of the flake with coexisting hexagonal and monoclinic phase. The composition measured by EDS for each region is indicated by Te% in the figure. **(c-d)** EDS spectra taken from region I and II indicated in **(a)** and **(b)**. 80

5.14 **(a)** Raman spectra taken at region-I and region-II from Figure 5.13a. **(b)** Angle resolved Raman peak intensity of peak A and B from region-I and II. 81

5.15 **(a)** PL spectra taken at region-I and II. GaAs substrate peak is labeled by green backgound. **(b)** PL mapping of the emission intensity at 1.74 eV taken from the area indicated by the rectangular in Figure 5.13a. **(c)** Schematic of the 3D atomic structure of the coexisting hexagonal and monoclinic phases. 82

6.1 Phase diagram of the SnSe-SnTe system. (Figure taken from Ref. 119) 88

CHAPTER 1 INTRODUCTION TO LAYER STRUCTURED GALLIUM CHALCOGENIDES

1.1 Introduction to Layer Structured Two Dimensional (2D) Semiconductors

The discovery of graphene[1] has led to a rapid development of 2D layered materials that now include hexagonal boron nitride (hBN)[2], transition metal dichalcogenides (TMDCs)[3], mono-elemental 2D semiconductors such as phosphorene[4, 5, 6], and post transition metal chalcogenides (PTMCs)[7, 8, 9, 10]. These materials possess a layered structure with strong in-plane covalent bonds and weak van der Waals (vdW) interaction between the layers. This unique layered structure makes it possible to thin down these materials to a few atomic layers and even monolayer, which can exhibit significantly different properties compared to their bulk counterparts. For example, graphene has demonstrated a high electron mobility of 250,000 cm^2/Vs at room temperature[11], an exceptional thermal conductivity of 5000 W/mK[12] and a high Young's modulus of 1 TPa[13]. MoS_2, as a representative TMDC, goes through a transition from indirect bandgap to direct bandgap from bulk to monolayer, and exhibit a high exciton binding energy of 300 meV in the monolayer form[14, 15, 16].

Most of the 2D materials possess a hexagonal crystal structure that is isotropic in the plane formed by *a* and *b* axis but highly anisotropic in the out-of-plane *c* axis. Examples include graphene, hBN, GaSe and TMDCs in the hexagonal phase. As a result, the in-plane light-matter interaction is isotropic and independent to the polarization angle of the incoming light. Apart fro43m the isotropic hexagonal phase, some 2D materials can also form orthorhombic phase (black phosphorous)[17, 18], triclinic phase (ReS_2)[19, 20, 21, 22] and monoclinic phase (GaTe)[23, 24, 25]. In these structures, instead of forming in-plane 3-fold

symmetry hexagonal rings, the atoms are arranged in a distorted pattern and form chains along a certain axis. The interatomic distance within the chains is significantly different from that between the chains. Such chain structure leads to a highly in-plane anisotropy of the electron wave function and give rise to anisotropic electrical and optical properties. For example, in black phosphorous (BP) each P atom is connected to 3 other P atoms to form a stable ring structure just like in graphene. But the rings are puckered so it has a reduced symmetry compared to graphene and a clear chain structure is formed along the b axis. This gives BP a unique angle dependent electrical and thermal conductivity[26]. Another example is ReS_2, a member of TMDCs with an optical bandgap around 1.4 eV (bulk) and 1.6 eV (monolayer)[20]. In comparison to the isotropic group-VIB TMDCs such as MoS_2 and WSe_2, the rhenium atom in ReS_2 has an extra electron that is shared between two neighboring rhenium atoms. Thus, highly oriented Re-Re chains are formed along the *b*-axis lattice direction due to strong interaction and dimerization between the adjacent Re atoms. The anisotropic crystal structure gives ReS_2 unique applications in direction sensitive field effect transistors and polarization dependent photodetectors[27, 28, 29].

1.2 Gallium Chalcogenides and Their Emerging Properties

Gallium chalcogenides belong to the PTMC category that mainly includes the following stoichiometric compositions: MX and M_2X_3 (M=In, Ga, Sn and X=S, Se, Te). Among these compounds, monochalcogenides, i.e. MX, have emerged as novel 2D semiconducting materials and shown their potentials in next generation optoelectronic applications[30]. This dissertation focuses on layer structured gallium mono-chalcogenides (GaX) including GaSe, GaTe and their alloys such as GaSeTe.

1.2.1 Crystal and Electronic Structure

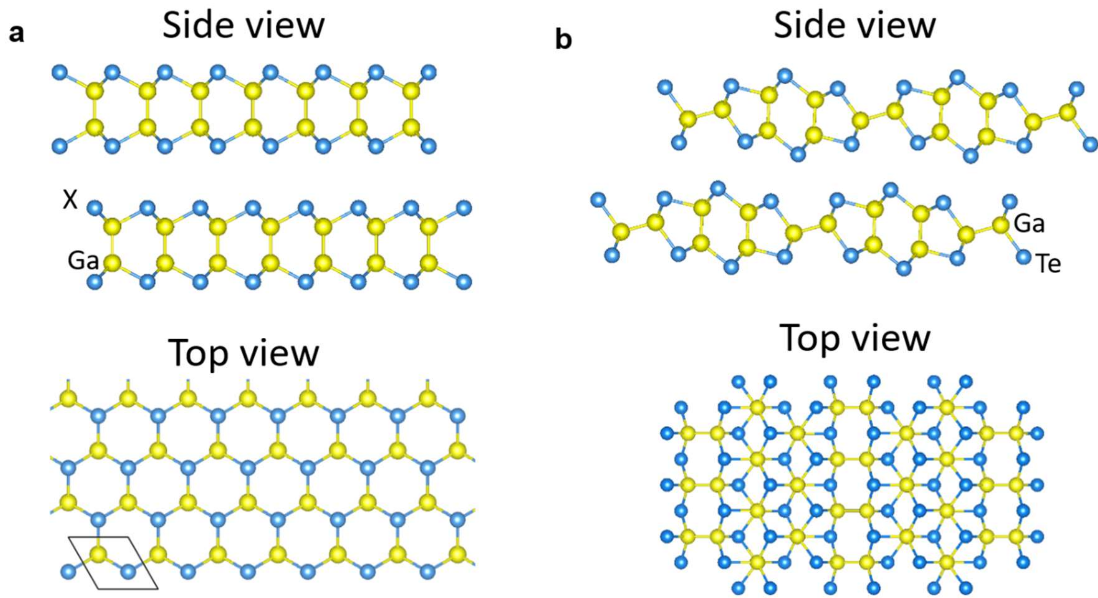

Figure 1.1 **(a)** Side and top view of the crystal structure of hexagonal GaX such as GaS and GaSe. **(b)** Side and top view of the crystal structure of monoclinic GaTe.

The atoms in GaX layers are generally arranged in such a way that two Ga atoms are sandwiched between two chalcogen atoms to form the "X-Ga-Ga-X" structure (Figure 1.1a), compared to the "X-M-X" assembly of group-VI TMDCs. Each Ga atom is bonded with another Ga atom and 3 X atoms, and each X atom is bonded with 3 Ga atoms. While the atomic arrangement in a single layer is fixed, GaX can form a wide variety of polytypes based on the stacking sequence of the layers[31]. GaS has a hexagonal structure with the lattice constants a=3.587 Å and c=15.492 Å. It favors the β polytype and a space group of $P\bar{6}m2$. GaSe has the same atomic arrangement within a monolayer, but exhibit more polytypes due to various stacking orders. The most common phases are β- and ε-GaSe[32]. The β phase has an inversion center between the layers due to the stacking mode and belongs to the space group of D_{6h}^{4}. The ε phase is not centrosymmetric and

belongs to the space group D_{3h}^{1}. Both ε and β phases have the same lattice constants of a=3.75 Å and c=15.94 Å, with the monolayer thickness of 0.8 nm.

An anomaly in the GaX family, in terms of crystal structure, is GaTe. It exists in two phases: hexagonal and monoclinic, and the monoclinic phase is found to be more stable (Figure 1.1b)[33]. It belongs to the space group C2/m with lattice constants of a=17.32 Å, b=4.05 Å and c=10.54 Å. In the monoclinic phase, every third of the Ga-Ga bonds is twisted toward the in-plane direction and the bonding length is different from those pointing out of plane. Similar to black phosphorous and ReS_2, the distorted bonding structure results in the formation of atomic chains along the <010> direction and gives rise to the anisotropic behavior in light-matter interaction[25, 34, 35].

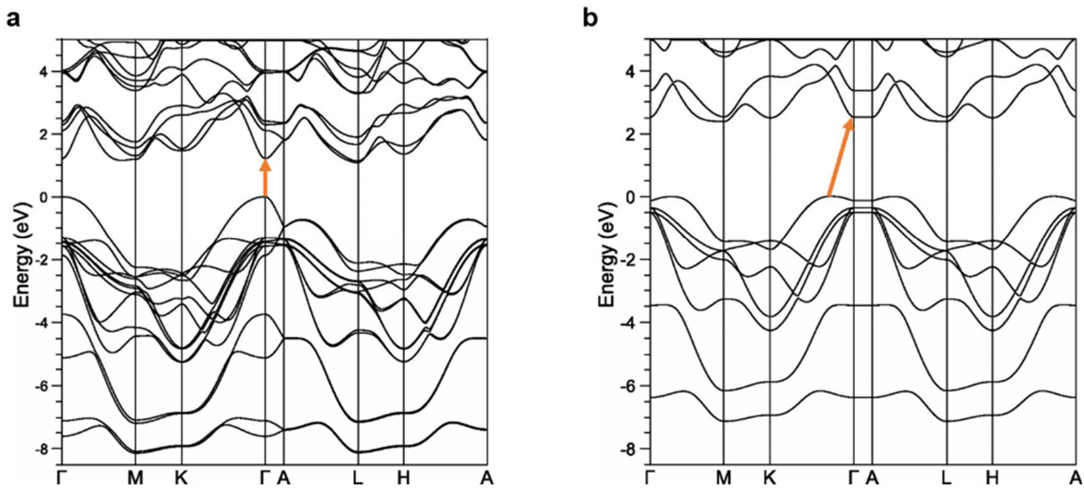

Figure 1.2 **(a)** The electronic band structure of bulk GaSe, calculated using a DFT-LDA method. **(b)** The electronic band structure of monolayer GaSe, calculated using a DFT-LDA method. (Figure taken from Ref. 36 © 2011 American Physical Society)

The unique crystal structure of GaX leads to distinctive electronic band structure compared to other 2D systems such as TMDCs. The bandgap of bulk GaX spans a wide range from 1.66 eV (GaTe) to 2.55 eV (GaS). Bulk GaSe has an indirect band gap of

about 2.0 eV and a direct band gap of only about 25 meV higher[37]. Since the indirect band gap and direct band gap are very close to each other, electrons can easily jump between the two levels with the help of a small amount of thermal energy. As a result, bulk GaSe behaves like a direct band gap semiconductor at room temperature and is highly luminescent. 2D GaSe shows a tunable band gap as a function of the number of layers. As the layer number reduces, the valence band maximum (VBM) at Γ point splits symmetrically and form an "M" shaped pattern, whereas the conduction band minimum (CBM) stays at Γ point. This band renormalization leads to a direct-to-indirect band gap transition from bulk to monolayer GaSe (Figure 1.2b)[36]. Various routes including both theoretical and experimental have been taken to acquire the band gap of monolayer GaSe. Rybkovskiy et al. carried out density functional theory (DFT) calculations using local density approximation (LDA) and reported the band gap value of and 1.21 eV for bulk GaSe (Figure 1.2a) and 2.60 eV for monolayer (Figure 1.2b)[36]. LDA is known to underestimate the band gap value since it overestimates the lattice constant. Using GW approximation, the band gap of 3.89 eV was obtained for monolayer GaSe and 2.34 eV for bulk[36]. Lei et al. reported an indirect band gap of 3.3 eV according to the photocurrent measurements for 2D GaSe layers[38]. Jung et al. reported the same value according to the cathodoluminescence (CL) measurements for monolayer GaSe[39]. Similar direct to indirect band gap transition happens for other PTMCs such as InSe and GaTe. The band gap for few layered InSe and GaTe was found to be 1.45 eV and 1.7 eV respectively based on DFT calculations[40, 41, 42].

1.2.2 Synthesis Methods

The synthesis methods of 2D GaX can be generally divided into two categories: bottom-up and top-down. The top-down approach generates 2D GaX sheets by exfoliation from bulk crystals. Commonly used methods include mechanical cleavage by scotch tape[43], liquid and chemical exfoliation[44], ion intercalation[45] and ultrasonication[46]. The scotch tape method (Figure. 1.3a) is the most widely used method to prepare 2D GaX since its successful application in graphene and TMDCs. A piece of GaX crystal is first adhered to the sticky scotch tape, then the tape is folded and unfolded for several times to reduce the thickness of the crystal. After that, the tape is brought into contact with a certain substrate. After the tape is cleaved from the substrate, the GaX flakes are left on the surface of the substrate. The sample is then brought to an optical microscope for observation. For a better optical contrast of monolayers, Si wafers with 285 nm SiO_2 are often used as the substrate, where the 2D layers appear in blue color (Figure. 1.3b)[9]. Despite the simplicity of this method and the high quality single crystalline flakes that can be obtained, it is hard to produce large scale 2D flakes with uniform thickness. To improve the scalability and uniformity of the 2D flakes, other top-down methods have been developed, such as liquid exfoliation and electrochemical exfoliation. These methods were mostly reported on graphene, black phosphorous and TMDCs, but not on GaX.

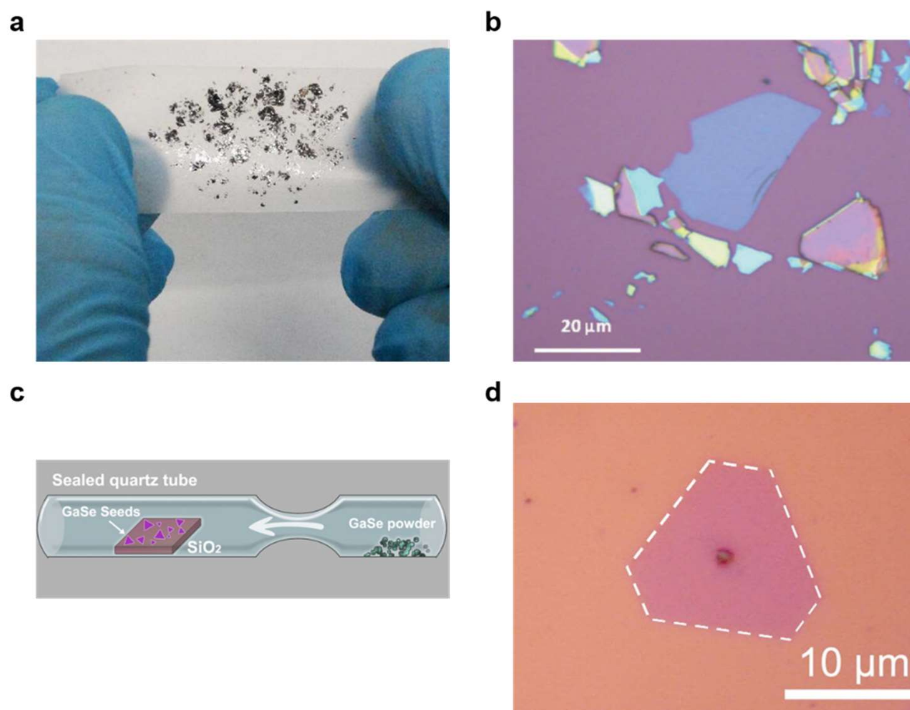

Figure 1.3 **(a)** The mechanical exfoliation method using a scotch tape. **(b)** Optical image of few layered GaSe on Si/SiO_2 prepared by mechanical exfoliation. (Figure taken from Ref. 9 © 2012 John Wiley and Sons) **(c)** Vapor phase transport method for synthesizing 2D GaSe. **(d)** 2D GaSe flake synthesized by vapor phase transport. (Figure taken from Ref. 38 © 2013 American Chemical Society)

The synthesis of large area and uniform 2D flakes is crucial for their applications. To accomplish this, vapor phase transport (VPT) method has been established as a bottom-up approach. Lei et al. first reported the VPT synthesis of large area atomically thin GaSe flakes on SiO_2/Si[38]. In this method, GaSe source powders and substrates with GaSe particles as seeds were placed in opposite ends of a sealed quartz tube (Figure 1.3c). The tube was in vacuum condition with 10^{-3} Torr Ar to avoid oxidization of GaSe. During the growth process, the source and substrates were kept at 750 °C and 720 °C respectively for 20 min, followed by rapid cooling to room temperature. After the growth, atomically thin GaSe flakes with thickness down to 2 nm were obtained (Figure 1.3d). The flakes form in

triangle, truncated triangle and hexagonal shapes which can be controlled by the concentration of the source, as well as the distance between the source and nucleation site. A modified VPT method has been used by Zhou et al. and Li et al. to grow 2D GaSe on various substrates such as mica and graphene[47, 48]. In this method, GaSe and Ga_2Se_3 powders were mixed at molar ratio of 50:1 and placed at the hot zone (750 °C) in a tube furnace to serve as the source. Ar was used as the transport gas and the substrate was placed downstream at 720 °C. Single and few layered GaSe flakes with triangle shapes were synthesized on flexible and transparent mica substrates. Despite the large 35% lattice mismatch between GaSe and mica, the GaSe triangles show identical orientations and terrace structures, which is a sign of epitaxial growth mechanism. The growth on graphene showed similar epitaxial nature except that the GaSe epilayers form irregular shapes and different lattice orientation from the graphene layers. Generally, a rotation angle of 10.5 ± 0.3 degrees was observed in the prepared GaSe epilayers.

Using a similar approach, GaTe nanosheets with planar alignments have been grown on flexible mica substrates, which follow a van der Waals epitaxial growth mechanism by taking advantage of the chemically inert surface of mica[49]. On one hand, the chemically inert mica surface enables the lateral epitaxial growth of GaTe nanosheets without strict lattice matching. On the other hand, weak van der Waals interactions between the mica substrate and GaTe adatoms facilitate the lateral migration of the GaTe adatoms, and thus promote the lateral growth of the GaTe nanosheets.

1.2.3 Characterization, Properties and Applications

Various techniques are employed to characterize 2D materials such as optical microscopy, Raman spectroscopy, Photoluminescence (PL) spectroscopy, scanning

electron microscopy (SEM), atomic force microscopy (AFM) and high-resolution transmission electron microscopy (HRTEM). Raman spectroscopy is the most widely used method to characterize the crystal structure and vibrational properties of 2D materials. For bulk GaSe, there are 12 vibrational modes, including 8 in-plane modes of E' and E" and 4 out-of-plane modes of A_1' and A_2". All Raman modes are active except A_2"[7, 38, 50]. The schematics of each active vibration mode and the typical Raman spectra for GaSe with different thickness is depicted in Figure 1.4[51]. The intensity decreases dramatically and even tends to vanish when the thickness approaches 1-2 layers.

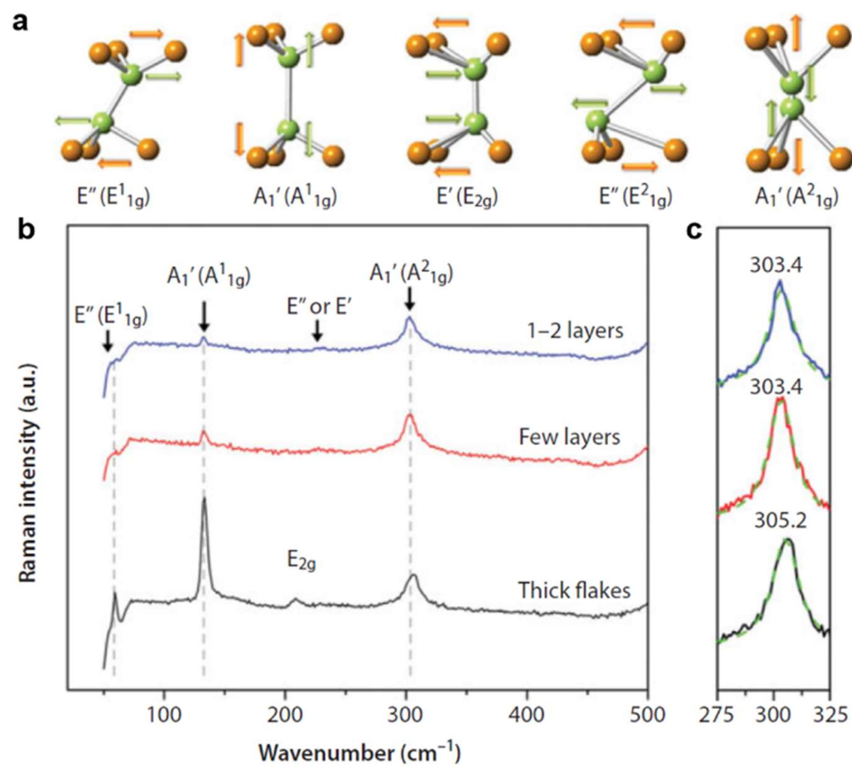

Figure 1.4 **(a)** Schematics of the Raman modes of GaSe. The colored arrows designate the vibrational directions of selenium atoms (orange) and gallium (green) atoms. **(b)** Raman spectra of GaSe with different layer numbers. **(c).** Zoom-in of the A_{1g} peak of GaSe. (Figure taken from Ref. 51 © 2016 Scrivener Publishing LLC)

The vibrational properties for GaTe is much more complicated not only because it has more active modes (Figure 1.5a and Figure 1.5b), but also it shows anisotropic nature due to the chain structure in the monoclinic phase. Angle resolved Raman spectroscopy has been used to study the anisotropic behavior of GaTe prepared by mechanical exfoliation[25]. The A_g mode at 115 cm^{-1} shows relatively stronger anisotropy with a period of 180° and with maximum intensities along the *x*-axis (Figure 1.5c). On the other hand, the mode around 161 cm^{-1} shows a 4-fold anisotropy with a period of 90°, and the maximum intensities along 45°and 135° (Figure 1.5d).

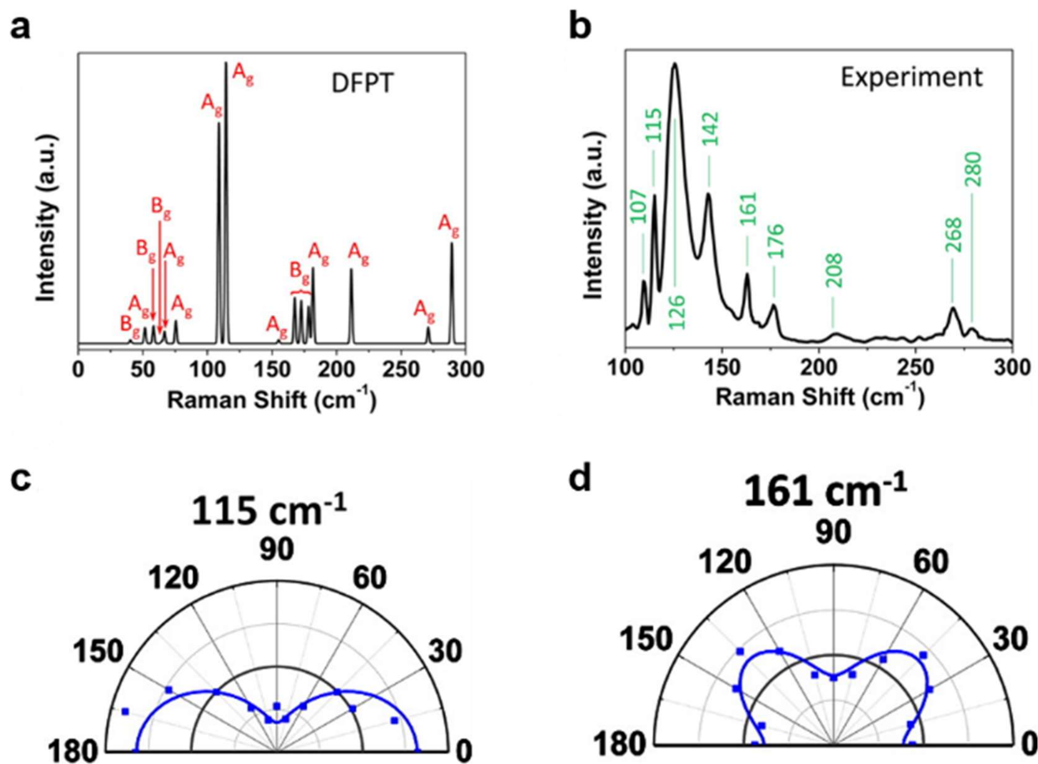

Figure 1.5 **(a)** Raman spectrum of GaTe calculated by density functional perturbation theory (DFPT). **(b)** Experimental Raman spectrum of a bulk GaTe single crystal. **(c)** The Raman intensity *vs* polarization angle for the A_g mode (115 cm^{-1}). **(d)** The Raman intensity *vs* polarization angle for the B_g mode (161 cm^{-1}). (Figure taken from Ref. 25 © 2016 American Chemical Society)

PL spectroscopy is used to characterize the band gap and optical properties of PTMCs. Two-dimensional GaSe flakes show a thickness dependent PL spectra, suggesting the thickness dependence of the band gap[10]. The PL intensity of 2D GaSe declines as thickness reduces to monolayer due to the direct to indirect band gap transition. The PL peak also blue shifts by about 20 meV from bulk to bilayer due to the opening of the band gap. Unlike 2D GaSe whose optical properties have attracted much attention, the studies on GaTe still stays at its bulk form and no thickness dependent PL has been reported.

1.3 Motivation and Significance of This Work

Owing to their indirect bandgap within the visible light range in the 2D form, gallium chalcogenides have potential applications in solar cells and photodetectors where electron-hole pairs need to be separated efficiently. The VBM and CBM positions of 2D GaX is also predicted to be suitable for photocatalysis of water splitting[52]. In order to realize these applications, there is a demand to engineer their band gap and optical properties as we need. For example, applications such as solar cells and photocatalysis require the material to have a wide spectrum response to sunlight for maximum absorption, which can be achieved by bandgap engineering. In this dissertation, multiple methods including strain engineering and alloying are demonstrated to obtain wide bandgap tuning range in gallium chalcogenides.

Applying strain is one of the methods to induce band gap tuning in 2D semiconductors and has been thoroughly studied on exfoliated TMDCs. Castellanos-Gomez et al. created wrinkled MoS_2 on an elastomeric substrate to study the local strain effect on the band structure using PL measurements[53]. A strain-induced reduction of the

direct band gap and funneling of photo generated excitons toward regions of higher strain has been observed. Similar method was also used on GaSe to manipulate its optical properties. Strained 2D GaSe was found to emit photons at almost the same wavelength as unstrained material but appears an order of magnitude brighter[54]. Despite the promising results of strain engineering, this method has been mostly studied on exfoliated samples and the strain usually comes from an external force. As a result, the band gap tuning effect was quite limited due to the small amount of strain that can be applied. Thus it is necessary to find a way to synthesize naturally strained GaX with higher amount of band gap tuning. Moreover, most of the previous studies used lateral strain along the in-plane direction. The effect of vertical strain on the band structure of 2D GaX still needs to be further studied. In this work, a method of applying strain in both lateral and vertical directions simultaneously is demonstrated to successfully reduce the bandgap of GaSe from 2.0 eV to 1.4 eV, which is so far the largest bandgap tuning range reported on GaSe. The result opens up opportunities for applying GaSe as a wide spectrum light absorbing material in solar cells and photocatalysis.

Another widely used method for band gap engineering is alloying. $GaTe_xSe_{1-x}$ alloys have been successfully synthesized by molecular beam epitaxy (MBE) on Si substrates and a composition-dependent phonon vibration frequency has been observed across the full compositional range[55]. $GaS_{1-x}Se_x$ nanobelts synthesized by chemical vapor transport also exhibited compositional dependent photoluminescence at 490−620 nm[56]. However, the materials demonstrated in these works are all in the bulk form. Synthesis of 2D GaX alloys still remains as a big challenge. Moreover, since GaTe exists in monoclinic phase while GaSe is in hexagonal phase, there exists huge miscibility gaps in the GaSe-GaTe

phase diagram, making it difficult to synthesize full composition alloy and reach a wide bandgap tuning range. In this dissertation, I present a method to close the miscibility gap in the GaSe-GaTe system and form full composition GaSeTe alloys. The alloys show a monoclinic to hexagonal phase transition and crossover, which is observed for the first time in any 2D alloy systems. This method widens the bandgap tuning range significantly compared to other 2D alloys without such phase crossover behavior. The similar formation energies for different phases in the phase crossover region also makes GaSeTe alloy a potential phase change material with possible applications in memory devices.

Defect engineering in 2D materials has induced novel properties such as quantum dot like single photon emission in 2D TMDCs[57, 58, 59, 60]. Similar findings were also made in exfoliated GaSe with localized excitons trapped by local strain field[61]. Unlike the thorough studies carried out on 2D TMDCs, a very limited number of work has been done on the effect of defects on the luminescence properties of GaX, leaving this field quite unexplored. In this work, I report novel photoluminescence lines induced by various types of defects existing in GaTe that have not been observed before. The emission peaks have distinguished features in peak width, power dependent and temperature dependent behaviors, originating from the type of related defects. This finding deepens our understanding on the defect states in GaTe and provides opportunities for tuning the optical properties of GaTe through defect engineering.

Following the above discussion, this thesis will focus on (i). Strain induced band gap engineering in VPT synthesized GaSe; (ii). Defect induced band structure tuning and anisotropic optical properties of VPT synthesized GaTe and (iii). Band gap tuning by phase engineering in VPT synthesized GaSeTe alloys.

CHAPTER 2 SYNTHESIS AND PHYSICAL PROPERTIES ENGINEERING IN 2D MATERIALS

This chapter describes the methods being used in this dissertation for synthesis, characterization and physical properties engineering in 2D materials. In this work, I designed and carried out the vapor phase transport (VPT) synthesis process for 2D GaSe, GaTe and GaSeTe alloys. I carried out room temperature PL and Raman measurements to study their optical and lattice vibrational properties. Low temperature PL and reflectance measurements were performed by Prof. Bernhard Urbaszek's group. I performed scanning electron microscopy (SEM), electron dispersion spectroscopy (EDS) and atomic force microscopy (AFM) measurements to study the morphology, composition and thickness of the GaTe and GaSeTe samples. Composition of 2D GaSe was measured by our collaborator Dr. Changhyun Ko using EDS and Auger electron spectroscopy (AES). Transmission electron microscopy (TEM) and selected area electron diffraction (SAED) experiments were performed by Bin Chen in our group. High-angle annular dark-field imaging (HAADF) on the NION UltraSTEM100 scanning transmission electron microscope (STEM) was conducted by our collaborator Dr. Toshihiro Aoki. Band structure calculations for GaSe under strain were performed by Prof. Jeffrey Grossman's group. Formation energies of GaSeTe alloys were calculated by Prof. Houlong Zhuang's group.

2.1 Principles of Synthesis Methods for 2D Materials

2.1.1 Mechanical Exfoliation

The popular "scotch tape" method is used to prepare mechanically exfoliated 2D GaX flakes on various substrates including Si with 285 nm SiO_2, sapphire, Si and GaAs.

Prior to exfoliation, the sapphire or 285 nm SiO_2/Si substrate is treated by oxygen plasma for 2 minutes to remove the surface contaminants. During exfoliation, a small piece of bulk GaX single crystal is placed on the sticky side of a scotch tape, which is then brought into contact with another piece of scotch tape. Upon cleaving the two pieces of tapes, the crystal breaks into thinner pieces. The process was repeated 4 to 6 times until the crystal appears thin enough. Finally, the scotch tape is pressed onto a desired substrate and then peeled off, leaving the 2D flakes on the substrate surface.

2.1.2 Vapor Phase Transport

Vapor phase transport (VPT) of GaX is carried out in a tube furnace where the source material is located in the center of the furnace with a higher temperature and the substrates are located downstream with a lower temperature. A carrier gas such as Ar is passed into the tube to facilitate the transport of the evaporated precursors.

The VPT process can be divided into three steps: (1) evaporation of the precursor; (2) transport of the reactants and (3) deposition of the product. The boundary layer theory is used to understand the transport process and growth kinetics in VPT. As depicted in Figure 2.1[62], the gas flowing on the surface of the substrate experiences a dragging force toward the opposite direction of its motion which reduces the flow speed. The dragging force mainly comes from the viscous shear and inertial forces at the interface between the gas and substrate. By connecting the point where the flow speed reaches 0.99 u_0, a line profile can be drawn which is defined as the edge of the boundary layer. The flow outside the boundary layer is laminar viscous flow with constant velocity because it is only determined by inertial forces. The thickness of the boundary layer is given by

$$\delta=\frac{10}{3}\frac{L}{\sqrt{Re}} \quad (2.1)$$

where Re is the Reynolds number and L is the distance from the leading edge of the substrate. The reactant moves across the boundary layer by diffusion and then deposit on the substrate as the product.

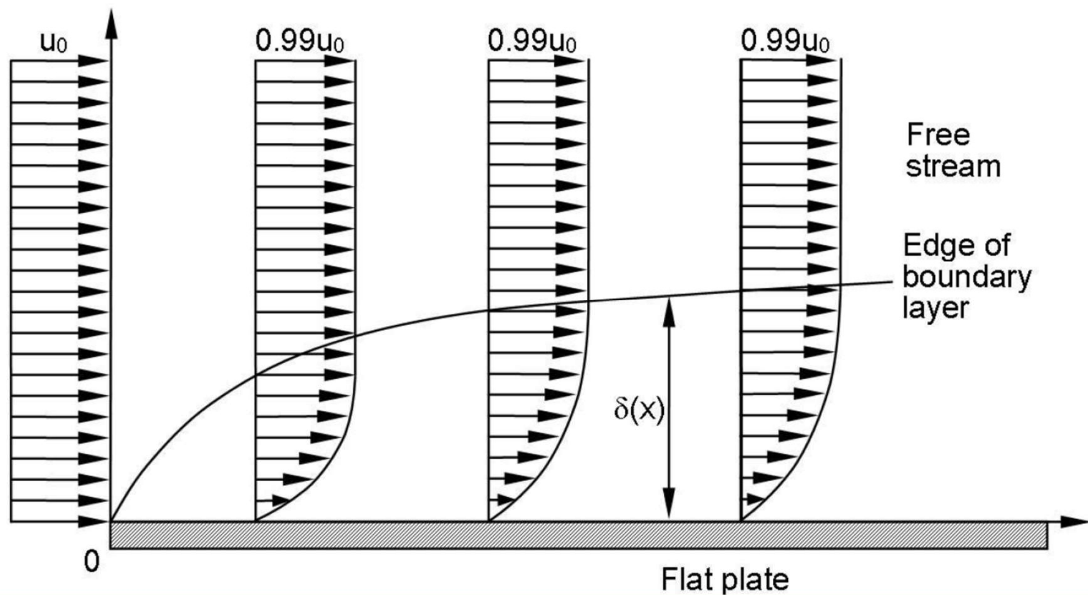

Figure 2.1 Schematics of the boundary layer on the substrate in a typical VPT process. (Figure taken from Ref. 62 © 2010, Springer-Verlag London Limited)

The last step of the VPT process is deposition of the product which can be described by classical nucleation and growth theory[63]. Since the nucleation in the VPT process is gas to solid phase transition, the driving force for nucleation comes from the chemical potential difference of the reactant molecules between its gaseous phase and solid phase:

$$\Delta\mu = \mu_g - \mu_s \quad (2.2)$$

Where μ_g and μ_s are the chemical potentials of the reactant molecules in the gas and solid phase. If the nucleation is homogeneous, then the free energy change during the nucleation process is described as

$$\Delta G_T = -\frac{4}{3}\pi \cdot \frac{r^3}{V}\Delta\mu + 4\pi r^2\sigma \qquad (2.3)$$

where r is the radius of the nucleus, V is the volume of a single molecule and σ is the surface free energy per unit area.

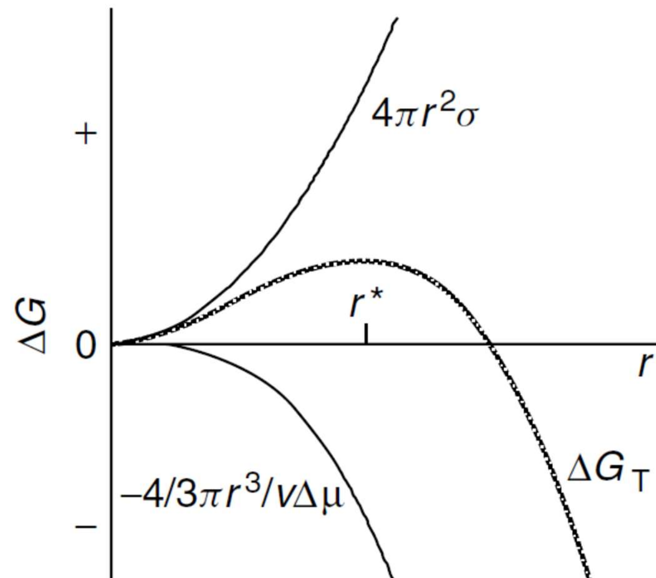

Figure 2.2 Free energy change as a function of the radius of the nucleus. (Figure taken from Ref. 63 © 2010, John Wiley and Sons)

As shown in Figure 2.2[63], ΔG_T reaches maximum at the critical nucleus radius r^*, and the corresponding ΔG^* is the energy barrier that must be overcome for stable nucleus to form. The rate of nucleation can be expressed as:

$$J = A\exp\left(-\frac{\Delta G^*}{k_B T}\right) \qquad (2.4)$$

where A is the prefactor determined by kinetic considerations, k_B is the Boltzmann constant and T is the temperature. In a real VPT process the product is deposited on a substrate, making the nucleation heterogeneous. The presence of a foreign substrate

makes σ smaller and reduces the value of ΔG^* and r^*, making the nucleation more favorable.

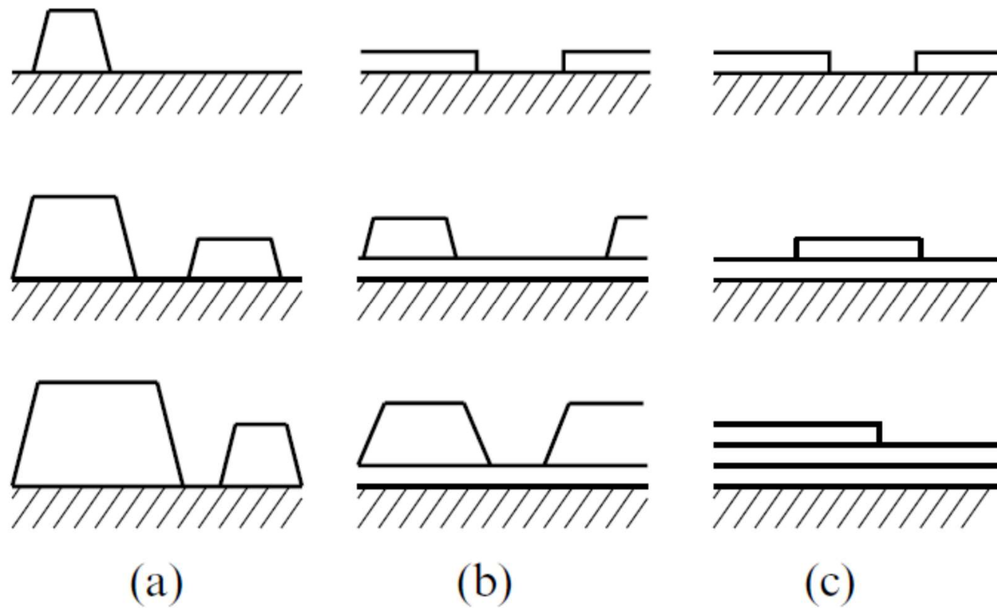

Figure 2.3 Schematics of the (a) Volmer-Weber growth mode, (b) Stranski-Krastanov growth mode and (c) Frank-van der Merwe growth mode. (Figure taken from Ref. 64 © Cambridge University Press)

Based on the different interaction strength between the adatoms and the substrate, the crystal growth on the substrate can be described by three growth modes: the Volmer-Weber mode, the Stranski-Krastanov mode and the Frank-van der Merwe mode[64]. The Volmer-Weber mode, also called island growth mode, is characterized by the formation of three dimensional (3D) clusters or islands. In the Frank-van der Merwe growth mode, also called layer-by-layer mode, adatoms grow in two dimensional layers on the substrate without forming islands, resulting in atomically smooth surfaces. This is the mode that is preferred in the synthesis of 2D materials. The Stranski-Krastanov mode is a combination of the other two modes where both 2D layers and 3D islands are formed.

In a typical experiment, various substrates are used including Si with 285 nm SiO_2, sapphire, Si and GaAs. The process is carried out in a single zone tube furnace equipped with a vacuum pump and various gas channels controlled by mass flow controllers (MFC) (Figure 2.4). The synthesis of 2D GaSe was carried out in a 1″ quartz tube. 60 mg GaSe (BOC sciences) and 3 mg Ga_2Se_3 (Alfa Aesar) powders were mixed together as the source materials and Ar is used as the carrier gas.

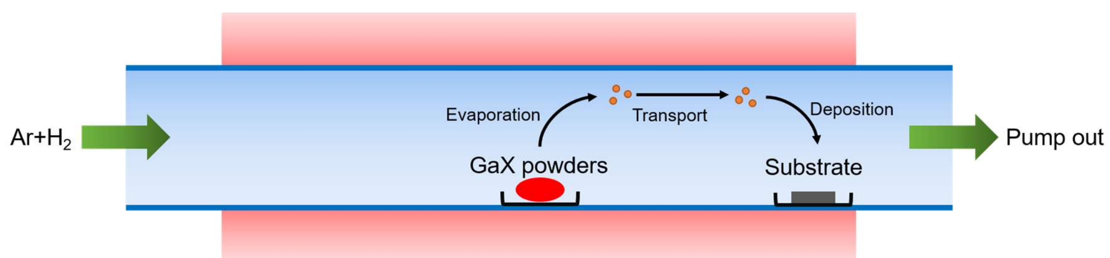

Figure 2.4 Schematic diagram of the VPT system and growth process.

P-type Si (111), sapphire and GaAs (111) wafers were used as growth substrates. Prior to growth the Si wafers were cleaned with acetone, methanol, RCA-1 cleanser (mixture of DI water, 27% $NH_3{\cdot}H_2O$ and 30% H_2O_2 with volume ratio 5:1:1) and 2% HF. The source powders were loaded in a quartz boat and sent to the center of the tube. The substrate was located 13 cm away downstream. The tube was evacuated to 10 mTorr and then heated from room temperature to the growth temperature with a ramping rate of 20 ^{o}C/min. The temperature was kept stable for 5 min and then cooled down following different cooling rate. The Ar flow rate was set at 50 sccm and the growth pressure was 30 Torr for the whole process. The growth on sapphire and GaAs was carried out under the same condition as the growth on Si(111). The sapphire is cleaned by O_2 plasma for 3 min before growth. GaTe (60 mg) and Ga_2Te_3 (10 mg) powders (American Elements) were mixed together as the source materials and Ar (15 sccm)+H_2 (5 sccm) is used as the

carrier gas. The tube was heated from room temperature to the growth temperature with a ramping rate of 20 ^{o}C/min. The temperature was kept stable for 5 min and then cooled down to room temperature. The Ar flow rate was set at 15 sccm and the growth pressure was 30 Torr for the whole process. For the synthesis of GaSeTe alloys, same growth parameters were used as GaSe, except that 10 mg of GaTe (or InSe) powders was placed upstream to GaSe powders with various distances to acquire controlled composition for the alloy.

2.2 Principles of Physical Properties Engineering in 2D Materials

This dissertation focuses on the engineering of a variety of physical properties of GaX, including the bandgap, lattice vibrational properties, optical properties and optoelectronic properties. The methods used here mainly include strain engineering, defect engineering and phase engineering in heterostructural alloys. The principles of these methods are discussed in the following.

2.2.1 Strain Engineering

The band structure of a semiconductor material is highly dependent on the bonding length between the nuclei, namely the lattice constant. As the atoms come together and form bonds, the energetically separated states (s, p, d orbitals) split into continuous bands due to the coupling and overlap of the electron wavefunctions. As the electron states from adjacent atoms mix, they form the occupied binding states at lower energy (valence band) and unoccupied antibinding states at higher energy (conduction band). This principle is shown as an example in diamond in Figure 2.5[65] and applies to most semiconductors. As shown in Figure 2.5, the bandgap of a semiconductor has strong dependence on its lattice constant, making it possible to perform band engineering by applying strain.

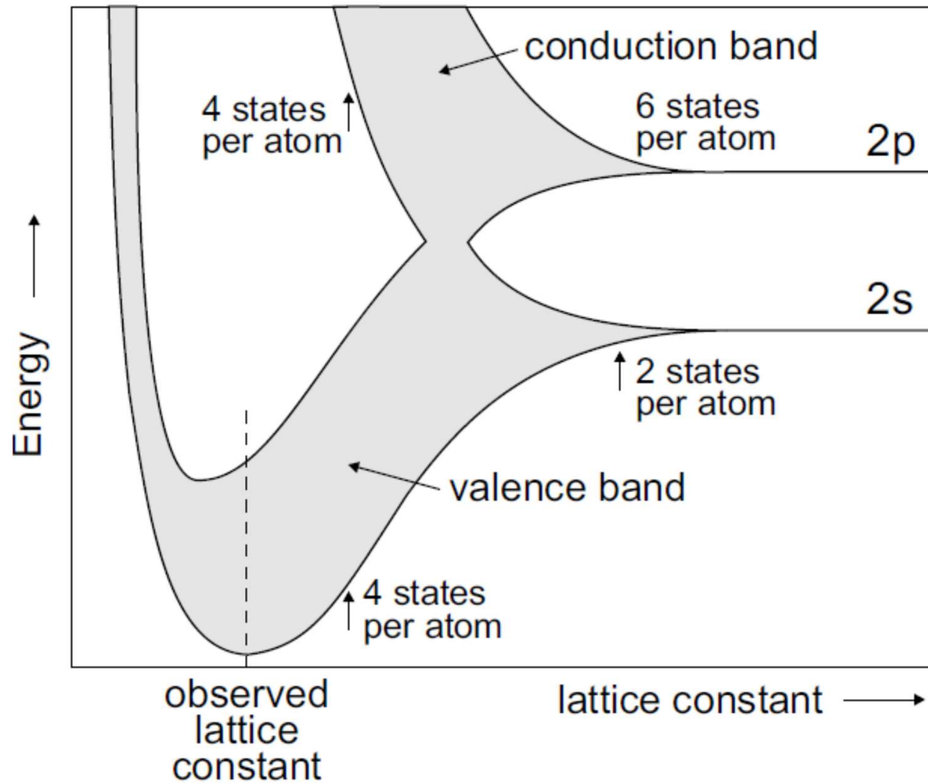

Figure 2.5 Schematic of the Electron energy levels in diamond structured carbon as a function of the lattice constant. (Figure taken from Ref. 65 © 2006, Springer-Verlag Berlin Heidelberg)

Raman spectroscopy is a powerful tool to measure localized strain with high spatial resolution. In Raman spectroscopy, the incident laser is inelastically scattered by interacting with the molecular vibrations that can be described by the harmonic oscillator model. The shift of the photon energy reflects the vibration frequency of the harmonic oscillator, which is in the form of

$$\nu = \frac{1}{2\pi}\sqrt{\frac{k}{\mu}} \tag{2.5}$$

where k is the spring constant of the harmonic oscillator and μ is the reduced mass of the atoms in the molecule, which is given by

$$\frac{1}{\mu} = \frac{1}{m_1} + \frac{1}{m_2} \quad (2.6)$$

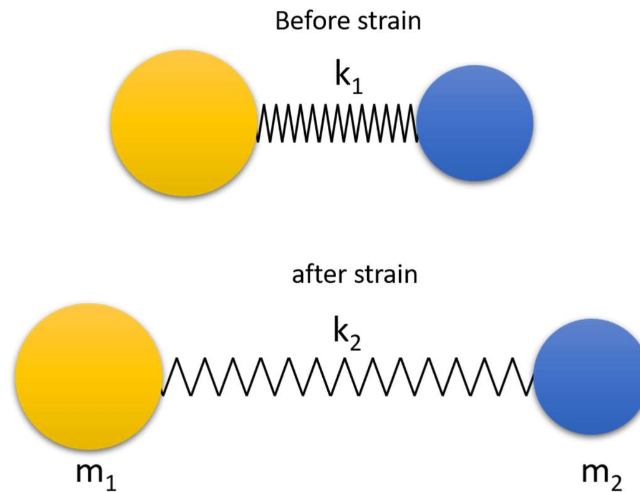

Figure 2.6 Schematic of the harmonic oscillator formed in a bi-atomic molecule before and after strain.

As seen in Equation (2.5), the vibration frequency depends on the spring constant which is affected by the distance between the atoms. In most cases, as tensile strain is applied, the atoms move away from each other and the bonding strength is reduced, resulting in smaller k and lower vibration frequency. As compressive strain is applied, the interatomic distance decreases, leading to stronger bonding and larger k, resulting in higher vibration frequency.

2.2.2 Defect Engineering

Defects have significant effect on the properties of 2D semiconductors. In a perfect crystal, each atom is located at its designated spot. But in a real crystal, the lattice deviates from the perfect structure due to the existence of defects. Based on their structure, defects can be classified into point defects, line defects and planar defects. Point defects include vacancies and interstitial atoms, which cause imperfections at a

single lattice point. Point defects can affect the electronic structure and properties of semiconductors by introducing additional electronic states within the bandgap and changing the fermi level. The additional states usually have much lower density of states (DOS) compared to the valence band and conduction band. Line defects are one dimensional (1D) defects that are formed by dislocations, where a line of atoms are out of position. Dislocations can be divided into edge dislocation and screw dislocation, as shown in Figure 2.7. Similar to point defects, dislocations can also add electronic states within the bandgap. Screw dislocations can serve as nucleation sites for heterostructural nucleation and facilitate the growth of the material, leading to screw dislocation driven growth.

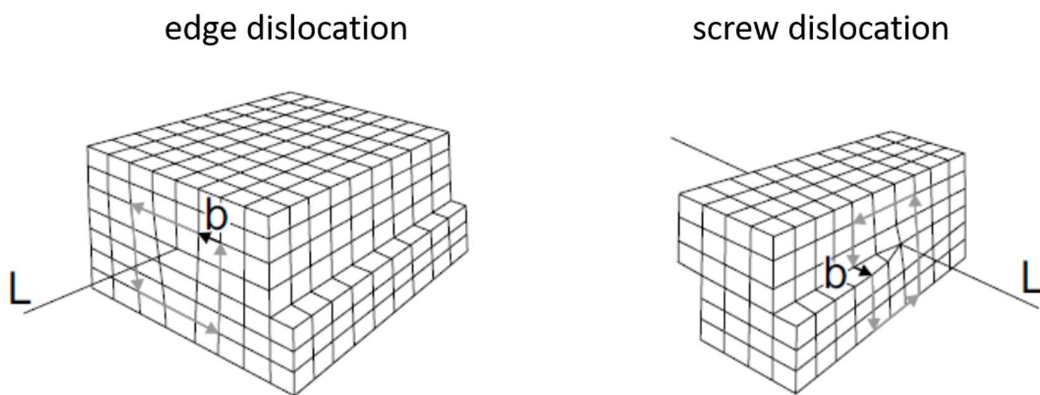

Figure 2.7 Schematics of edge dislocation and screw dislocation. (Figure taken from Ref. 66 © 2006 Springer-Verlag Berlin Heidelberg)

Planar defects include grain boundaries and stacking faults, where the displacement happens at the interface between two crystal domains or layers. Grain boundaries are usually found at the interface between two domains with different orientations. These defects can sometimes host completely different electronic structure from the matrix material, such as the metallic grain boundary in semiconducting MoS_2[67].

2.2.3 Phase Engineering in Heterostructural Alloys

Forming alloys has been a widely used approach for bandgap engineering in semiconductor materials. To achieve full composition alloys, the two components usually need to be in the same phase, as is the case for most of the thoroughly studied group III-V and II-VI semiconductor alloys. Such alloys with the same phase across the full composition are called isostructural alloys, and their bandgap changes continuously as a function of composition (Figure 2.8)[68].

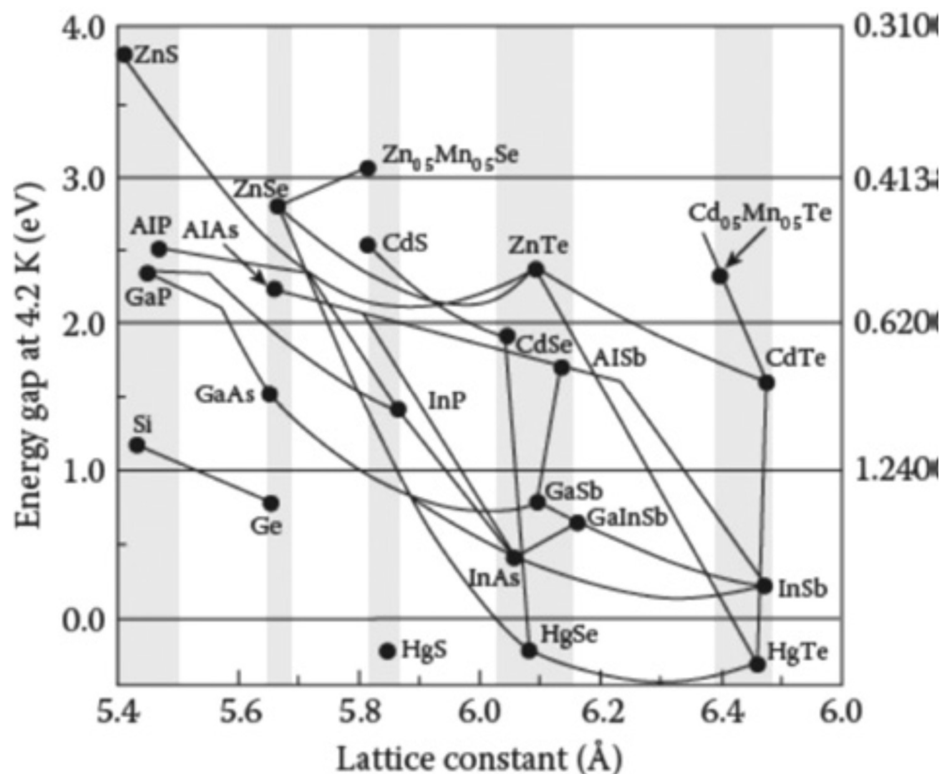

Figure 2.8 Bandgap vs lattice constant of common semiconductor alloys. (Figure taken from Ref. 68 © 2017 De Gruyter, Berlin/Boston)

Heterostructural alloys are formed by two components belonging to two different phases. As the composition changes, a structural transition from one phase to the other happens at a certain composition. Such phase transition offers a new degree of freedom in

materials design besides chemical composition, and opens up the opportunity for phase engineering[69].

However, full composition alloying typically becomes difficult in heterostructural alloys due to the structural mismatch and miscibility gaps in the phase diagram. To overcome this difficulty, we can borrow the ideas that have been used to close the miscibility gap in group III-V isotructural alloys. One way to accomplish this goal is to use the proper substrate. As the alloy is grown on a substrate, the film of the alloy strains to match the lattice parameter of the substrate, leading to the reduction in the formation free energy of the alloy[70]:

$$\begin{aligned} G &= G^{\text{ideal solution}} + \Delta G_{\text{mix}} + \Delta G_{\text{strain}} \\ &= \sum_i x_i G_i + RT \sum_i x_i \ln x_i + \Delta G_{\text{mix}} + \Delta G_{\text{strain}}(c_{ij}, \sigma, \varepsilon) \end{aligned} \quad (2.7)$$

where G_i is the partial molar free energies of the components; x_i are the mole fractions of the corresponding component; ΔG_{mix} is the free energy mixing term that describes the deviation from ideal behavior and $\Delta G_{strain}(c_{ij}, \sigma, \varepsilon)$ represents the elastic energy generated by strain. The reduction of the formation free energy can significantly reduce the phase separation critical temperature of the semiconductor alloy grown on proper substrates. In the case of GaInAs alloys as shown in Figure 2.9, the critical temperature decreases to negative across the full composition when InAs is chosen as the substrate, indicating the ability of forming full composition GaInAs alloys on InAs despite the big miscibility gap without strain.

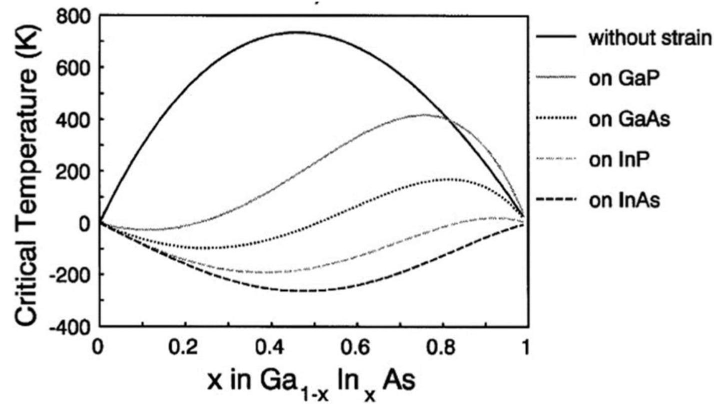

Figure 2.9 Calculated critical temperatures for the GaInAs alloy as a function of composition. The solid dark lines correspond to strain-free material. The other results assume the strains that would be induced by pseudomorphic heteroepitaxial growth on the noted substrates. (Figure taken from Ref. 70 © AIP Publishing)

Once the miscibility gap is closed, phase transition from one component to the other will be observed at a certain composition of the heterostructural alloy, allowing manipulation of the material properties through the phase engineering approach.

2.3 Experimental Methods

2.3.1 Optical Properties and Lattice Dynamics Characterization

Raman and PL spectroscopy were used to characterize the vibrational and optical properties of the samples. The experiments were carried out on a Renishaw InVia spectroscopy system with a 100x objective lens using a laser source of 488 nm wavelength. The laser was focused onto the sample with a spot diameter of 0.5 μm. Angle resolved measurements were carried out in the same system by mounting samples on a rotation stage and taking data when the sample is rotated every 20°. The incident laser and detector were polarized parallel to each other along the 0-180° direction. Low temperature PL and reflectance measurements were performed in a home-built micro-spectroscopy set-up around a closed-cycle, low vibration attoDry cryostat with a

temperature controller (T=4 K to 300K). For PL at a fixed wavelength of 633 nm a HeNe laser was used; for PL experiments as a function of excitation laser wavelength, a tunable, continuous wave Ti-Sa Laser SOLSTISF from M SQUARED was used. The white light source for reflectivity is a halogen lamp with a stabilized power supply. The emitted and/or reflected light was dispersed in a spectrometer and detected by a Si-CCD camera. For the pressure dependent studies, a home-built Raman system equipped with green laser (λ = 532 nm) and long working distance 50x optical lens was used. The data was collected using an Acton 300i spectrograph and a back thinned Princeton Instruments liquid nitrogen cooled CCD detector.

2.3.2 Morphology and Thickness Characterization

A Bruker D3100 Scanning Probe Microscope (SPM) was used for AFM measurements in ambient environment. The scanning rate was 1 Hz with a resolution of 512×512. The data was processed by Gwyddion software. Zeiss Gemini Ultra-55 field emission SEM, AMRAY 1910 SEM and Hitachi S4700 field emission SEM were employed for surface morphology observation. The Zeiss Gemini Ultra-55 was operated at an accelerating voltage of 3 kV, and the AMRAY 1910 and Hitachi S4700 were opterated at 15-20 kV with a working distance of 12-15 mm.

2.3.3 Composition and Crystal Structure Characterization

Employing a Bruker XFlash® 6|60 detector coupled with the Zeiss Gemini Ultra-55 SEM, energy-dispersive x-ray spectroscopy (EDS) and element mapping were carried out with an operating voltage of 15 kV. Nano-Auger spectroscopy (n-AES) was performed using an Oxford/Omicron Nano-Auger system that is based on an ultra-high vacuum chamber (base pressure 10^{-10} mbar) equipped with a field emission electron source and a

multi-channel hemisphere detector. The electron beam can be focused to a spot size of ~ 10 nm enabling the nanoscale chemical composition analysis on microscale GaSe structures. Also, *in-depth* n-AES studies were conducted employing the Ar ion sputtering gun attached to the instrument.

TEM and SAED experiments were performed on the FEI Titan TEM with the accelerating voltage of 300 kV. High-angle annular dark-field imaging (HAADF) was conducted using a NION UltraSTEM100 scanning transmission electron microscope (STEM). The accelerating voltage was typically set to 40 to 80 kV, and the probe size was about 0.3 nm with a probe current of approximately 12 pA. X-ray diffraction (XRD) measurements are conducted on a PANalytical X'Pert Pro Materials Research model X-Ray diffractometer with Cu-Kα radiation (1.5406 Å) using a 0.05° step size and a 2 s dwell time.

2.3.4 Density Functional Theory Calculations

Band structure calculations for GaSe under strain are based on first-principles density functional theory (DFT) using projector augmented wave potentials[71]. The exchange correlation potential has been represented by the Generalized Gradient characterized by Perdew-Burke-Ernzerhof[72] including van der Waals correction (vdW)[73] both for spin-polarized and spin-unpolarized cases. Effects of spin-orbit coupling and non-collinear magnetism are not taken into account. Supercell size, kinetic energy cut-off, Brillouin zone (BZ) samplings of the calculations have been determined after extensive convergence analysis. A plane-wave basis set with kinetic energy cut-off of 370 eV is used. In the self-consistent field potential and total energy calculations BZ is sampled by special **k**-points. The numbers of these **k**-points are (16x16x4) for the

primitive bulk ε-GaSe unit cell and are scaled according to the size of the super cells. All atomic positions and lattice constants are optimized by using the conjugate gradient method, where the total energy and atomic forces are minimized. The convergence for energy is chosen as 10^{-6} eV between two consecutive steps, and the maximum Hellmann-Feynman forces acting on each atom is less than 0.01 eV/Å upon ionic relaxation. The pressure in the unit cell is kept below 5 kBar in each lattice vectors for relax structures. The amplitude of the applied pressure in the calculations conducted under strain are kept under experimentally reachable values.

Formation energies of GaSeTe alloys were calculated using the Vienna *Ab initio* Simulation Package (VASP)[74] for density functional theory calculations. To simulate hexagonal and monoclinic $GaSe_{1-x}Te_x$ different compositions (x = 0, 1/12, 2/12, 3/12, 4/12, 6/12, 8/12, 9/12 and 1), 3x3x1 and 1x3x1 supercells were used, respectively, leading to 72 atoms in each supercell. The supercell structures were generated using the method based on the Special Quasirandom Structures (SQS) method[75] implemented in the ATAT package[76]. In the VASP calculations, the Perdew-Burke-Ernzerhof functional[72] and potentials from the projector augmented-wave method[71, 77] were used. Plane wave basis set with a cutoff energy of 500 eV were used and the *k*-point sampling grids for the supercells were set to 4x4x2 and 2x6x2 for the hexagonal and monoclinic supercells, respectively. The formation energy E_f of $GaSe_{1-x}Te_x$ is defined as $E_f = (E_{GaSe1-xTex} - E_{Ga} - (1-x)E_{Se} - xE_{Te})/2$, where $E_{GaSe1-xTex}$ refers to the energy of a $GaSe_{1-x}Te_x$ supercell per formula unit. E_{Ga}, E_{Se}, and E_{Te} denote the energies of Ga, Se, and Te atoms in their corresponding bulk unit cells. The cluster expansion method in ATAT was used

to search for possible ordered compounds with the compositions lying between hexagonal GaSe and GaTe.

CHAPTER 3 CONTROLLED SYNTHESIS AND BAND ENGINEERING OF GaSe

This chapter focuses on the vapor phase transport synthesis of 2D GaSe and the band gap tuning effect induced by lateral and vertical strain. As mentioned in previous chapter, strain induced band gap tuning has been mostly studied on exfoliated GaSe and the effect was quite limited due to the small amount of strain that can be applied through an external force. In this work, we show that the band gap of GaSe can be significantly reduced from 2 eV down to 1.7 eV by tensile strain induced by the substrate, which reaches the range of $GaSe_xTe_{(1-x)}$ alloys. The band gap can be further reduced by applying vertical strain using a diamond anvil cell (DAC) setup. Overall, results are fundamentally and technologically intriguing as the technique offers unique routes to design materials without alloying or defect engineering.

3.1 Synthesis of 2D GaSe on Si (111)

In a typical vapor phase transport (VPT) process, Ga_2Se_3 and GaSe precursors were transported to hot (growth) zone using inert Ar gas at high temperatures to deposit GaSe layers on Si(111) and sapphire surfaces. Here, Si(111) surface offers an excellent hexagonal symmetry match between the matching faces of GaSe(0001) and Si(111) that corresponds to a 2.6% lattice mismatch using the "GaSe" *a* lattice parameter of 3.74 Å and a silicon surface net parameter, $a/\sqrt{2}$ ~ 3.84 Å[78, 79, 80] (Figure 3.1).

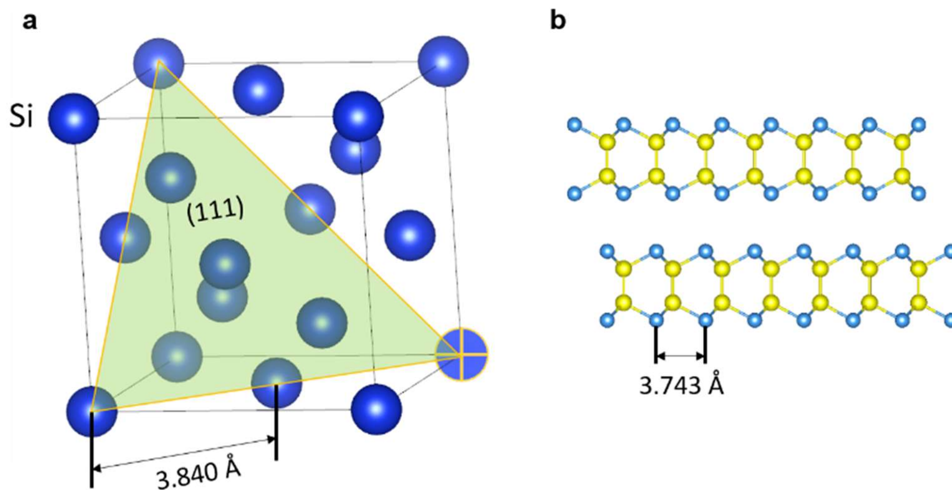

Figure 3.1 **(a)** Schematics of the interatomic displacement in Si (111) face. **(b)** Schematics of the interatomic displacement in GaSe (0001) face.

By carefully controlling the cooling rate, three different morphologies are obtained, namely flat triangle, pyramid, and spiral shapes as shown in Figure 3.2. In the growth process, samples were kept at growth temperature 750 ^{o}C for five minutes (see A→B in Figure 3.2a), and immediately after samples were cooled down to room temperature following three different paths (red, yellow, and blue lines). The first path (red curve in Figure 3.2a) predominantly produces flat triangles after rapidly cooling the furnace at a rate greater than 20 ^{o}C by simply opening tube furnace. For the second path (yellow curve), samples were cooled at a rate of 10 ^{o}C/min (B→C) within 2 min, and fast cooled (rate>20 ^{o}C) below 730 ^{o}C. Interestingly, pyramids are only formed during this process. For the third path (blue curve), samples are cooled down to 700 ^{o}C at a controlled rate of 10 ^{o}C/min and fast cooled down to room temperature below 700 ^{o}C. Flakes with spiral patterns are mostly observed after this process.

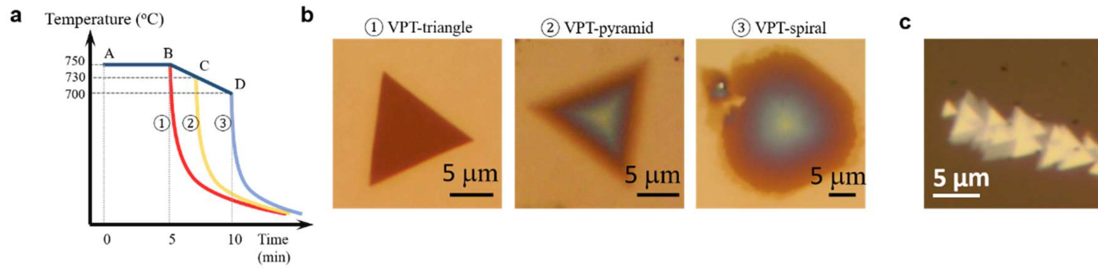

Figure 3.2 **(a)** Temperature profiles during the cooling process used in the VPT growth of GaSe. **(b)** Optical images of flat triangle, pyramid and spiral flakes of GaSe obtained by corresponding cooling process. **(c)** Optical image of VPT grown GaSe on sapphire.

In Figure 3.3, we show AFM images taken from triangular GaSe nanostructures which measures 30 nm in height with rather steep edges. A closer look at the AFM images shows that the triangle is grown on a bilayer GaSe plane measuring 1.7 nm in thickness – twice that of c-axis lattice parameter (Figure 3.3a). In contrast, pyramid flakes (Figure 3.3b) does not have sharp edges, but instead its edges make acute angle. Each step of pyramid structure is ~1.6-1.7 nm in thickness which implies that GaSe layers are grown as bilayers in Bernal (AB) stacking. Unlike others, spiral flakes (Figure 3.3c) is made of monolayer GaSe which 0.9 nm step height, and can be clearly distinguished by its striking helical fringes and spiral contours. The chemical composition measured by EDS shows the Ga:Se ratio is close to 1:1 and the elemental mapping shows both Ga and Se distribute uniformly across the flake (Figure 3.4a and Figure 3.4b). TEM measurements show that synthesized flakes are in ε-phase where layers are stacked in Bernal stacking arrangement (Figure 3.4c, Figure 3.4d and Figure 3.4e).

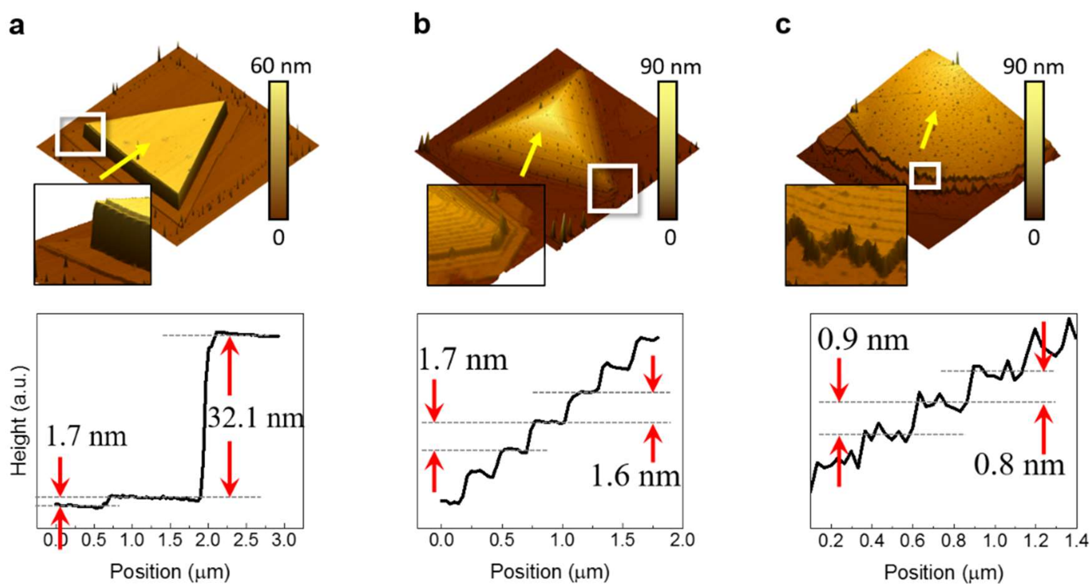

Figure 3.3 AFM images and height profiles of flat triangle **(a)**, pyramid **(b)** and spiral **(c)** GaSe flakes. The height profiles are taken from positions indicated by the yellow arrows.

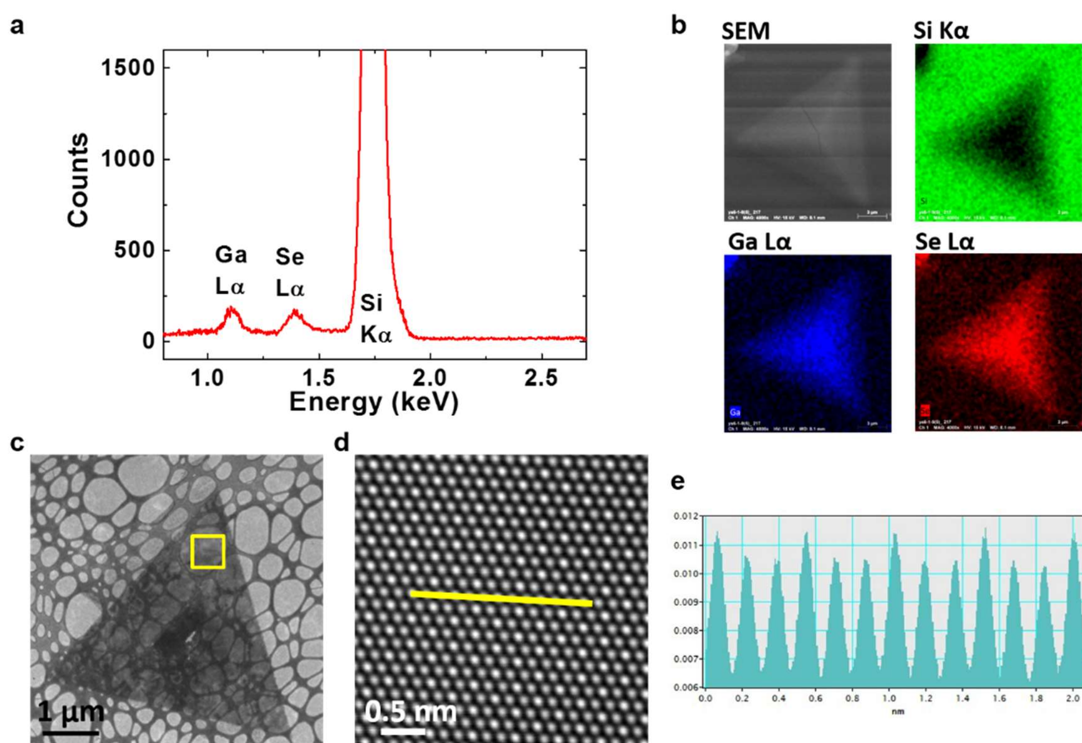

Figure 3.4 **(a)** EDS spectrum of a VPT grown GaSe pyramid on Si. **(b)** EDS mapping of a VPT grown GaSe pyramid on Si. **(c)** Low magnification image of a VPT grown GaSe triangle. **(d)**

HAADF image of the selected area in (c). **(e)** Intensity profile along the yellow line in (d), indicating the ABAB stacking of GaSe.

What is the origin of such vastly different morphologies and relation to growth conditions? The synthesis of crystalline nanomaterials must follow basic crystal growth theory, describing the layer-by-layer (LBL -also called Frank van der Merwe-) dendritic growth[81], and spiral screw-dislocation driven (SDD) growth[82, 83]. In this work, triangle and pyramid features are in the LBL regime due to their highly layered / stacked nature, whereas spiral flakes are grown by SDD. The latter is particularly evident from spiral patterns in AFM images (Figure 3.3c) which is a signature morphology observed in SDD grown low-dimensional materials. Within the crystal theory, dentritic-LBL-SDD growth regime depends on the degree of supersaturation which is expressed as $s=\ln(c/c_0)$ where c and c_0 are the precursor and equilibrium concentration values[84]. We postulate that triangle features are grown at 750 ºC (A→B in Figure 3.2a) when the precursor concentration is higher –due to higher vapor pressure- and s value is high enough to sustain LBL growth. Upon rapid cooling, growth temperature quickly drops below 700 ºC (above which GaSe layers are grown), bypassing B→C and C→D temperature regions (Figure 3.2a), and thus almost no growth takes place below 750 ºC. However, when the temperature is slowly cooled from 750 to 730 ºC (B→C), precursor concentration s, and step growth velocity slowly decreases. Combination of these factors are still sufficient to sustain LBL growth (as evidenced by layered nature of pyramids), but resulting materials assume pyramid shapes due to reduced and time / temperature. Finally, spiral features are realized at low temperature (C→D), low concentration precursor and s conditions. In this regime, nuclei formation –which is essential to LBL growth- is not preferred as the

supersaturation concentration is below its critical value, instead screw dislocations offer active sites with relatively large Gibbs free energies and SDD growth dominates in the C→D range. Since each layer measures monolayer (0.9 nm) in spiral features, as opposed to bilayers in triangles and pyramids, we argue that screw dislocations are probably formed by uplifted layers on the surface.

3.2 Band Gap Engineering by Lateral Strain

Photoluminescence (PL) spectroscopy is used to study the optical properties of the VPT synthesized GaSe. By using a confocal laser scanning microscope with a 500 nm laser spot size, we are able to perform PL mapping on the GaSe flakes and study the spatial variation of PL peak energy and intensity. Figure 3.5b and Figure 3.5e shows the PL mapping pattern of a VPT synthesized GaSe flat triangle flake (Figure 3.5a) compared to an exfoliated flake (Figure 3.5b). Interestingly, the VPT GaSe flake shows a large variation in both PL emission energy and intensity across the whole flake, whereas the exfoliated flake shows a rather uniform pattern. PL spectra taken from individual spots are plotted in Figure 3.5c, which shows a significant red shift for the VPT GaSe flake compared to the exfoliated flake. The emission range covers from 630 nm to 700 nm which corresponds to almost the same spectral range attained by alloying Se with Te in $GaSe_xTe_{(1-x)}$ ternary systems[55] as shown in Figure 3.5f. Similar studies on pyramid and spiral shaped flakes reveal the same red-shifted emission features as shown in Figure 3.6a. Considering such broad range of band gap variation, we refer to this effect as '*colossal band gap renormalization*'.

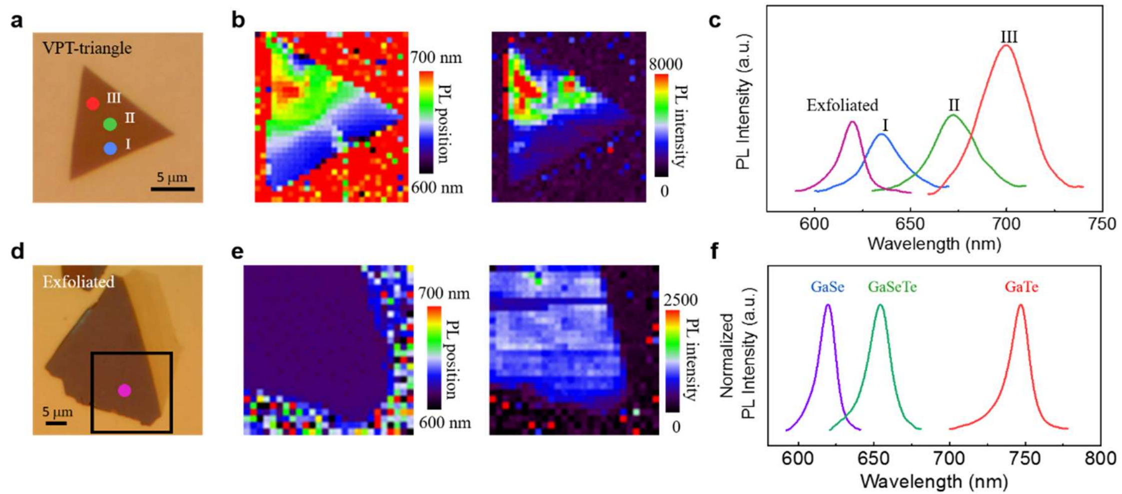

Figure 3.5 **(a)** Optical image of a VPT synthesized GaSe triangle flake. **(b)** PL peak position and intensity mapping of the GaSe flake in (a). **(c)** PL spectra of the exfoliated flake and the VPT synthesized triangle, taken at locations pointed in (a) and (d) by dots with corresponding colors. **(d)** Optical image of an exfoliated GaSe flake. **(e)** PL peak position and intensity mapping of the GaSe flake in (d). **(f)** Normalized PL spectra of bulk GaSe, GaSeTe alloy and GaTe crystals.

To further understand the band gap renormalization effect, a large number of PL spectra have been taken and the full width at half maximum (FWHM) vs emission wavelength is plotted in Figure 3.6b. Results show that the PL peak position of triangle and pyramid GaSe flakes ranges in the 630-700 nm and 640-700 nm respectively, whereas PL spectrum of spiral GaSe appears in close proximity to 680 nm with narrow PL distribution (+/- 10nm). We note that PL peak position of exfoliated GaSe and VPT GaSe on sapphire both have very small variation, s_{PL}<4nm, but emission lines are located at 620 nm and 630 nm which matches to the theoretically predicted and experimentally established values of GaSe. These trends can be clearly observed from PL peak position and intensity mapping data collected from various GaSe flakes in Figure 3.5 and Figure 3.6. For example, spiral and exfoliated GaSe flakes possess relatively uniform PL intensity whereas emission intensity is largely non-uniform on triangles and pyramids.

Furthermore, PL intensity from VPT GaSe appear more luminescent compared to exfoliated ones.

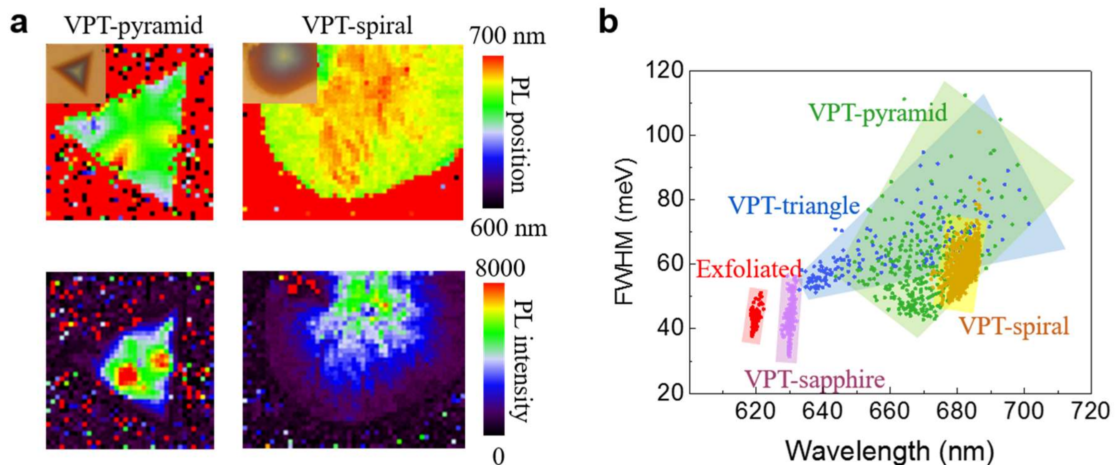

Figure 3.6 **(a)** PL peak position and intensity mapping of the pyramid and spiral shaped GaSe flake. **(b)** Distribution of PL FWHM as a function of peak position for each case. The quadrilaterals are for eye-guidance.

The question arises: What is the origin of such large band gap change? Our results cannot be explained by a simple band renormalization due to quantum confinement effects since any change in the band gap value becomes noticeable when the number of layers is less than 4 (~4 nm) which is far thinner than synthesized flakes[36]. Nor the spatial variation of PL peak and intensity can be explained by size confinement effects in the band structure since the thickness of GaSe features are either uniform (triangles) or the surface morphology / thickness does not correlate to observed PL peak/intensity distribution (pyramids). Another potential explanation might be non-stoichiometric elemental distribution across GaSe flake resulting in bound excitons ($X_D \rightarrow D+eh$) trapped at various chalcogen vacancy sites with different light emission energy. However, nano-scale energy dispersive x-ray spectroscopy (EDS) reveals that 1:1 Ga/Se

ratio is perfectly retained on the flake (Figure 3.4). Lastly, band alignment across Si and GaSe is also not possible to yield red-shifted PL since these results are specific to VPT grown samples on Si, and exfoliation onto Si(111) does not yield similar response. Colossal PL change, however, can be attributed to substrate induced strain effects on GaSe nanostructures as evidenced by micro-Raman spectroscopy measurements and DFT calculations[85, 86, 87].

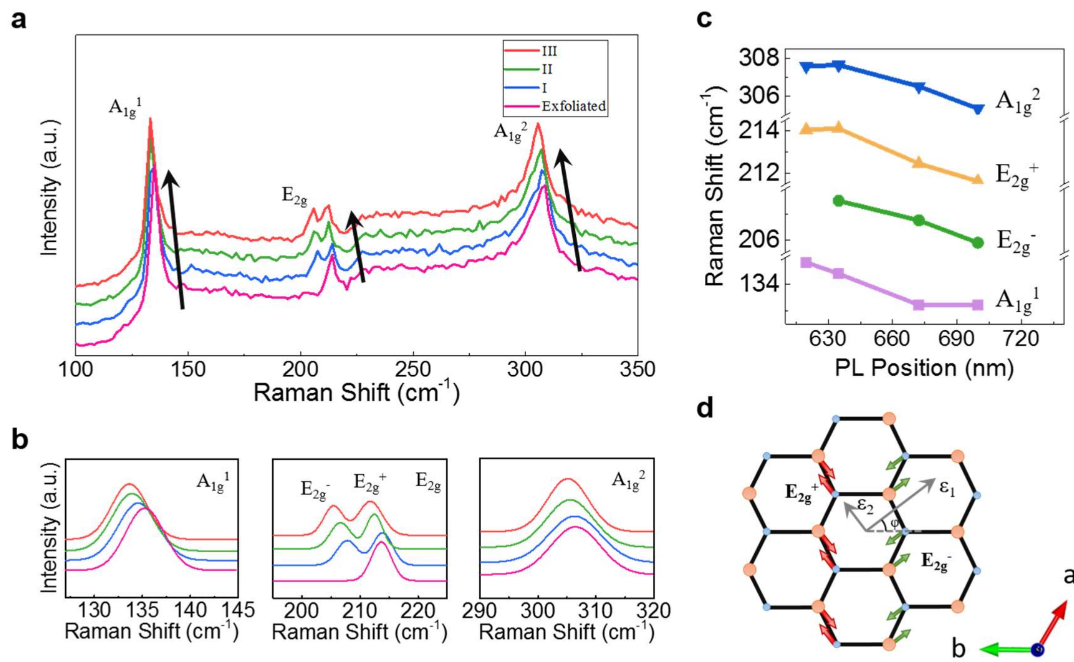

Figure 3.7 **(a)** Raman spectra of the VPT synthesized GaSe triangle taken at locations indicated by the dots in Figure 3.5a with corresponding colors. The result is compared to an exfoliated (unstrained) GaSe flake in Figure 3.5d. **(b)** Fitted spectra of the vibration modes of A_{1g}^1, E_{2g} and A_{1g}^2 on exfoliated and VPT synthesized triangle. **(c)** The shift of each vibration mode as a function of PL peak position as shown in Figure 3.5c. **(d)** Schematics of the vibrational property of in-plane biaxial strained GaSe.

We argue that band renormalization effect originates from finite tensile strain acting on vdW deposited GaSe/Si(111) flakes. Micro-Raman studies on triangular GaSe flakes

show that three prominent vibrational modes (A_{1g}^1, E_{2g}, and A_{1g}^2 located near 135 cm^{-1}, 214 cm^{-1} and 307 cm^{-1}, respectively) are significantly softened compared to exfoliated GaSe (Figure 3.7a-c). Here, we note that triangular flakes offer ideal platform to perform Raman characterization owing to their uniform thickness and flat morphology. Even though presented results are acquired from triangles, similar findings have also been reproduced for many spiral and pyramid GaSe samples. Red-shifted Raman peaks clearly implies that a finite tensile strain exists on GaSe/Si(111) compared to unstrained exfoliated GaSe[87].

Further evidence for finite in-plane strain comes from lifted degeneracy of E_{2g} mode[88]. This mode, described by a single Lorentzian peak on exfoliated GaSe flakes, splits into two components, namely E_{2g}^- and E_{2g}^+, for VPT GaSe (Figure 3.7b). In its unstained state the E_{2g} mode consists of two degenerate modes: one polarized in the *a* axis and another in the *b*-axis direction. But with finite strain at any arbitrary angle, the degeneracy of E_{2g}^- and E_{2g}^+ peaks is lifted, and each peak shifts by a different amount depending on the direction of the strain axis with respect to *a* and *b* lattice vectors (Figure 3.7d). This picture is further supported by similar findings on strain / E_{2g} mode splitting relations observed on other material systems, such as CNTs, graphene, and more recently MoS_2[87, 88].

Importantly, Raman peaks gradually red-shift going from point I to III (see flake and labelling in Figure 3.5a and Figure 3.5d), suggesting that the magnitude of the strain is not uniform across the flake. PL mapping on the same flake reveal that peak position is red-shifted and PL intensity much increased in the same direction (I to III). Thus, we argue that PL peak shift and band gap change is directly linked to the amount of strain

within each flake (Figure 3.7c), and PL mapping gives a reasonable information on nanoscale strain distribution on the flake. Here, we note that strained parts have stronger emission possibly due to exciton immigration / diffusion from unstrained (larger band gap) regions to strained parts through funneling effect (Figure 3.8a)[53]. Proposed in-plane tensile strain picture is also consistent with the first principles results (Figure 3.8b) which shows that band gap decreases (by 0.18 eV/%) in the tensile strain direction, whereas compressive strain increases the band gap by 0.11 eV/1 % strain. From the dE_{gap}/ds relation in Figure 3.8b, together with largest measured PL peak shift (2.0 eV for exfoliated GaSe to 1.7 eV for GaSe triangles), the maximum value of the in-plane tensile strain is estimated to be 2% which is the room temperature mismatch (2.6%) between Si(111) and GaSe.

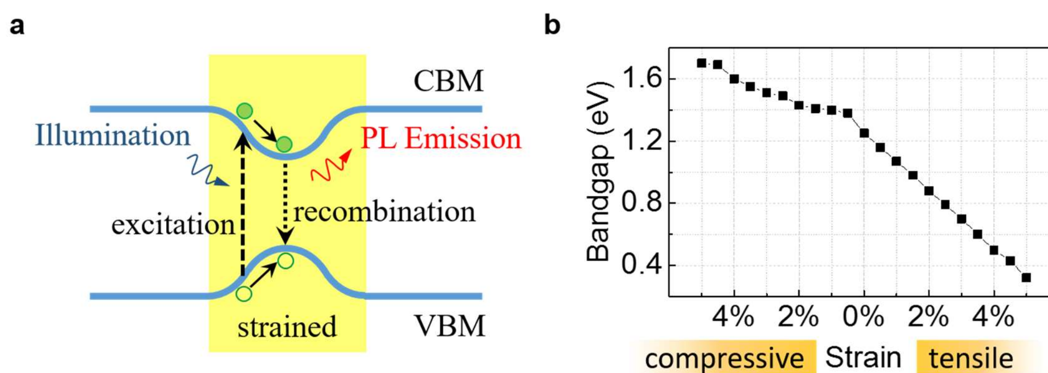

Figure 3.8 **(a)** DFT calculated bandgap as a function of strain. **(b)** Schematic diagram of the funnel effect caused by non-uniform strain.

Due to a larger lattice mismatch between GaSe and sapphire (21%), vdW epitaxy on sapphire produces GaSe flakes with physical properties close to exfoliated ones (Figure 3.6b) –PL peak is shifted only by 10 nm–, and underlying substrate does not induce any strain on the flakes. Consequently, vdW epitaxy on sapphire produces flakes with narrow

PL distribution (similar to exfoliated ones) whereas GaSe triangles and pyramids on Si span much larger energy range due to non-uniform strain distribution. The only exception to this trend is observed on spiral GaSe flakes on Si(111) where its PL peak position is significantly red-shifted and is well defined. Since the SDD growth is driven by misplaced edges and kinks due to lower activation energies, uniform PL peak distribution can be attributed to uniform strain profile on spiral flakes. Overall results are surprising since i) GaSe layers are perfectly passivated thus interaction with the underlying substrate is expected to be minuscule regardless from the substrate's chemical state, ii) even if there is a finite strain acting on GaSe layers, it is unlikely to transfer strain from one layer to another through weak vdW forces between adjacent layers. In this view, strain is anticipated to act only on the first few layers and PL / Raman measurements (which collects signal with equal weighting factor across the thickness) should –in principle- probe mostly unstrained regions. Considering results on Si(111), sapphire, and exfoliated flakes, underlying substrate plays an essential role in determining the material behavior of GaSe, especially when the substrate surface is not passivated as in the case of Si(111). One potential explanation is that Si atoms interact strongly with nucleated GaSe, and strain is carried onto GaSe layers during lateral diffusion process due to finite -but small- lattice mismatch.

3.3 Effect of the Vertical Compressive Strain

Further band gap tuning can be obtained by applying vertical strain. In contrast to conventional DAC setup where hydrostatic pressure acts both in- and out-of-plane directions, we have applied compressive vertical pressure (Figure 3.9a) up to ~0.3 GPa on both exfoliated and VPT grown GaSe flakes and monitored the shift in Raman

frequencies and PL peak position. The pressure is estimated from the Si Raman peak shift (Fig 3.10b-c).

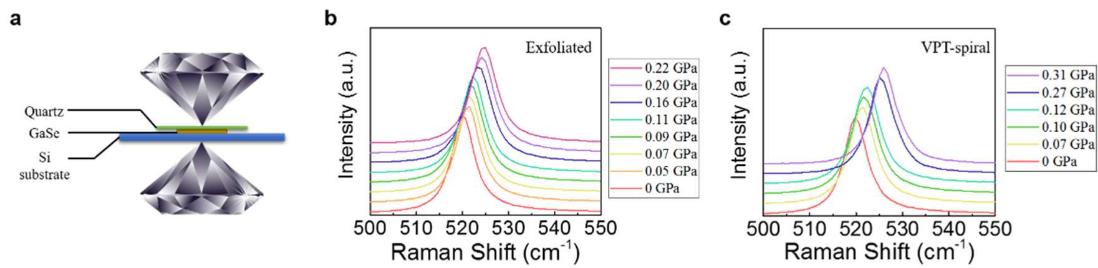

Figure 3.9 **(a)** Schematic of the experimental setup using a diamond anvil cell. **(b-c)** Pressure-dependent Raman spectra of the Si substrate for exfoliated GaSe (b) and VPT grown spiral GaSe (c). The pressure is estimated by the shift amount of the Si peak using a previously established relation[89].

If GaSe on Si(111) has a finite amount of tensile strain, we anticipate that GaSe layers will be easier pushed closer to each other at a given pressure due to increased bond length reducing the change density around individual GaSe layers and repulsion force between adjacent layers. Since the band gap and PL peak position strictly depends on the interlayer coupling, PL peak position of GaSe/Si(111) is expected to have stronger pressure dependence compared to exfoliated ones.

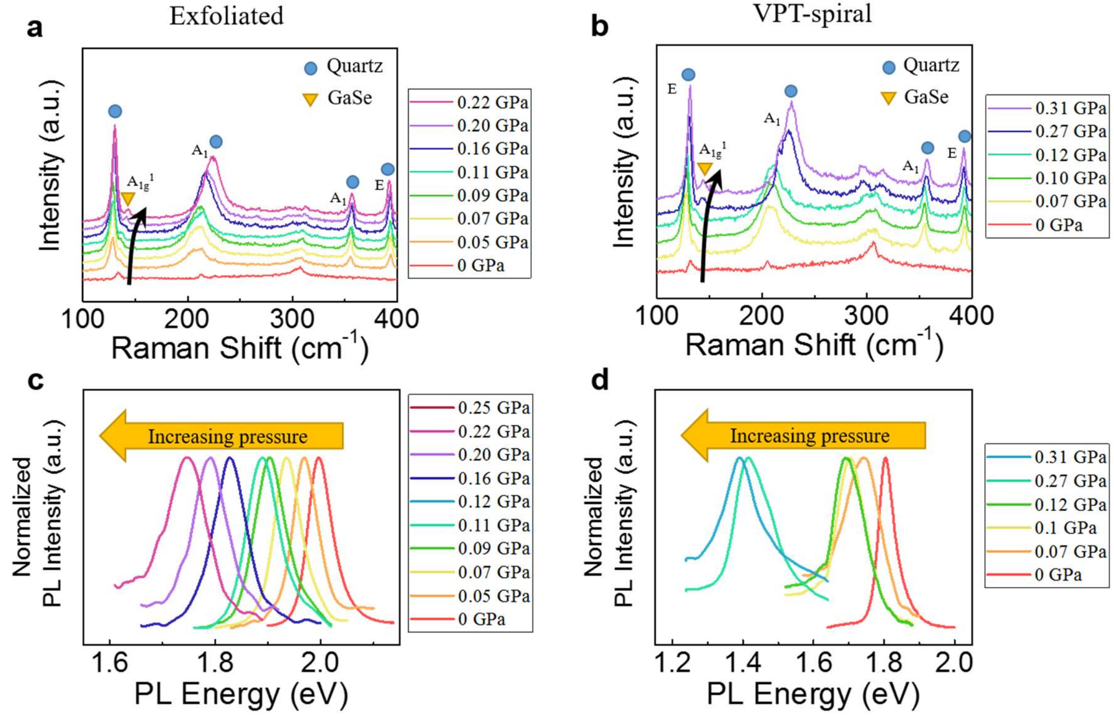

Figure 3.10 **(a)** Pressure-dependent Raman spectra of exfoliated GaSe. **(b)** Pressure-dependent Raman spectra of VPT synthesized spiral flake. **(c)** Pressure-dependent PL spectra of exfoliated GaSe. **(d)** Pressure-dependent PL spectra of VPT synthesized spiral flake.

Owing to the uniformity of the PL peak position, spiral GaSe/Si(111) is selected over triangle and pyramid features for DAC measurements, and its pressure response is compared to exfoliated GaSe flakes as shown in Figure 3.10. Upon applying pressure on spiral GaSe/Si(111) in DAC setup, Raman peaks gradually stiffen as shown in Figure 3.10a-b, suggesting that the applied pressure is successfully transferred to GaSe. PL spectroscopy and m-DAC measurements reveal that PL peak red-shifts for both GaSe/Si(111) and exfoliated GaSe due to pressure induced band renormalization. PL peak of GaSe flakes scales linearly with applied vertical pressure, however spiral flakes appear to be more sensitive (dE_{gap}/dP = -1.43 eV/GPa) to the vertical pressure compared to exfoliated ones (dE_{gap}/dP = -1.17 eV/GPa) as shown in Figure 3.11a-b. Here, it is

worthy to mention that observed difference in the pressure dependence is quite large in comparison to other material systems. For instance, GaN and GaAs belong to the $P6_3mc$ and $F\bar{4}3m$ symmetry groups and dE_{gap}/dP only differ by 0.066 eV/GPa[90, 91, 92].

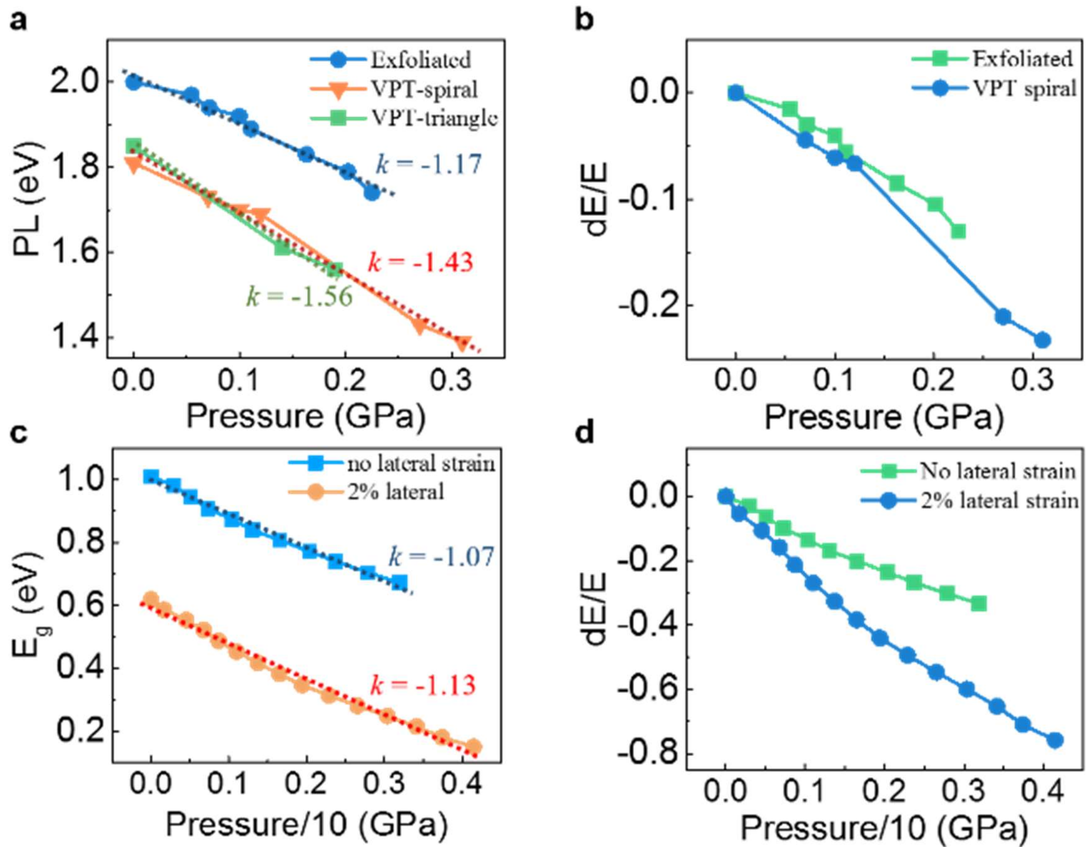

Figure 3.11 **(a)** Band gap as a function of pressure for exfoliated and VPT synthesized triangle and spiral flakes. Dashed lines are linear fits to each set of data. **(b)** Ratio of band gap change as a function of vertical pressure obtained from (a). **(c)** DFT calculated band gap as a function of pressure for strained and unstrained GaSe. **(d)** Ratio of band gap change as a function of vertical pressure obtained from (c).

The effect of pressure on the optical band gap of GaSe can be further understood by density functional theory (DFT) calculations. Figure 3.11c-d shows the band gap of GaSe as a function of vertical pressure obtained by DFT calculations for unstrained (exfoliated) and 2% tensile strained (VPT grown) GaSe layers. Results show that calculated band gap

decreases much faster (is more sensitive) for tensile strained GaSe spiral nanostructures, and agree well with our experimental findings. Linear fitting of the calculation results gives a dE/dP slope difference of 17%, which is similar to the experimental result of 22%.

3.4 Summary

This chapter demonstrates collosal band renormalization effect in GaSe layers grown onto Si(111) surfaces via van der Waals epitaxy. The band gap spans 630-700 nm range which is significantly red-shifted compared to exfoliated GaSe (620 nm) and covers almost the same spectral range as $GaSe_xTe_{(1-x)}$ ternary alloys. Interestingly, vdW epitaxy on sapphire or GaSe exfoliation onto Si(111) do not yield similar results, suggesting that interaction between Si(111) and GaSe layers play a crucial role especially during nucleation and diffusion of GaSe. Through control over kinetic factors, we were able to synthesize desired GaSe morphologies and attain modest control over emission wavelength. Raman spectroscopy, diamond anvil cell pressure studies, PL spectroscopy, and computational calculations suggest that tensile strain on GaSe layers, arising from interaction between Si and GaSe, results in observed band renormalization effects. Findings open new venues to design new material properties from the same material itself and offers new insights to vdW epitaxy of lamellar materials.

CHAPTER 4 SYNTHESIS AND NOVEL PROPERTIES OF GaTe

This chapter studies the vapor phase transport synthesis of GaTe on various substrates including GaAs (111), Si (111) and sapphire. Results show that substrate type has a crucial effect on the growth mechanism and the consequent morphology and properties. Using high-resolution transmission electron microscopy (HRTEM), we provide atomic images of the pseudo-1D chain-like structure in GaTe, and report on their anisotropic properties using angle resolved micro-PL and micro-Raman spectroscopy techniques. In terms of optical properties, the GaTe flakes synthesized on sapphire not only show a strong band edge PL emission at 1.66 eV, but also display multiple sharp emissions in the forbidden gap. Detailed PL mapping and temperature and power dependent PL measurements are used to study the emission mechanism of these peaks.

4.1 Synthesis and Structural Characteristics of Nanostructured GaTe

GaTe flakes were synthesized by VPT technique in a tube furnace using GaTe and Ga_2Te_3 polycrystalline powders as the source. The setup is similar to the one used in the GaSe growth discussed in the previous chapter (Figure 2.1). We have performed the growth on a variety of substrates including GaAs (111), Si (111) and c-cut sapphire to understand different substrate effects and growth mechanism. Here, GaAs and Si wafers were selected in order to integrate 2D materials systems into scalable bulk semiconductors in hybrid structures, and sapphire was chosen owing to recent successful growth of 2D systems onto their highly crystalline surfaces.

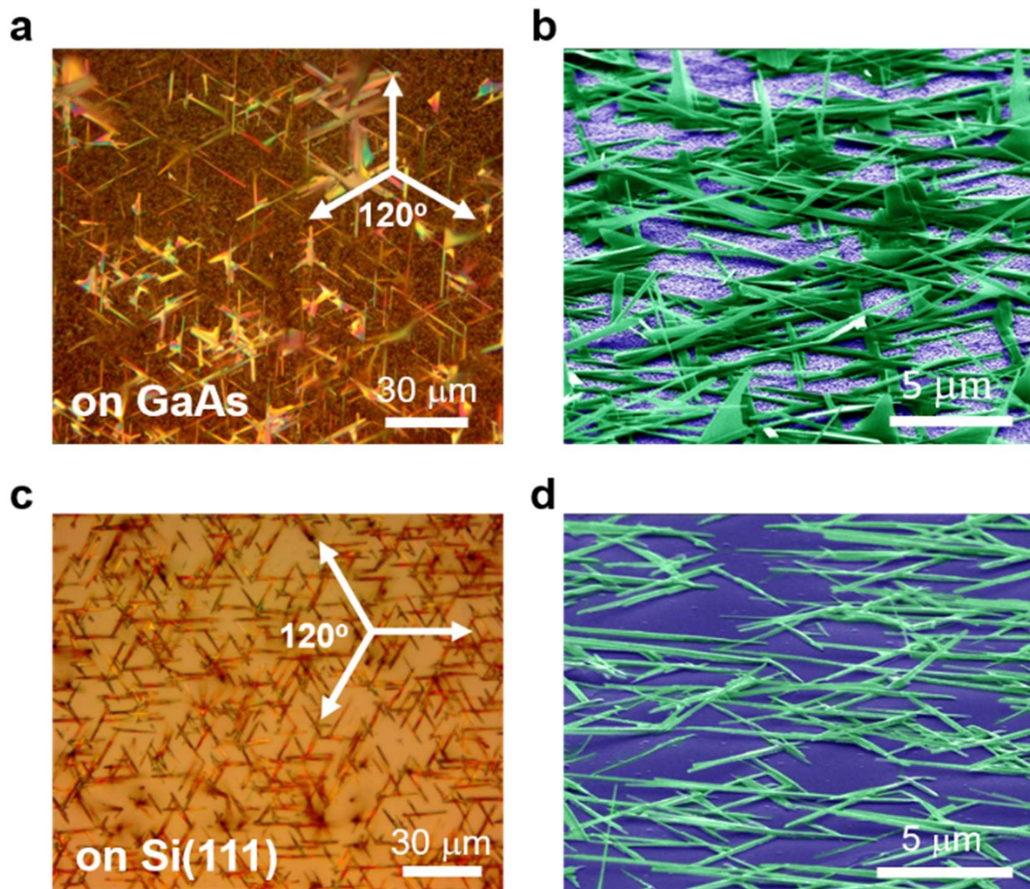

Figure 4.1 **(a-b)** Optical (a) and false colored SEM (b) images of GaTe synthesized on GaAs (111) substrate. **(c-d)** Optical (c) and false colored SEM (d) images of GaTe synthesized on Si (111) substrate.

GaTe is first synthesized on GaAs (111) and Si (111) substrates. As shown in Figure 4.1, the morphology of the GaTe nanostructures depends strongly on the substrate type. Typical growth processes carried onto GaAs and Si yield GaTe nanowires lying flat on the surface, however some of the ribbons also grow out of plane at an acute angle with the substrate as shown in scanning electron microscopy (SEM) images in Figure 4.1b and Figure 4.1d. These nanowires appear to be well aligned along three directions that make a fixed angle of 120° with each other, which is a sign of epitaxial growth[93]. To confirm

epitaxial relationship between GaTe and GaAs, we have performed pole figure X-ray diffraction (XRD), SEM and HRTEM combined. A full XRD spectrum of the sample is shown in Figure 4.2a. GaAs (111) and (222) peaks are clearly seen, confirming the (111) orientation of the GaAs substrate. As for GaTe, only two peaks are revealed-the (001) peak at 11.9^{o} and the (002) peak at 23.8^{o}. This suggests that the GaTe nanowires have a (002) preferred vertical orientation on GaAs(111). The pole figure XRD result shown in Figure 4.2b further confirms that the GaTe (002) plane is parallel to the GaAs (111) plane (Figure 4.2c).

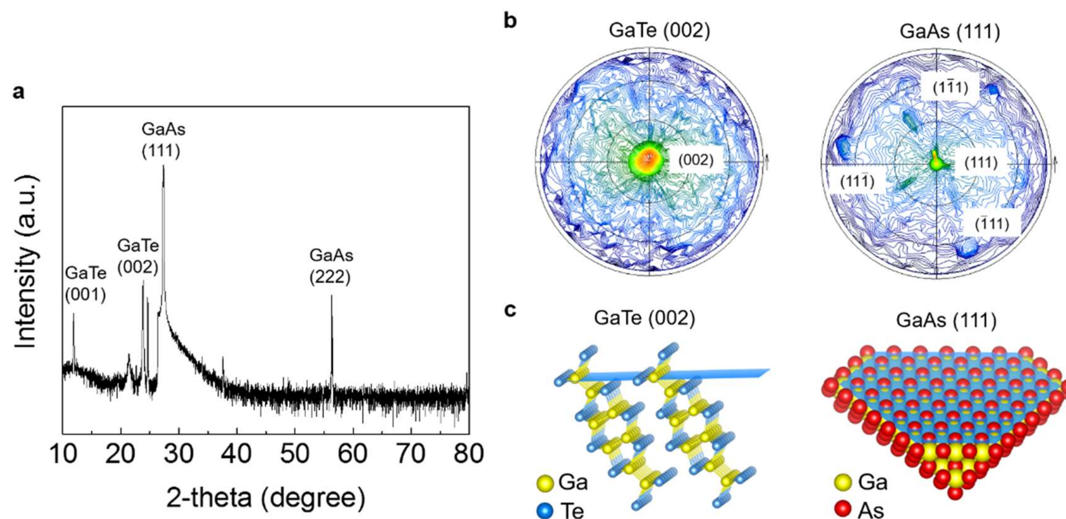

Figure 4.2 **(a)** XRD spectrum of GaTe grown on GaAs (111). **(b)** Pole figure XRD spectra of the GaTe (002) plane and the GaAs (111) plane system. **(c)** The atomic structure of both planes shown in (b).

Next, we determine the rotational relationship between the GaTe nanowires and the GaAs substrate by analyzing the angle of the nanowire growth. Figure 4.3a shows the SEM image of the GaTe nanowires grown at the edge of the GaAs wafer. It is known that the GaAs (111) wafer cracks along the [110] direction. We find that the nanowires form a 30° angle with respect to the wafer edge, which is parallel to the [121] direction of GaAs

(Figure 4.3c). HRTEM image (Figure 4.3b) shows that the nanowire growth direction is along the [010] chain direction of GaTe. Thus the rotational relationship between GaTe and GaAs is determined as GaTe [010]//GaAs [121]. Finally, a 3D structure of the GaAs-GaTe system is constructed as shown in Figure 4.3d. It is worthy to note that the growth of GaTe is quite different in that instead of isotropic growth (i.e., material grows in all directions in the plane), monoclinic GaTe growth occurs preferably along the [010] chain direction. This chain-like growth is directly related to the highly anisotropic crystal structure[94] of monoclinic GaTe and will be discussed later in the article. Here, we also note that similar relations also exist for GaTe grown onto Si wafers but are not shown here for brevity.

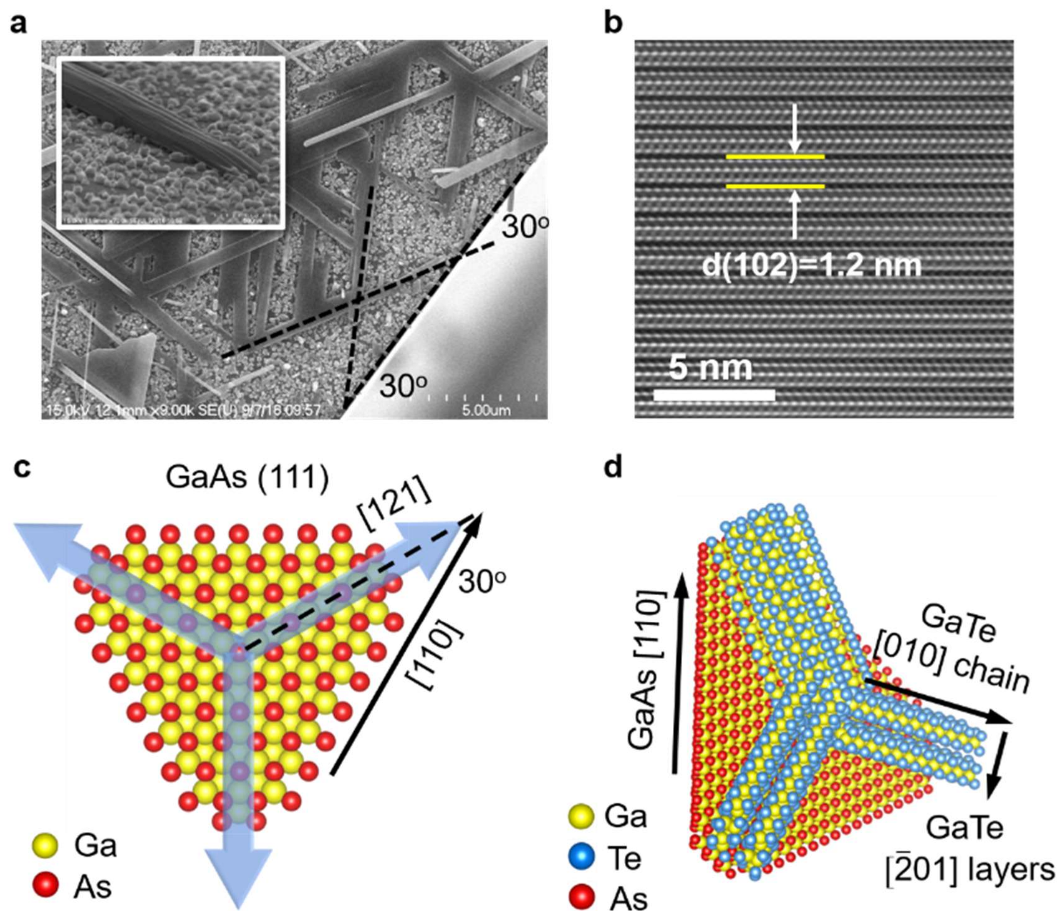

Figure 4.3 **(a)** SEM image of GaTe grown at the edge of the GaAs (111) substrate. inset: Zoom-in view of a GaTe nanowire grown on GaAs (111). **(b)** HRTEM image of the VPT grown GaTe that shows the chain structure. **(c)** atomic structure of the GaAs (111) surface with the GaTe nanowire growth direction labeled by blue arrows. **(d)** 3D atomic model of the GaTe nanowires grown on GaAs (111).

However, due to the large lattice mismatch of 13.7% between GaTe (4.15 Å of Te-Te distance along [010]) and sapphire (4.81 Å along [010]) compared to 2.0% and 7.2% on GaAs ($d_{As\text{-}As}$=4.07 Å along [110]) and Si ($d_{Si\text{-}Si}$=3.87 Å along [110]) respectively, GaTe flakes grow rather randomly on sapphire substrates as shown in Figure 4.4a. The resulting morphology varies from wires to flakes with the dimensions ranging from 10 μm to 30 μm. This random distribution of morphology and dimension may be attributed

to the van der Waals epitaxy growth mechanism where the GaTe is bonded to the substrate by weak van der Waals force without forming any direct chemical bonds. Under this regime, the GaTe adatoms can transport more freely on the sapphire surface. Overall our manufacturing route enables synthesis of pseudo-1D GaTe sheets for the first time onto different substrates and is a significant progress in synthesis of pseudo-1D systems.

4.2 Optical Properties of VPT Deposited GaTe

To understand how substrate type and growth characteristics influence the overall optical response from direct band gap nanomaterial GaTe, we have performed photoluminescence (PL) measurements as shown in Figure 4.4b. We find that the GaTe flakes grown on sapphire behave quite differently from those grown on GaAs and Si as well as flakes isolated from GaTe single crystals synthesized via Bridgman method. The main PL peak located at 1.66 eV for GaTe/sapphire (red) and GaTe/GaAs (green) matches closely the fundamental direct band gap of GaTe at 1.65 eV (blue line), and is thus identified as the band edge emission (X_0) related to radiative recombination of photo-excited electrons and holes. The sample grown on GaAs displays an additional peak at 1.42 eV (green line) originating from the GaAs substrate (E_g^{GaAs}=1.4 eV). Surprisingly, however, the sample grown on sapphire (red line) shows three additional sharp (FWHM~50 meV) emission lines at 1.29 eV, 1.39 eV and 1.50 eV as pointed out by the blue arrows which are not present in exfoliated GaTe and GaAs/GaTe samples. Then the question arises: What is the origin of these additional peaks?

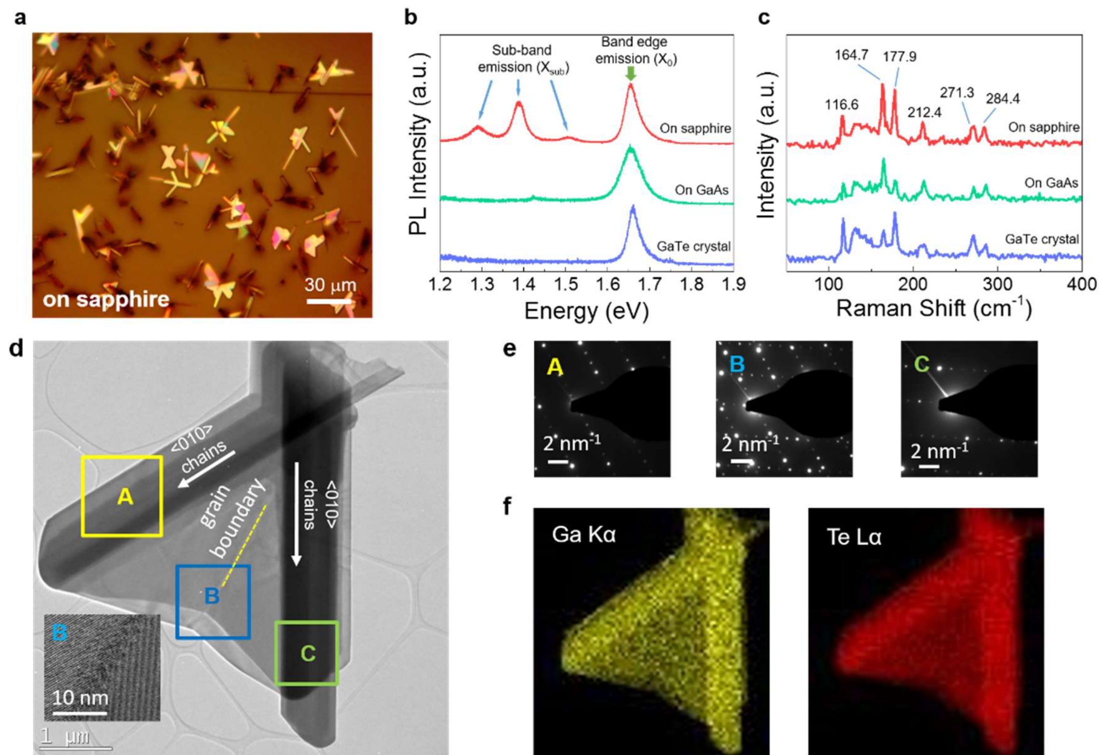

Figure 4.4 **(a).** Optical image of GaTe synthesized on c-cut sapphire substrate. **(b)** Photoluminescence spectra of GaTe synthesized on various substrates. **(c)** Raman spectra of GaTe synthesized on various substrates. **(d)** Low magnification TEM image and HRTEM image of the B area (inset). **(e)** selected area electron diffraction (SAED) pattern of a GaTe flake synthesized on sapphire. The SAED patterns are taken at three different regions marked by the squares in the TEM image. **(f)** EDS mapping of Ga and Te taken on the GaTe flake.

As evidenced by micro-Raman measurements, we safely exclude the presence of secondary phases such as Ga_2Te_3 or TeO_2 and their potential impact on the PL spectrum. As shown in Figure 4.4c, Raman spectra from sapphire/GaTe precisely match the GaTe single crystals grown by the Bridgman method, GaAs/GaTe, as well as existing literature without any additional peaks associated with other compositions and phases[95]. The Raman measurements were performed on various spots and none of them showed the possible existence of a second phase. Another direct evidence for single phase GaTe comes from our selected area electron diffraction (SAED) patterns and energy dispersive

X-ray spectroscopy (EDS) mapping in large areas on a GaTe flake synthesized on sapphire (Figure 4.4d-f). In agreement with our earlier Raman data, the SAED shows the flake is pure crystalline GaTe without any second phases. The EDS mapping also indicates a uniform distribution of Ga and Te elements. However, the SAED does suggest that the flake is poly-crystalline and is composed of two domains with different crystal orientations, which will be discussed later with the anisotropy properties. The high resolution transmission electron microscopy (HRTEM) image (Figure 4.4d inset) also proves the high crystallinity of the GaTe flake.

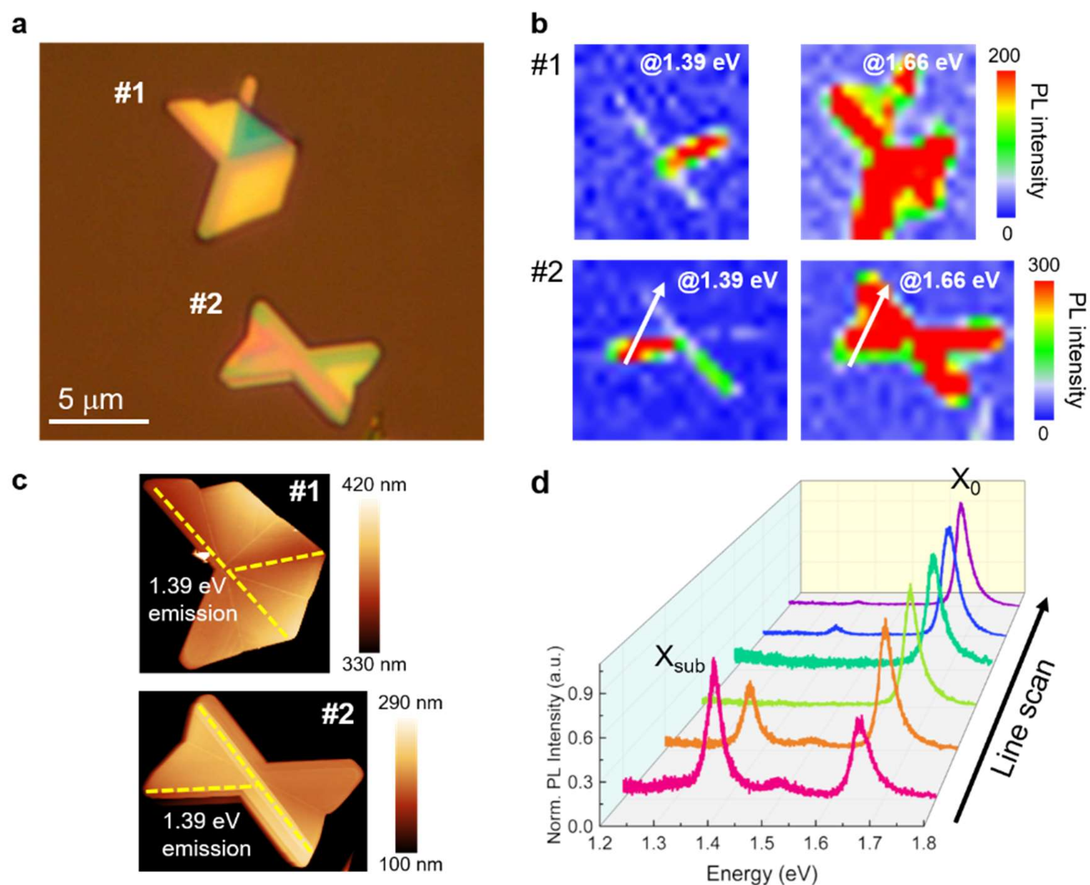

Figure 4.5 **(a)** Optical image of two typical GaTe flakes grown on sapphire. **(b)** PL intensity mapping at 1.39 eV and 1.66 eV for the two flakes. **(c)** AFM images of the two flakes. yellow

dashed lines show the position for the 1.39 eV emission. **(d)** Line scan of the PL spectra taken along the white arrow at flake #2 shown in (b).

To elucidate on the origin of these new PL peaks, we have performed large area spatial mapping of the PL spectra on two typical flakes grown on sapphire under 488 nm laser excitation with particular focus on the two most prominent PL peaks, namely 1.39 eV (X_{sub}) and 1.66 eV (X_0). However, similar conclusions can also be drawn for other below band gap emission peaks in Figure 4.4b**.** Overall, PL mapping data shows that emission peak position and intensity are relatively non-uniform across the flake as shown in Figure 4.5a-b. The X_0 emission is observed all across the flake for both flake #1 and #2, and is particularly strong at certain boundaries and edges. The X_{sub} emission line, however, is only observed at selected boundaries and edges, as shown in Figure 4.5b-c, suggesting spatially localized emission. A line scan of the PL spectra across flake #2 can be found in Figure 4.5d, which clearly demonstrates that the X_{sub} emission is only localized at the edges.

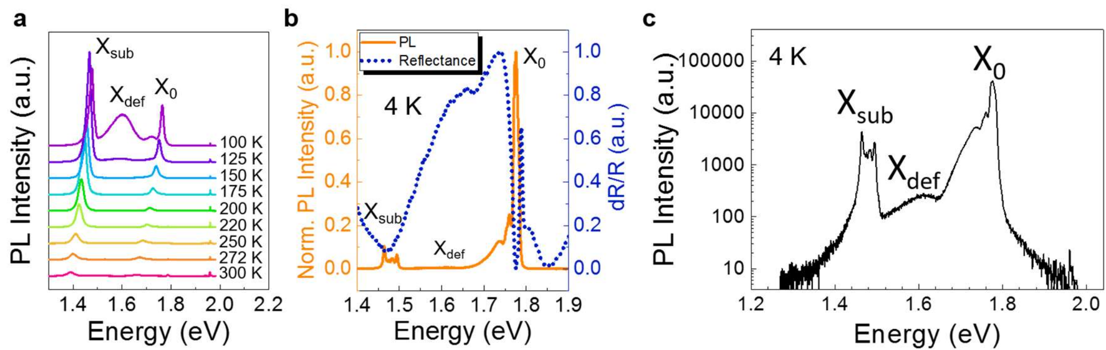

Figure 4.6 **(a)** Temperature dependent PL spectra measured at the spot with 1.39 eV emission. **(b)** PL and photo reflectance spectra measured at the spot with the intermediate band emission at 4 K. **(c)** log-scale plot of the PL spectrum in (b) to show the X_{def}.

Temperature dependent PL measurements (100-300K) in Figure 4.6a show that FWHM of X_0 and X_{sub} both remain fairly sharp at all temperatures (15 and 22 meV, respectively). Below 150 K an additional, broad (FWHM~123 meV) peak appears at 1.55 eV. This peak is also seen at 4K as shown in Figure S6. In contrast to X_{sub}, this broad peak, which thermally quenches above 100K, can be attributed to randomly arranged defects with shallow confinement, such as Ga vacancies that have been studied recently[96]. High signal-to-noise photoreflectance (PR) spectra at 4K (Figure 4.6b) show that the sharp differential reflectance (dR/R) peak (blue dashed line) matches closely in energy with the X_0 PL emission line (orange solid) i.e. we do not observe any Stokes shift due to localization of Coulomb bound electron-hole pairs (excitons) at this energy. This clearly demonstrates that the emission comes from radiative recombination of excitons at the direct bandgap around 1.78 eV[97, 98]. Here, we note that the blue shift of the X_0 emission from 1.66 eV at room temperature to 1.78 eV at low temperature is simply due to increase in optical band gap which can be described by the Varshni Law[99], the exciton binding energy of around 20 meV (bulk GaTe) is only a small correction[97, 98]. Similarly, X_{sub} peak position shifts from 1.39 eV at 300K to 1.5 eV at 4K, but the photoreflectance spectrum does not display any transition peak at 1.5 eV. The absence of reflectance transition proves that the X_{sub} has a comparably low density of states and oscillator strength and is not related to any strong band-to-band transition. We argue that X_{sub} originates from recombination of electron-hole pairs at localized energy levels at 1.39 eV (localized emission centers). This can be clearly seen in our power dependent PL studies: As shown in Figure 4.7a the X_{sub}/X_0 peak intensity ratio quickly decreases and the X_{sub} peak saturates as the laser power density is increased. This behavior is another indication

for a low density of states and suggests recombination of carriers spatially localized at defects to be the origin of X_{sub}.

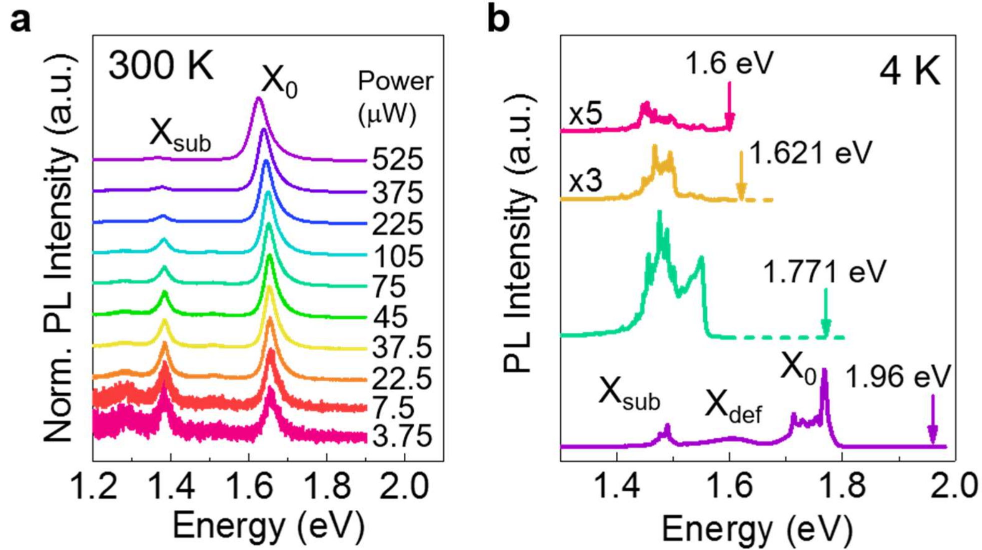

Figure 4.7 **(a)** Power dependent PL spectra measured at the spot with the intermediate band emission at room temperature. **(b)** PL spectra of the GaTe flakes excited by different laser energies at 4 K.

Using different laser excitation energies, we provide further evidence that shows that X_{sub} does not come from the band-to-band transition of a second phase but structural defects in GaTe. Figure 4.7b shows the PL spectra at excitation energies above the band gap (1.96 eV), resonant with the band gap (1.771 eV) and below the band gap (1.621 and 1.6 eV). Carriers excited resonantly at the band-gap can clearly relax very efficiently towards X_{sub}, which suggest that defects can capture a considerable fraction of the generated excitons. As expected from this scenario, we observe that laser excitation *below* the gap results in much lower defect related X_{sub} emission as the absorption (i.e. exciton generation) is strongly diminished.

The significance of this X_{sub} emission can be described as follows: (i) This emission is clearly seen at low temperature (4K) and room temperature, suggesting either strong confinement at defect sites or the formation of a mid-gap defect band. This looks similar to the intermediate band emission found in $ZnTe_{1-x}O_x$[100] and $CuIn_{1-x}Se_xS_2$[101] recently, which indicates the possibility of below bandgap absorption and intermediate band solar cells based on GaTe; (ii) The emission is spectrally very sharp with a FWHM similar to the band edge emission X_0, which is abnormal for a defect emission. Both observations (i) and (ii) are in clear contrast to X_{def}, which only appears at low temperature and is spectrally broad. Further studies have been planned on determining what kind of defects give rise to X_{sub} exactly. One possibility is O_2 adsorption as it has been established by DFT calculations that the GaTe-O_2 complex can induce intermediate band states in GaTe[95].

4.3 Anisotropy of VPT Synthesized GaTe

As discussed in Chapter 1, monoclinic GaTe has an anisotropic chain structure instead of isotropic hexagonal structure. Proved by the TEM study discussed above, The synthesized GaTe has a monoclinic phase, which is found to be more stable than the hexagonal phase[33]. Both phases have a layered structure with two Ga atoms sandwiched between two Te atoms in each layer. But it is clear that the two structures are quite different in the atom arrangements as shown in Figure 4.8a. In the hexagonal phase, each Ga atom is bonded to one Ga atom and three Te atoms and vice versa. All the Ga-Ga bonds are parallel to each other with an identical bonding length of 2.47 Å. However, in the monoclinic phase, every third of the Ga-Ga bonds is twisted and the bonding length is not the same for all Ga-Ga bonds. The Ga-Ga bonding length is 2.48 Å for those labeled

by the red rectangle in Figure 4.8a and 2.46 Å for the rest. As a result, a series of atomic chains is formed along the <010> direction. Similar to black phosphorous and ReS_2, the formation of these atomic chains is expected to give monoclinic GaTe unique in-plane anisotropy, which is proved by our angle resolved PL and Raman spectroscopy measurements.

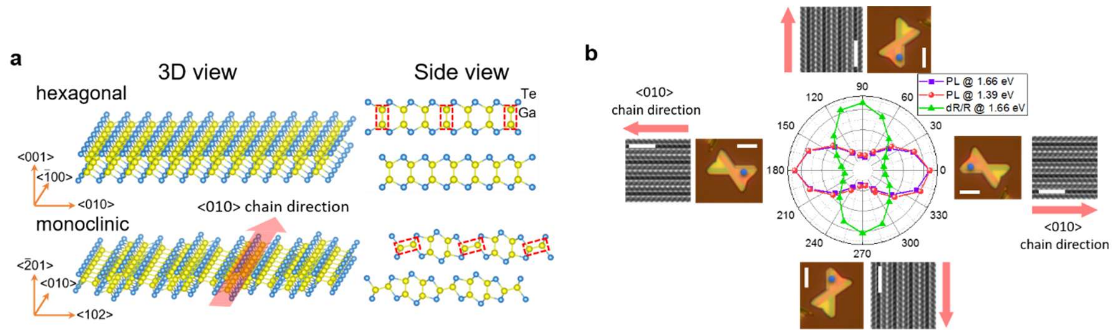

Figure 4.8 **(a)** Schematics of the crystal structure of hexagonal and monoclinic GaTe. **(b)** Angle resolved PL and reflectance intensity of the GaTe flake. The optical (scale bar = 5μm) and HRTEM images (scale bar = 2 nm) corresponding to 0o, 90o, 180o and 270o are shown around, with red arrows pointing toward the <010> chain direction. The blue spot shows the location where the PL and HRTEM are measured.

Figure 4.8b shows the angle resolved micro-PL (ARMP) and photo reflectance spectra of the GaTe flake. The atomic chains along the <010> direction are clearly seen in the i-FFT HRTEM image, which is parallel to the edge of the bow-tie shaped GaTe flake. The incident laser is polarized along the 0-180° direction and the sample is rotated counter-clockwise from 0° to 360°. It can be seen that the angle resolved PL intensity for both X_0 and X_{sub} emission show very similar angular dependence with a twofold symmetry. They reach their maximum intensities when the <010> chain direction is parallel to the laser polarization direction. The maximum PL intensity at 0° is about 5 times larger than at 90°, indicating strong anisotropy of the optical response of the GaTe

flake grown on sapphire. This is confirmed in reflectance measurements, which show a minimum along the <010> direction i.e. a maximum in absorbance (assuming negligible transmittance change as a function of rotation angle). This indicates that the maximum PL intensity along the <010> direction is also caused by maximum absorbance of the incident photons, as the emission mechanisms for X_0 and X_{sub} are different.

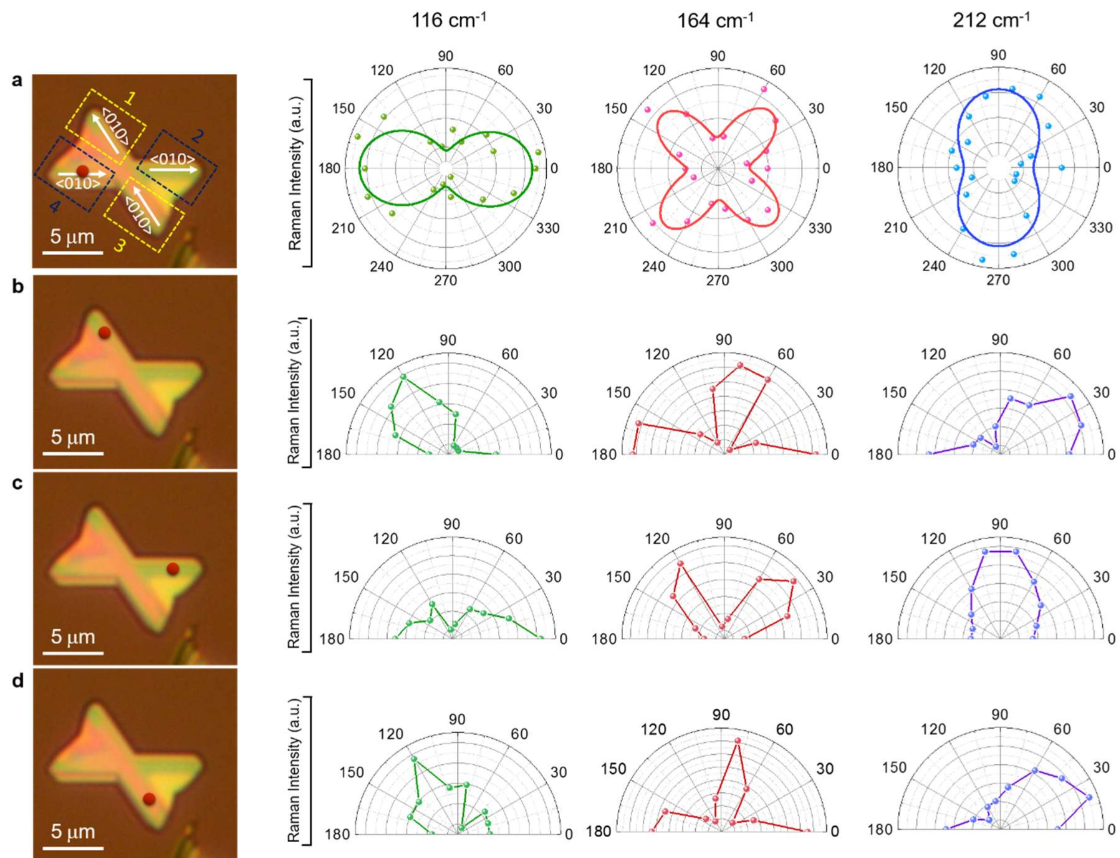

Figure 4.9 **(a-d)** Optical image and angle resolved Raman intensity of the 116 cm^{-1}, 164 cm^{-1} and 212 cm^{-1} peaks of the same GaTe flake, with a red spot showing the location where the angle resolved Raman spectroscopy is measured. The domain structure is indicated by the rectangles in (a). The solid lines in (a) are fitted curves.

The anisotropic behavior of the monoclinic GaTe flakes is also demonstrated by angle resolved micro-Raman (ARMR) spectroscopy, which has been widely used in other pseudo one dimensional materials such as ReS_2[22] and TiS_3[94]. The measurement is carried

out in the same setup as the ARMP experiment. Figure 4.9 shows the angle resolved Raman intensity of two A_g modes (116 and 212 cm^{-1}) and one B_g mode (164 cm^{-1}). The anisotropy of the two A_g mode both show a twofold symmetry with a period of 180°. The 116 cm^{-1} mode exhibits maximum intensities along the <010> chain direction, while the 212 cm^{-1} mode is polarized perpendicular to the chain direction. The opposite polarization behavior indicates different atomic displacement directions for the two modes. On the other hand, the polarization of the 164 cm^{-1} mode shows a fourfold symmetry with a 90° period, and the intensity reaches maximum at 45°, 135°, 225° and 315°, making a 45° degree with respect to the <010> chain direction. The different polarization features for the A_g and B_g modes are consistent with recent reports on GaTe anisotropy and can be explained by different symmetries of the A_g and B_g vibration modes[25]. As shown in Figure 4.9a, the GaTe flake is consisted of two domains with different crystal orientation and a grain boundary in between. The SAED pattern (Figure 4.4e) shows that each domain is single crystalline with the <010> chains parallel to the edge. Note that the flake in Figure 4.4d is half the shape of a bowtie shaped GaTe flake as shown in Figure 4.9a, which is probably due to the damage caused by the sonication when preparing the sample. As a result, the whole flake can be divided into 4 domains indicated by the rectangles in Figure 4.9a. To further understand the domain structure of the bowtie shaped GaTe flake, we have performed ARMR measurements in different domains on the bowtie shaped flake. The result shows that the 116 cm^{-1} mode is always polarized along the edge direction, which is the <010> chain direction and agrees with the SAED result. The polarization of the 164 cm^{-1} and 212 cm^{-1} modes are also consistent with the crystal orientation in each domain. Thus, domain 1 and 3 have the same

orientation, whereas domain 2 and 4 have the same orientation. The ARMR result further confirms that the crystal orientation is along the <010> chain direction at the edge of the bow-tie shaped GaTe flake which is consistent with recent work on exfoliated material[25].

4.4 Summary

This chapter demonstrates the synthesis of anisotropic pseudo-1D monoclinic GaTe on various substrates including GaAs (111), Si (111) and c-cut sapphire. GaTe flakes grown on sapphire exhibit well defined, narrow, and bright PL emission peaks originating from localized emission due to select type of imperfection sites states that appear at energies well below the fundamental emission line (optical bandgap). Bright emission within the forbidden band is observed for the first time in GaTe and may be the starting point for further defect engineering for optoelectronics in PTMCs. Lastly, angle resolved PL and Raman studies suggest that the synthesized monoclinic GaTe flakes are also highly anisotropic due to its unique crystal structure, which is the first demonstration of the anisotropy in vapor phase synthesized pseudo one-dimensional GaTe.

CHAPTER 5 SYNTHESIS AND PHASE CROSSOVER IN GaSeTe ALLOYS

This chapter studies the synthesis and unique phase crossover properties in layer structured $GaSe_{1-x}Te_x$ alloys. Layer structured $GaSe_{1-x}Te_x$ alloys is synthesized across the full composition range and an abnormal band bowing effect induced by hexagonal to monoclinic phase crossover is observed. While the GaSe-GaTe equilibrium phase diagram suggests that single phase $GaSe_{1-x}Te_x$ alloys do not exist across the full composition range due to the miscibility gaps, our results show that GaAs (111) substrate plays an essential role in stabilizing the metastable single-phase alloys within the miscibility gaps and enables full composition alloying. As the Te content increases, a hexagonal to monoclinic phase transition is observed. Such phase transition features isotropic to anisotropic transitions of the optical properties and crystal structures characterized by angle resolved Raman spectroscopy and HRTEM. We also found that in the phase crossover region ($0.56<x<0.67$) both phases can coexist, and two different bandgap values can be obtained at the same composition, leading to the anomalous band bowing effects.

5.1 Synthesis of $GaSe_{1-x}Te_x$ Alloys Across the Full Composition

Compared to the thorough studies carried out on pure GaSe and GaTe compounds, the alloy $GaSe_{1-x}Te_x$ remains highly unexplored. One reason for this is the difficulty of synthesizing these alloys. According to the phase diagram of the GaSe-GaTe system as shown in Figure 5.1, the solubility of the third element in the matrix is quite low (~10%) at room temperature[102], so there is no thermodynamically stable single-phase GaSeTe alloy across the full compositional range. Moreover, a hexagonal to monoclinic phase transition happens as the composition changes from GaSe to GaTe, making it more

difficult for stabilizing the single phased GaSeTe alloys. However, this does not mean that it is impossible to synthesize these alloys, because they can still exist as a metastable phase if correct condition and environment is provided.

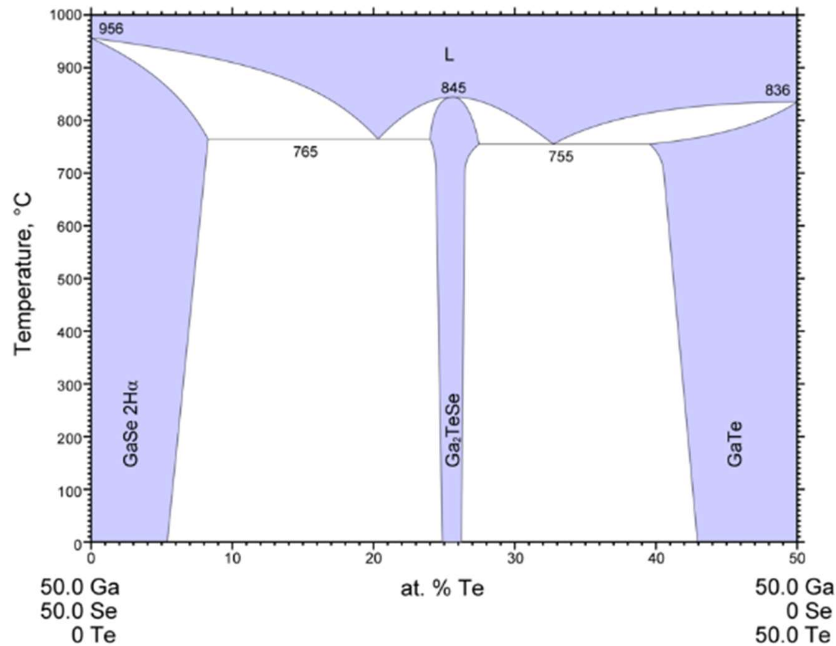

Figure 5.1 Phase diagram of the GaSe-GaTe system. (Figure taken from Ref. 102 © 2008 Pleiades Publishing, Ltd.)

In this work we overcome this difficulty by using the lattice matched GaAs (111) substrate and successfully synthesized $GaSe_{1-x}Te_x$ alloys in the full composition range. The $GaSe_{1-x}Te_x$ nanostructures were synthesized by VPT method in a single-zone tube furnace using GaSe and GaTe powders as the source materials (Figure 5.2). GaSe (60 mg) and GaTe (20 mg) powders (American Elements) were used as the source materials and Ar was used as the carrier gas. Bare GaAs (111) wafers were used as is for growth substrates. The GaSe and GaTe powders were loaded in two quartz boats and sent into the tube. The GaSe boat was put in the center of the tube and the GaTe boat was located upstream from GaSe. The distance between GaTe and GaSe was set in the range of 7-16

cm. The substrate was located 15 cm away downstream. The tube was evacuated to 10 mTorr and then heated from room temperature to 780 ^{o}C with a ramping rate of 20 $^{o}C/min$. The temperature was kept at 780 ^{o}C for 5 min and then cooled down to room temperature. The Ar flow rate was set at 50 sccm and the growth pressure was 300 Torr for the whole process.

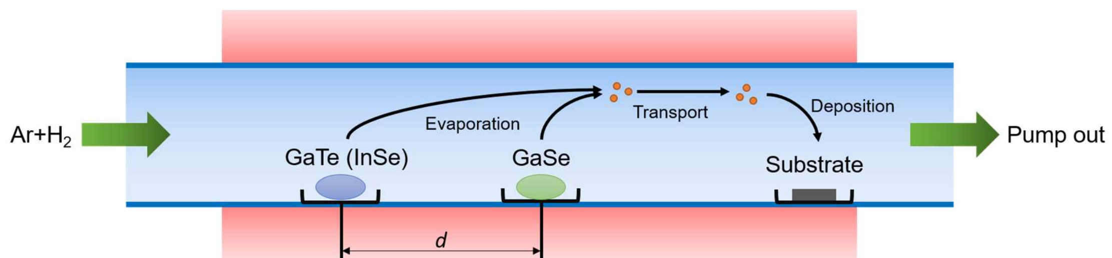

Figure 5.2 Schematic of the VPT growth process of GaSeTe and InGaSe alloys.

GaAs (111) is chosen as the substrate as it sustains layer-by-layer growth while facilitating epitaxial growth of both GaTe and GaSe owing to the close match in surface symmetry and the inter atomic distance. The composition of the $GaSe_{1-x}Te_x$ nanostructures is controlled by the evaporation rate of the GaTe and GaSe source. As shown in Figure 5.2, the GaTe and GaSe sources are separated by a distance *d* with GaSe kept in the center of the furnace and GaTe toward the upstream direction. The evaporation rate of the GaTe source is controlled by positioning it at various temperature regions with different distance *d* from the center. As *d* decreases, the temperature of the GaTe source increases, giving it a higher evaporation rate. At the same time, the GaSe source is fixed in the center so the evaporation rate is kept the same. To study the effect of *d* on the composition of the $GaSe_{1-x}Te_x$ nanostructures, we performed EDS measurement on each sample. As shown in Figure 5.3, both Se and Te peaks appear in every sample, indicating the formation of $GaSe_{1-x}Te_x$ alloys. The Te content in the GaSe1-

$_xTe_x$ nanostructure increases as *d* decreases, due to the increase of GaTe evaporation rate and partial pressure in the growth chamber.

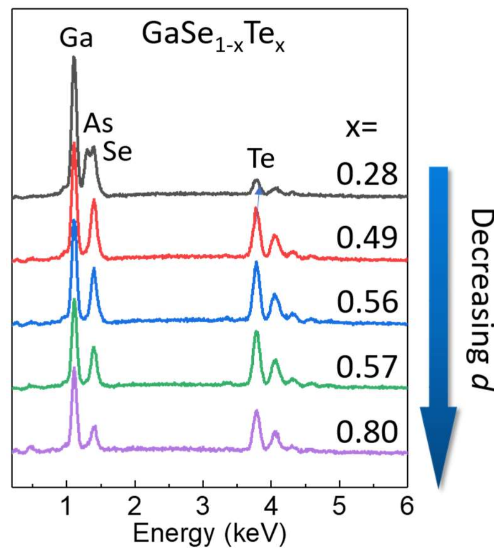

Figure 5.3 EDS spectra of the $GaSe_{1-x}Te_x$ nanostructures and the calculated composition

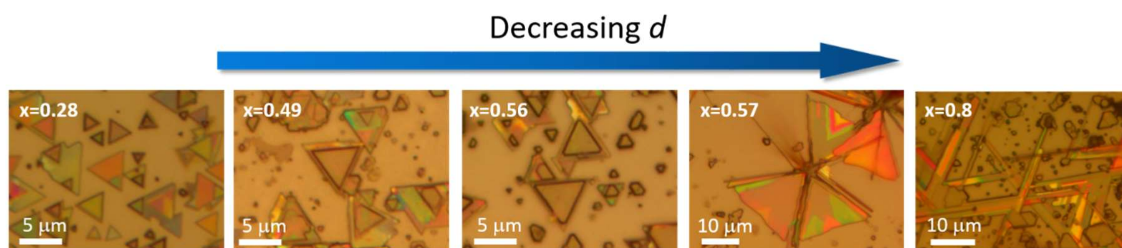

Figure 5.4 Optical images of the $GaSe_{1-x}Te_x$ nanostructures grown at different d between GaTe and GaSe source. Corresponding x values are shown on the top left corner of each image. Scale bar=5 μm for x=0.28, 0.49 and 0.56; 10 μm for x=0.57 and 0.8.

Interestingly, the morphology of the $GaSe_{1-x}Te_x$ nanostructure strongly depends on the Te content in $GaSe_{1-x}Te_x$. Closely following from Figure 5.4, on the Se-rich side where x<0.57, the growth typically yields 2D layered triangles with lateral dimension ranging from 1-10 μm. This finding agrees well with the prior work on GaSe demonstrating hexagonal phase and 3-fold symmetry[103, 104]. These triangles are grown in-plane and most of them are aligned along two directions with a 180° angle, indicating the

epitaxial growth of the $GaSe_{1-x}Te_x$ nanostructures on GaAs (111). At the Te-rich side with $x>0.57$, however, morphology changes to involve 1D structures ($0.57<x<0.8$) which become the dominant morphology when $x>0.8$. The nanoribbons are also grown in-plane and well aligned along three directions with an angle of 60° between each other when x is 0.8. This kind of one dimensional growth is quite similar to our previous study on GaTe[35], which has a highly anisotropic monoclinic structure that favors to grow along the [010] chain/anisotropy direction. The layered structure and growth direction of the nanoribbon is confirmed by high resolution TEM image and select area electron diffraction (SAED) and taken from a $GaSe_{1-x}Te_x$ nanoribbon with $x=0.63$ as shown in Figure 5.5. These optical images, geometrical anisotropy, and material morphology itself suggests that triangular and 1D-ribbon flakes belong to the three-fold symmetry isotropic hexagonal and anisotropic monoclinic phases, respectively, and crossover from 2D to 1D-like features occurs with increasing Te composition. More direct proofs for phase crossover and coexistence of two phases will be discussed within angle resolved Raman and PL spectroscopy as well as HRTEM measurements in the next sections. We note that bulk crystal growth, synthesis, and characterization of $GaSe_{1-x}Te_x$ alloys have been reported before. In these studies, results have shown that Se-rich ($x<0.25$) and Te-rich ($x>0.75$) phases can easily be crystallized but any composition between $0.25<x<0.75$ leads back to Se- and Te-rich phases. Our studies demonstrate the very first look at this previously unexplored composition region where extremely novel band bowing and multi-phase region exist.

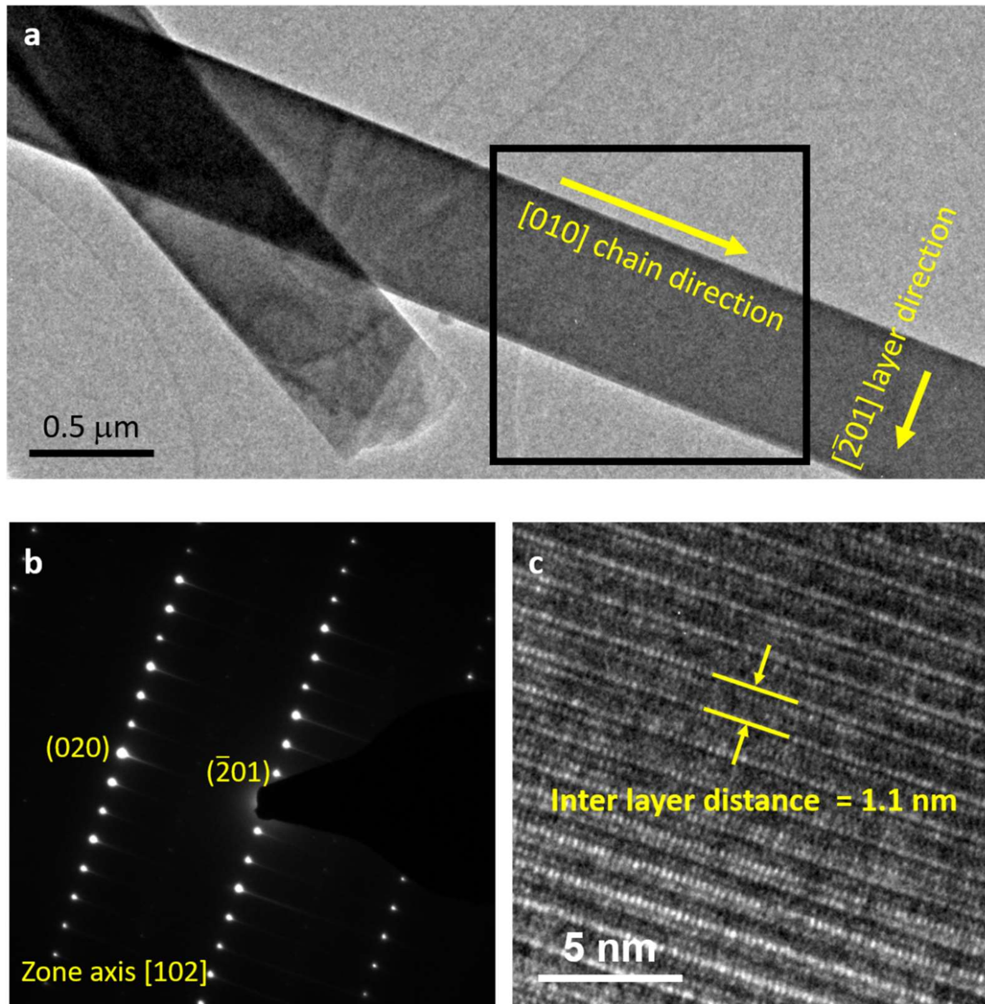

Figure 5.5 **(a)** Low magnification TEM image of a $GaSe_{1-x}Te_x$ nanowire with x=0.63. **(b)** SAED pattern of the nanowire taken from zone axis [102]. **(c)** HRTEM image of the nanowire with zone axis of [102].

5.2 Signature of Phase Transition in Raman Spectroscopy

To study the hexagonal to monoclinic phase transition in the $GaSe_{1-x}Te_x$ nanostructures, we performed detailed Raman and PL studies on these alloys across full composition. Fig. 5.5 shows the Raman spectra of $GaSe_{1-x}Te_x$ with x ranging from 0 to 1. The figure is separated into two parts – the upper part with yellow background comes from nanoribbons, while the lower part with blue background comes from triangular

shaped flakes. At x=0 (pure GaSe), the Raman spectrum contains three peaks at 136 cm^{-1} (A_{1g}^1 mode), 214 cm^{-1} (E_{2g} mode) and 308 cm^{-1} (A_{1g}^2 mode). The two peaks at 268 cm^{-1} and 294 cm^{-1} come from the GaAs substrate (Figure 5.6c). For x ranging from 0.28 to 0.66, the spectra share a similar shape with all three modes of GaSe presenting. A general tendency of softening is observed for all three vibration modes as Te content increases (Fig. 5.5b), corresponding to larger mass of Te atoms compared to Se. Note that the in-plane E_{2g} mode becomes rather broad and new peaks around it start to emerge as x becomes larger than 0.49. This is probably due to an increase in defect density that leads to the breakdown of the selection rule.

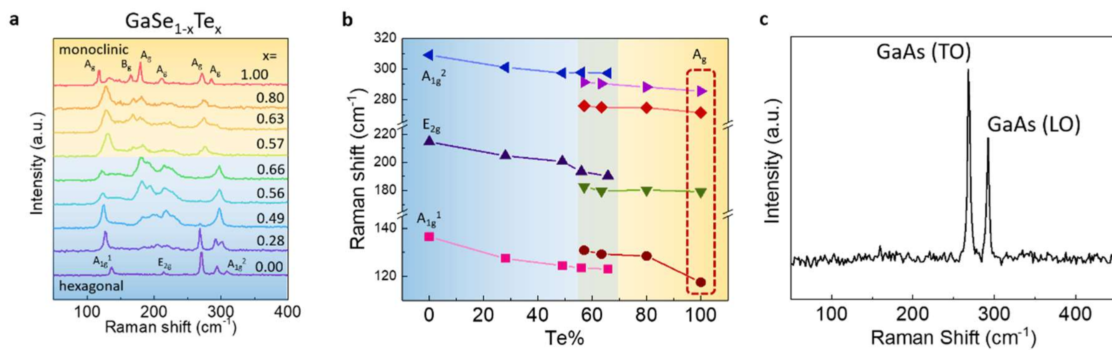

Figure 5.6 **(a)** Raman spectra of $GaSe_{1-x}Te_x$ nanostructures at different compositions. Monoclinic and hexagonal structures are separated by different background colors **(b)** Peak positions of different Raman modes as a function of Te content in $GaSe_{1-x}Te_x$. Blue background indicates the hexagonal side and yellow background indicates the monoclinic side. (c) Raman spectrum of the GaAs (111) substrate showing the transverse optical (TO) mode and the longitudinal optical (LO) mode.

As the morphology of the nanomaterial changes from 2D triangle to 1D nanoribbons, a dramatic change in the Raman spectra is observed (Figure 5.6a-b). The change is extremely clear when comparing the x=0.56 triangular sample with the x=0.57 nanoribbon. These two samples have very similar Te content but completely different

Raman spectra. First, the A_{1g}^1 mode shifts inversely to higher frequencies, and then softens as x increases. Second, the GaSe A_{1g}^2 mode disappears and a new peak at 276 cm^{-1} emerges, corresponding to the A_g mode at 280 cm^{-1} of pure GaTe. In the monoclinic region, the tendency of softening remains for all vibration modes as Te content increases, consistent with the trend in the hexagonal region. But the sudden change in the spectra characteristics around x=0.6 is a clear sign of hexagonal to monoclinic phase transition. Here, sudden Raman spectrum renormalization is associated with large changes in the crystal structure and symmetry resulting in largely different phonon vibration modes and Raman active modes. Indeed, similar Raman anomalies has been observed in high-pressure driven (diamond anvil cell measurements) phase transition of traditional material systems such as ReS_2 [105] and Teflon[106].

5.3 The Phase Crossover and Abnormal Band Bowing

A more exciting effect of the phase transition comes from the bandgap modulation. Photoluminescence spectra of $GaSe_{1-x}Te_x$ measured across the full composition range and the corresponding bandgap values are depicted in Figure 5.7, respectively. Here, we note that the GaAs substrate luminescence at 1.42 eV (Figure 5.7c) is fitted by $I = \sqrt{h\nu - E_g}\exp[-(h\nu - E_g)/k_B T]$, and the GaSeTe peak is fitted by Gaussian function for accurate determination of the E_{gap} values in Figure 5.7b. Similar to Raman spectra, an abrupt change in the bandgap is observed as the crystal structure changes from hexagonal to monoclinic. Interestingly, when the composition range is between $0.57<x<0.67$, two different PL peaks, E_{gap} values, and phases are *simultaneously* observed. We refer to this composition range ($0.57<x<0.67$) as the phase coexistence region. Previously, this kind

of phase coexistence behavior has not been observed in any other layered systems or 2D materials such as $Mo_xW_{(1-x)}S_2$, $MoS_{2x}Se_{2(1-x)}$, $ReS_{2x}Se_{2(1-x)}$, and others[107, 108, 109].

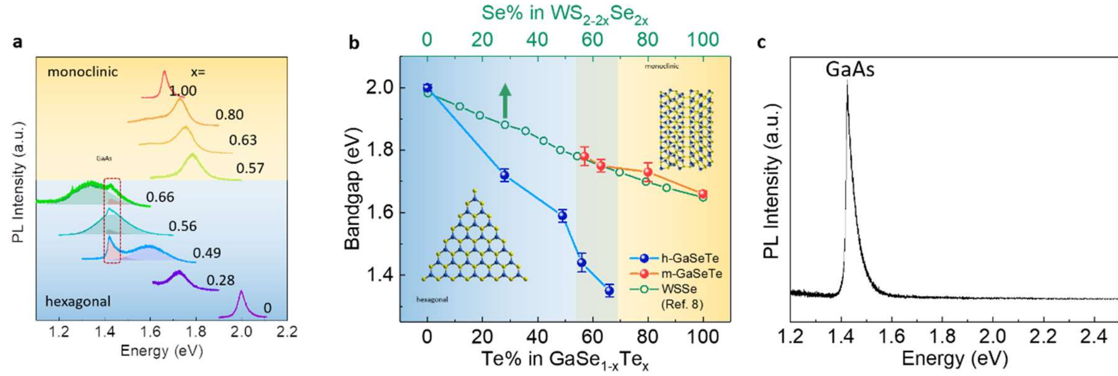

Figure 5.7 **(a)** PL spectra of $GaSe_{1-x}Te_x$ nanostructures at different compositions **(b)** Bandgap as a function of Te content in $GaSe_{1-x}Te_x$. (c) PL spectrum of the GaAs (111) substrate.

Potential explanation for this observation could be that two structural phases have rather close formation energies which enables one to attain two phases at a given composition. To offer better understanding to coexisting phases, we have performed density functional theory calculations within cluster expansion formalism to calculate formation energy differences between monoclinic and hexagonal phases at different tellurium content. Results (Figure 5.8) shows that initially x=0 (GaSe) and x=1 (GaTe) stabilizes in hexagonal and monoclinic phases respectively, consistent with our results. However, there exists a range of Te% values where two phases become energetically close to each other. For example, when x reaches ~40% two phases become energetically degenerate, and thus the two phases can coexist. While theoretically estimated composition range (Te~40%) for coexisting region is close to the experimentally observed values (~55-65%), the differences can be attributed to a variety of factors such as substrate effects, pressure differences (DFT under vacuum *vs*. experiment under

controlled pressure), and inability to account for kinetic / thermodynamic considerations with DFT framework.

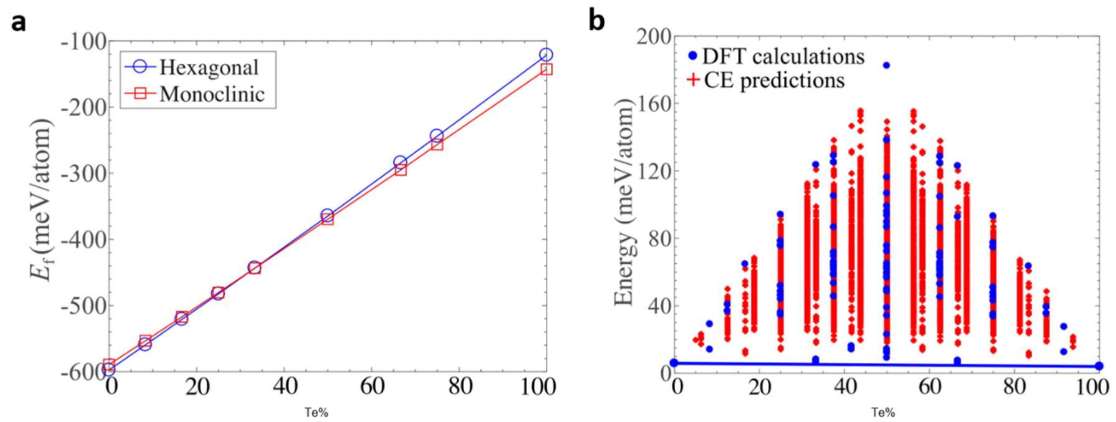

Figure 5.8 **(a)** Formation energies of both hexagonal and monoclinic phases of the GaSeTe alloy at various compositions. **(b)** Cluster expansion predictions and DFT calculations of the formation energies of GaSeTe alloys at different composition.

To elaborate the effect of substrates on the phase instability of the GaSeTe nanomaterials, we performed similar growth process on different substrates other than GaAs (111), including c-cut sapphire and highly oriented pyrolytic graphite (HOPG). The growth condition is the same as It can be seen that the phase of the GaSeTe nanomaterials strongly depends on the choice of the substrate. On HOPG, all flakes are grown in triangle shapes with hexagonal phase; while on sapphire, all flakes are grown in nanobelts with monoclinic phase as shown in Figure 5.9.

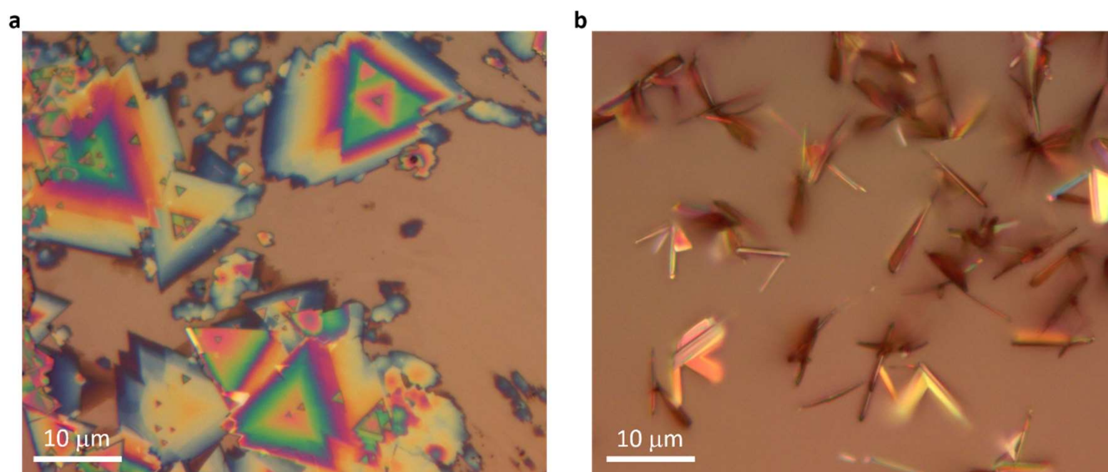

Figure 5.9 Optical images of GaSeTe nanomaterials grown on HOPG (**a**) and sapphire (**b**).

This dramatic difference can be explained by the different surface structure of the substrate and different interaction mechanism between the substrate and the GaSeTe nanomaterials. The surface of HOPG has a atomic flat hexagonal structure formed by carbon atoms arranging in honeycomb shape. As compared to the GaAs (111) surface, this structure is more isotropic and more similar to the surface of the hexagonal GaSeTe. This enables isotropic propagation of the GaSeTe adatoms on the HOPG surface and stabilization of the hexagonal structure of the GaSeTe nanomaterials[110]. On sapphire, most of the GaSeTe flakes are grown out of plane and belong to the monoclinic phase. This can be explained by the large lattice mismatch between sapphire and GaSeTe, which suppresses in-plane epitaxial growth. As there is no constraining force from the substrate, the Te-rich GaSeTe grows in its thermodynamically stable phase which is the monoclinic phase.

We note that the structural phase separation and coexistence observed in GaSeTe is different from the compositional phase separation commonly observed in most alloy systems where full composition alloy is not allowed. In those systems, the material

separates into two compositions where alloying is not allowed. This is also true for bulk GaSeTe alloys where compositions of $0.1<x<0.49$ and $0.51<x<0.85$ is inaccessible due to the compositional phase separation as shown in the phase diagram. However, our work shows that when GaSeTe is grown on GaAs (111) in 2D form, those forbidden compositions become accessible for GaSeTe alloys and completely new phenomena emerge - structural phase separation and coexistence at the same composition in a certain range.

It is also noteworthy to mention that the band bowing behavior in $GaSe_{1-x}Te_x$ (band gap variation with respect to alloying percentage) is significantly different from other 2D alloy systems owing to the presence of two different competing phases making large changes to the electronic band structure. For example, the $WS_{2-2x}Se_{2x}$ system has similar bandgaps as $GaSe_{1-x}Te_x$ at the two ends of x=0 and x=1[108]. The bandgap changes linearly in the $WS_{2-2x}Se_{2x}$ system because the system stays in one phase across full composition range, while it deviates from the linear relationship in the GaSeTe system due to the unique hexagonal to monoclinic phase transition. On the Se-rich hexagonal side as *x* goes from 0 $\rightarrow$0.66, the bandgap decreases from 2.01 eV to 1.35 eV, much faster compared to $WS_{2-2x}Se_{2x}$. As x changes from x=1 $\rightarrow$ 0.67 (the Te rich side), the band gap increases from 1.66 eV to 1.78 eV. In these two regions, the bandgap values for single-phase hexagonal ($0<x<0.57$) and monoclinic ($0.67<x<1$) shows a linear relationship with tellurium content, indicating a small band bowing parameter when the phase remains the same. However, in the phase crossover region, the band bowing theory, which relies on retaining the phase / crystal structure of semiconductor, can no longer be applied as evidenced by the dramatic bandgap change in phase coexistence region. This feature

enables wider bandgap tuning range in GaSeTe than $WS_{2-2x}Se_{2x}$. The two-phase coexisting region also allows us to make GaSeTe materials with different bandgaps without changing the composition. Using a linear extrapolation of the band gap variation across the composition range, we estimate that hexagonal GaTe and monoclinic GaSe (both materials have not been demonstrated before) should possess bandgap at 1.03 eV and 1.92 eV, respectively.

5.4 Isotropic to Anisotropic Phase Transition

Concurrent with abnormal band bowing across hexagonal to monoclinic phase transition, synthesized alloys possess unusual isotropic to anisotropic transition. While hexagonal GaSe possesses in-plane isotropy like 2D graphene and MoS_2, monoclinic GaTe is an anisotropic semiconductor in which atoms are arranged such a way that they form chains running along one particular lattice direction ([010] *b*-axis). To study the effect of phase transition on the structural properties of the $GaSe_{1-x}Te_x$ nanostructures, we have employed angle resolved Raman spectra at different Te content as shown in Figure 5.10. Previously, our team and others have successfully utilized angle resolved Raman spectroscopy to determine structural anisotropy direction of variety of 2D materials including monochalcogenides (GaTe)[25], dichalcogenides (ReS_2)[111], and trichalcogenides (MX_3 M=Hf, Zr, Ti; X=S, Se)[94, 112]. In this method, Raman intensity (I_R) of optical phonon modes involving atomic vibrations (induced polarization P_{ind}) along the chain (anisotropy) direction is measured as a function of P with angle (α). When the P direction is parallel (perpendicular) to atomic vibrations along (across) chain direction, P_{ind} and I_R is enhanced (reduced). Polar plots (I_R vs α), in return, enable one to determine if material

is anisotropic (two-lobed symmetry) and the anisotropy direction (lobe orientation direction).

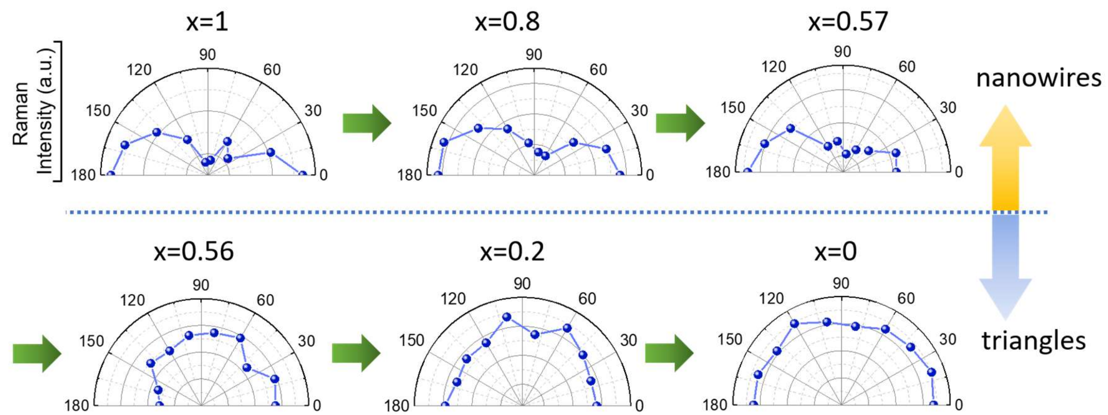

Figure 5.10 Evolution of angle resolved Raman peak intensity of the 128 cm^{-1} mode as Te content decreases.

In our measurements, we have selected optical mode located at 128 cm^{-1} that involves atomic vibrations along the chain direction for angle resolved Raman measurements. Previously, this peak has been successfully used to identify the chain direction of m-phase GaTe, and as expected displays a two-fold symmetry with a period of 180° (Figure 5.10 x=1)[35, 113]. Composition variation across x=1→0 (m-GaTe → h-GaSe) clearly shows that two-lobed feature turns into more isotropic polar plots in Figure 5.10. Here, we note that almost identical compositions (x=0.56 and 0.57) crystallize in hexagonal and monoclinic phases further proving co-existence of two phases.

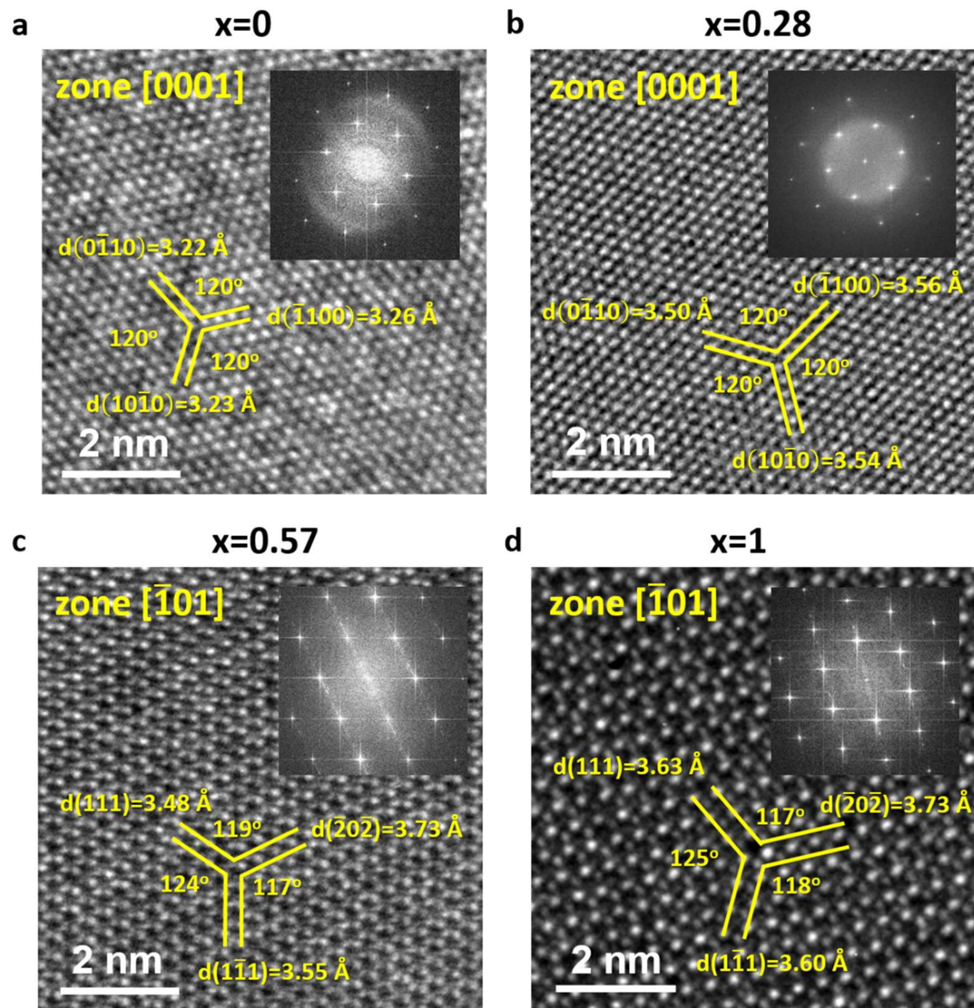

Figure 5.11 TEM and FFT patterns for $GaSe_{1-x}Te_x$ with **(a)** x=0 , **(b)** 0.28, **(c)** 0.57, and **(d)** x=1. The zone axis, interplanar distance and angle between planes are indicated in each image.

The crystal structure of both the hexagonal and monoclinic phases are studied by high resolution transmission electron microscope (HRTEM). Figure 5.11 shows the TEM images and corresponding fast Fourier transform (FFT) patterns for $GaSe_{1-x}Te_x$ with x=0, 0.28, 0.57 and 1. For the Se-rich x=0 and 0.28 samples, a six-fold symmetry is revealed with the angles between the $(10\bar{1}0)$, $(\bar{1}100)$ and $(0\bar{1}10)$ planes all being 120° as shown in Figure 5.11a and Figure 5.11b. The interplanar distance for the three planes closely match each other with very small difference between the maximum (d_{max}) and minimum (d_{min})

measured values (0.04 Å for x=0 and 0.06 Å for x=0.28). These features agree well with the characteristics of the hexagonal crystal system. Note that the interplanar distance increases as x increases from 0 to 0.28, because of the incorporation of the larger Te atoms compared to Se. For the Te-rich x=0.57 and x=1 samples, a completely different structure is found as shown in Figure 5.11c and Figure 5.11d. First, the 6-fold symmetry is lost and a 2-fold symmetry emerges, with the angles between the (111), $(\bar{2}0\bar{2})$ and $(1\bar{1}1)$ planes deviate from 120°. Second, the three planes possess different interplanar distance, with the d_{max}-d_{min} being 0.25 Å for x=0.57 and 0.33 Å for x=1. The interplanar distance of the GaTe sample (x=1) agrees well with the data of monoclinic GaTe from the ICDD database (PDF card No. 44-1127). These findings confirm the monoclinic structure of the x=0.57 and x=1 samples.

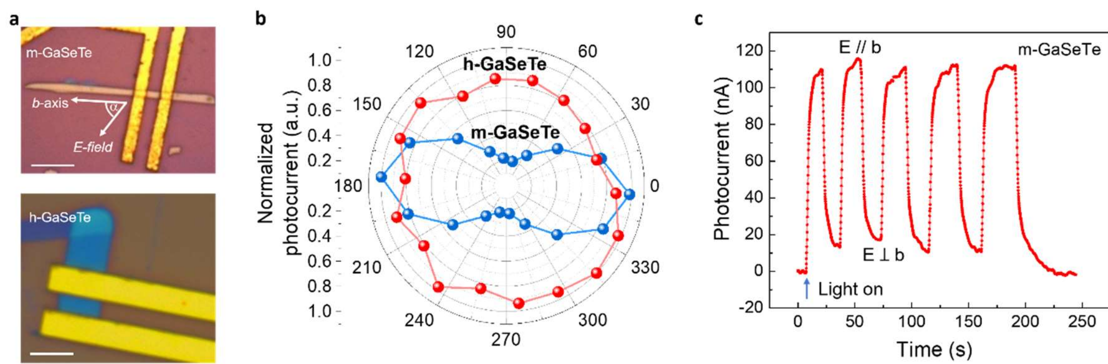

Figure 5.12 **(a)** Optical images of the GaSeTe devices based on the monoclinic (top, scale bar=10 μm) phase and hexagonal (bottom, scale bar=5 μm) phase. **(b)** Angle resolved photocurrent as a function of light polarization (E field) direction measured on both devices. **(c)** Time resolved photoresponse of the device based on monoclinic GaSeTe (V_{ds}=-0.2 V). The light polarization is alternatively switched between parallel and perpendicular to the b-axis.

To demonstrate the optoelectronic applications of the unique isotropic to anisotropic phase cross over in GaSeTe alloys, photodetectors based on both monoclinic and hexagonal GaSeTe alloys are fabricated, as shown in Figure 5.12a. The flake is cleaved

from GaSeTe samples grown onto GaAs substrates. Substrates are first indented by diamond tips of ~5um in diameter to delaminate samples lightly. Samples are mildly sonicated to release GaSeTe sheets that are transferred onto 285nm SiO_2/Si substrates using a mechanical transfer station. The 5 nm Ti/50 nm Au electrode was deposited onto the substrate by standard electron beam lithography. A 488 nm light source at 2.1mW/cm^2 power density is used for the photodetector characterization.

The phase of the two flakes are identified by Raman measurements based on the above discussion. Angle resolved photocurrent is measured as the polarization (E field) direction of the incident light is rotated with respect to the b-axis of the crystal. As shown in Figure 5.12b, the monoclinic GaSeTe has a clear dichroic response to photons. The photocurrent reaches maximum when the light polarization is parallel to the b-axis and becomes minimum when it is perpendicular to the b-axis. This is because the optical absorption coefficient is larger in the parallel setup than the perpendicular setup[35]. The direction dependent photoresponse is a clear demonstration of the anisotropy of the monoclinic GaSeTe. As a distinctive contrast, the hexagonal GaSeTe shows no direction dependent properties, owing to its isotropic hexagonal structure and loss of anisotropy. To further investigate the dichroic response of the monoclinic GaSeTe, we measured time resolved photocurrent change by alternatively switching the light polarization between parallel and perpendicular to the b-axis of the crystal. As shown in Figure 5.12c, the photocurrent rises rapidly as the polarization becomes parallel to the b-axis and drops immediately after turned to the perpendicular direction. The photo-responsivity (R) of the m-GaSeTe photodiode was calculated by the formula $R=I_{ph}/(P\cdot A_{eff})$. Here, $I_{ph}=|I_{on}-I_{off}|$, P is the incident light power per unit area (488 nm light source at 2.1mW/cm^2), A_{eff} is the

effective illumination area (~5 μm^2). By calculation, the highest R is ~950 A/W at V_{ds}=-0.2V when polarization is parallel to the b-axis. In comparison, R drops by 5 times down to ~200 A/W at P⊥b-axis, consistent with our polar photocurrent results.

5.5 Coexistence of the Hexagonal and Monoclinic Phase in the Crossover Region

We provide further proof that these vastly different phases coexist simultaneously within the same flake in phase separated form. This is in contrast to any other datasets in Figure 5.6 where different phases were observed at same compositions but on different flakes.

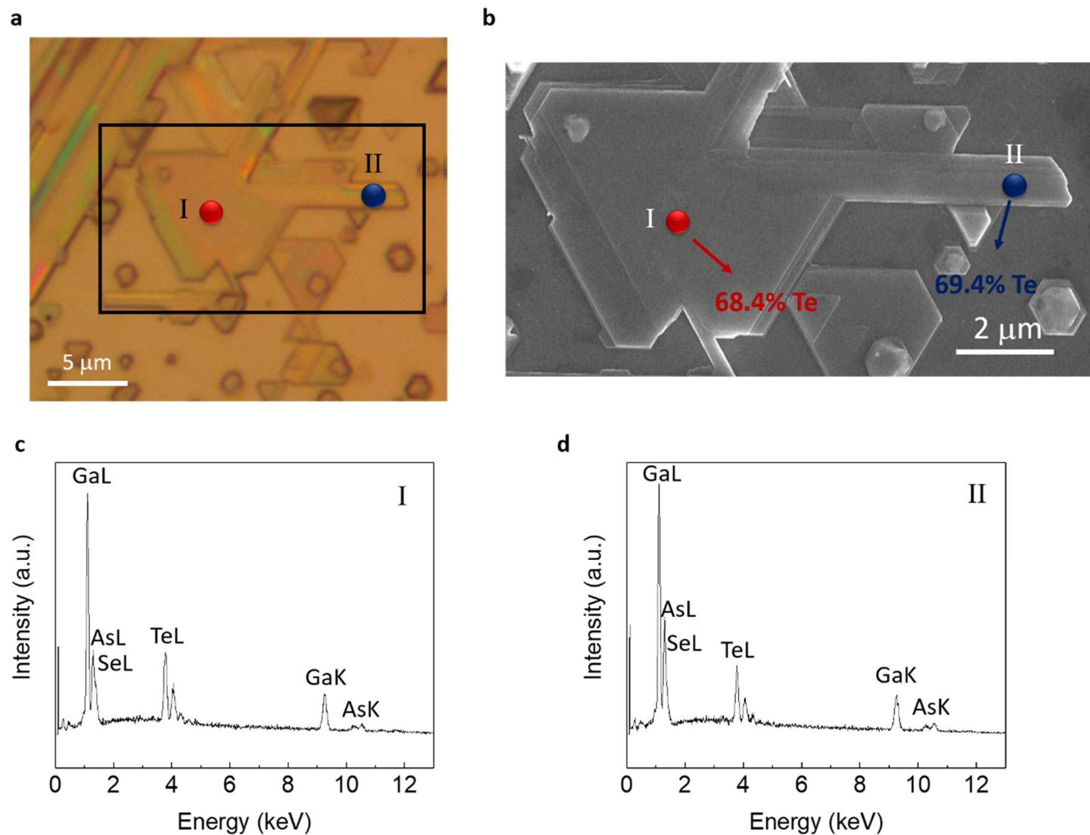

Figure 5.13 **(a)** Optical image of a $GaSe_{1-x}Te_x$ flake with both hexagonal (region-I) and monoclinic (region-II) phase grown simultaneously. **(b)** SEM image of the flake with coexisting hexagonal and monoclinic phase. The composition measured by EDS for each region is indicated by Te% in the figure. **(c-d)** EDS spectra taken from region I and II indicated in **(a)** and **(b)**.

A closer look at Figure 5.13a demonstrates the presence of triangular and nanoribbon features: Despite the dramatic difference in the morphology, both regions have close Te content – 68.4% for triangles and 69.4% for the nanoribbons (Figure 5.13b). The EDS spectra of the two regions can be found in Figure 5.13c-d. Raman spectrum and angle resolved Raman datasets in Figure 5.14 clearly demonstrate phase separated hexagonal (region I red) and monoclinic (region II blue) phases. These two phases are clearly distinguished by PL spectra as shown in Figure 5.15. The hexagonal region-I has a PL peak at 1.34 eV, while the monoclinic region-II shows a peak at 1.74 eV. Both PL emission energies fit into the linear bandgap relation vs Te content as discussed in Figure 5.7b. Note that 1% minuscule composition difference across these two regions leads to colossal bandgap renormalization of 0.4 eV. Coexisting phases on the same flake is best observed from PL mapping of the 1.74 eV peak intensity in Figure 5.15b.

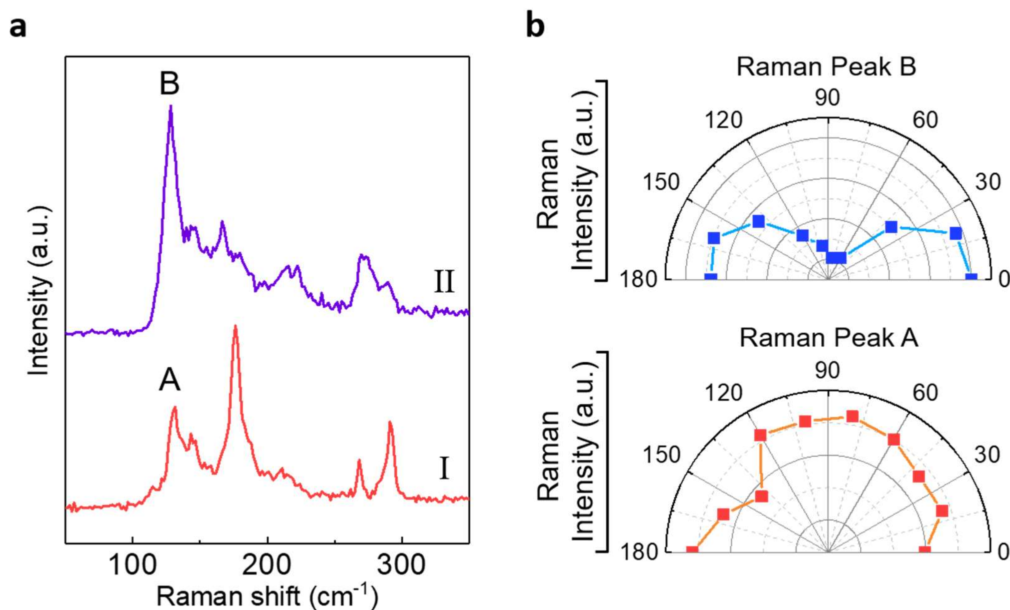

Figure 5.14 **(a)** Raman spectra taken at region-I and region-II from Figure 5.13a. **(b)** Angle resolved Raman peak intensity of peak A and B from region-I and II.

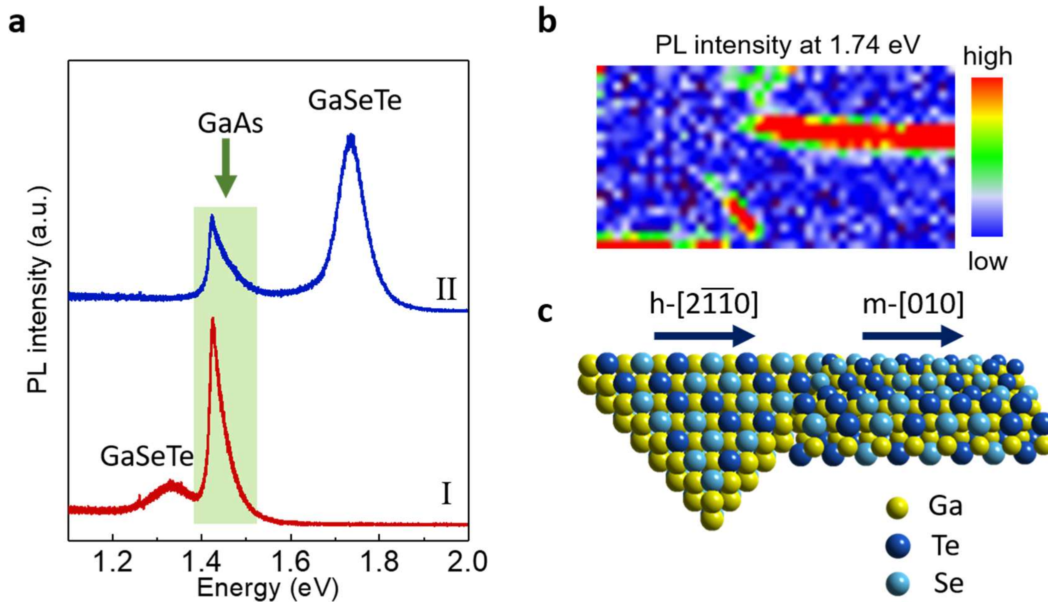

Figure 5.15 **(a)** PL spectra taken at region-I and II. GaAs substrate peak is labeled by green backgound. **(b)** PL mapping of the emission intensity at 1.74 eV taken from the area indicated by the rectangular in Figure 5.13a. **(c)** Schematic of the 3D atomic structure of the coexisting hexagonal and monoclinic phases.

PL mapping of 1.74eV peak shows that PL intensity is maximized around needle like nanoribbons (Figure 5.15b). Based on this we have constructed 3D view of the coexisting phase interfaces / boundaries in Figure 5.15c. It is noteworthy to point out that the PL intensity increases suddenly as it goes from region-I to region-II, indicating the interface between the two phases is sharp without any gradual transition area. We believe the growth procedure for this mixed-phase flake is as follows: the triangle region nucleates and grows on the GaAs (111) surface epitaxially first, followed by the growth of the nanobelts extending outward. The size of the hexagonal phase is limited due to the strain induced by the lattice mismatch between $GaSe_{1-x}Te_x$ and the GaAs substrate. As the hexagonal phase grows larger, it becomes less stable and the LBL growth turns into

dendritic growth, transforming the hexagonal phase to monoclinic phase characterized by the nanobelt shape in region-II.

5.6 Summary

This chapter demonstrates the novel phase crossover and anomalous band bowing effects in $GaSe_{1-x}Te_x$ nanostructures when the composition is continuously varied across two completely different materials, namely isotropic hexagonal GaSe (x=0) and anisotropic monoclinic GaTe (x=1). While traditional GaSe-GaTe phase diagram alone suggests that single phase $GaSe_{1-x}Te_x$ alloying across the full composition is not possible, results herein show that GaAs (111) substrate plays an essential role in stabilizing the metastable phases and enable wide composition variation to access previously unavailable phase crossover region. The coexistence of the isotropic hexagonal phase and the anisotropic monoclinic phase opens opportunities to make GaSeTe nanomaterials with different response to polarized light without changing the composition. Our results deepen our understanding for the gallium chalcogenide family and provide guidelines for tuning material properties through phase engineering.

CHAPTER 6 CONCLUSIONS AND OUTLOOK

5.1 Conclusions

In this dissertation, I demonstrated the synthesis of layer structured GaSe, GaTe and GaSeTe alloys with highly controlled structure, morphology and properties using vapor phase transport. In this synthesis process, the substrate is found to play an essential role in determining the structure and properties of the final product. In the growth of GaSe, the non-uniform lateral tensile strain induced by the substrate reduces the bandgap down to 1.7 eV and causes the continuous bandgap variation on a single GaSe flake. In the growth of GaTe, the nanowires are found to grow epitaxially along aligned directions on GaAs(111) and Si(111) surfaces, but randomly oriented on sapphire due to no direct bonding with the substrate. In the growth of GaSeTe alloys, the GaAs(111) substrate facilitates the formation of single phased alloys across the full composition despite the miscibility gaps in the phase diagram due to the close lattice and symmetry match. Furthermore, HOPG and sapphire yield completely different phases and morphologies of the product due to the different van der Waals interaction strength between GaSeTe and the substrate. These results indicate that the choice of substrate is a critical factor in engineering the structure and properties of layer structured gallium chalcogenides.

Besides the effect of substrates, defects are found to be another important factor in manipulating the optical properties of layer structured gallium chalcogenides. In the work of GaTe presented in Chapter 4, multiple PL emissions related to defects are observed below the bandgap. Due to their origins from different kinds of defects, they exhibit different behaviors as a function of temperature and laser power. The peak related to bound excitons at localized point defects shows a weak and broad emission, but the one

related to edge states and grain boundaries shows a strong and sharp peak. The result presented here emphasizes the important effect of various types of defects in manipulating the exitonic features in layer structured gallium chalcogenides.

The different crystal structures between GaSe and GaTe inspired the idea of phase engineering in GaSeTe alloys as presented in Chapter 5. As the Te content is increased, a hexagonal to monoclinic phase transition and crossover is observed. In the phase crossover region, both phases coexist at the same composition but demonstrate completely different crystal structures, bandgaps and anisotropic behavior. This unique phase crossover results in an abnormal band bowing phenomenon in the GaSeTe alloys, leading to a much wider bandgap tuning range than single phased alloys. Results suggest that the properties of layer structure gallium chalcogenides can be engineered through the phase engineering approach.

5.2 Outlook

In the past decade, significant progress has been made in both fundamental science and applications of 2D materials. The bulk of this effort has focused on graphene and transition metal dichalcogenides, where controlled synthesis and engineering of their physical properties have been thoroughly studied. Gallium chalcogenides as an important component in the 2D materials family, however, has not been given enough attention and remain highly unexplored. The main reason is that unlike TMDCs, gallium chalcogenides are indirect bandgap semiconductors in the monolayer form and cannot emit light. However, this dissertation demonstrates that these materials exhibit intriguing properties that could lead to exciting opportunities and applications even in the few layered or bulk form. For example, the non-uniform strain on GaSe grown on Si(111) could form

nanoscale localized strain field that traps excitons through the band funneling effect. These spatially localized excitons resemble those in quantum dots where quantum confinement effect applies and may exhibit unique quantum phenomena such as single photon emission.

Gallium telluride distinguishes itself from GaS and GaSe by its monoclinic structure characterized by the well-defined quasi-1D atomic chains that extend along a particular lattice direction. Such unique anisotropic crystal structure makes GaTe fall into the "2D anisotropic" materials family that includes black phosphorous, ReS_2, TaS_3 etc. Table 6.1 lists the mostly studied 2D anisotropic materials. These materials host exciting and highly technologically relevant material properties, such as high carrier mobility[112, 114], polarized light emission/absorption[115, 116, 117], thermally conductive pathways[118], and novel quantum phenomena that lead to degrees of variation in properties along different crystallographic orientations. However, most of these exciting properties remain unexplored in GaTe, opening up opportunities for future research such as epitaxial growth with controlled atomic chain orientation, direction dependent electronic and thermal transport, effect of defects on the anisotropic properties etc.

Table 6.1 List of commonly found 2D anisotropic materials

Material class	Examples	Properties
Monoatomic	BPs, 2D Te, and 2D Se	High carrier mobility, polarized excitons
Monochalcogenides	**GaTe**, SnSe, and GeSe	High ZT, polarized excitons
Dichalcogenides	ReS_2, $ReSe_2$, $MoTe_2$, WTe_2	Charge density wave (CDW), Quantum spin hall, polarized excitons
Trichalcogenides	MX_3 (M=Hf, Zr, Ti, Nb, Ta and X= S, Se, Te)	High carrier mobility, polarized excitons, CDW
Others	SiP, $NbTe_4$, $TaTe_4$, Nb_3S_4, $ZrTe_5$, NbI_4	High carrier mobility

The discovery of hexagonal to monoclinic phase transition and crossover in the GaSeTe alloy system is an exclusive finding in the 2D materials family so far. However, such phenomenon has the potential to exist in many other 2D alloys with the two components being different phases. For example, in the SnSe-SnTe system, SnSe has an orthorhombic structure with the space group of Pnma, while SnTe has a FCC phase belonging to the Fm-3m space group. Furthermore, SnSe is a narrow bandgap semiconductor with a bandgap of 0.52 eV, while SnTe is nearly metallic with a bandgap of 0.04 eV. Figure 6.1 shows the phase diagram of the SnSe-SnTe system[119], where a miscibility gap is found in the middle. However, using the knowledge learned from GaSeTe, this gap could be closed if appropriate synthesis method and substrates are used. Once the miscibility gap is closed and full composition alloys of SnSeTe are formed, orthorhombic to FCC phase transition and crossover could be observed at a certain composition. Such transition is a layered to non-layered structural transition and could also be semiconductor to metal transition. SnSeTe is not the only promising system that

could host such phase crossover, which may also be observed in GeSeTe and SnGeTe 2D alloys.

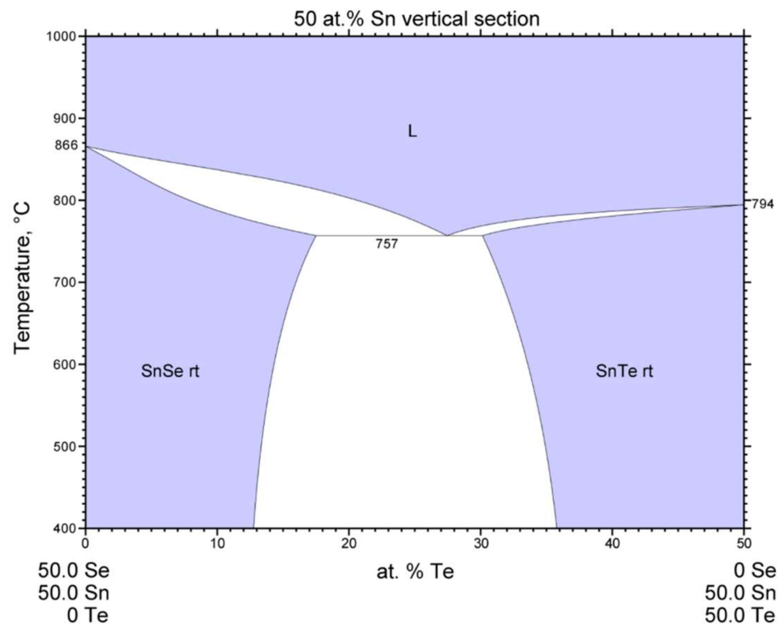

Figure 6.1 Phase diagram of the SnSe-SnTe system. (Figure taken from Ref. 119 © 1992 Elsevier B.V.)

Overall, the work presented in this dissertation opens up opportunities for discovering new properties and potential high-performance device applications for layer structured gallium chalcogenides and other 2D systems through controlled vapor phase synthesis, strain engineering, defect engineering and phase engineering.

REFERENCES

1. Novoselov, K. S.; Geim, A. K.; Morozov, S. V.; Jiang, D.; Zhang, Y.; Dubonos, S. V.; Grigorieva, I. V.; Firsov, A. A. "Electric Field Effect in Atomically Thin Carbon Films". *Science* 306(2004): 666-669.

2. Dean, C. R.; Young, A. F.; MericI; LeeC; WangL; SorgenfreiS; WatanabeK; TaniguchiT; KimP; Shepard, K. L.; HoneJ. "Boron nitride substrates for high-quality graphene electronics". *Nature Nanotechnology* 5(2010): 722-726.

3. Wang, Qing; Kalantar-Zadeh, Kourosh; Kis, Andras; Coleman, Jonathan N.; Strano, Michael S. "Electronics and optoelectronics of two-dimensional transition metal dichalcogenides". *Nature Nanotechnology* 7(2012): 699-712.

4. Mao, Nannan; Wu, Juanxia; Han, Bowen; Lin, Jingjing; Tong, Lianming; Zhang, Jin. "Birefringence-Directed Raman Selection Rules in 2D Black Phosphorus Crystals". *Small* 12(2016): 2627-2633.

5. Lu, Junpeng; Yang, Jiong; Carvalho, Alexandra; Liu, Hongwei; Lu, Yuerui; Sow, Chorng H. "Light-Matter Interactions in Phosphorene". *Accounts of chemical research* 49(2016): 1806-1815.

6. Li, Likai; Kim, Jonghwan; Jin, Chenhao; Ye, Guo J.; Qiu, Diana Y.; da Jornada, Felipe H.; Shi, Zhiwen; Chen, Long; Zhang, Zuocheng; Yang, Fangyuan; Watanabe, Kenji; Taniguchi, Takashi; Ren, Wencai; Louie, Steven G.; Chen, Xian H.; Zhang, Yuanbo; Wang, Feng. "Direct observation of the layer-dependent electronic structure in phosphorene". *Nature Nanotechnology* (2016): 21-25.

7. Li, Xufan; Lin, Ming-Wei; Puretzky, Alexander A.; Idrobo, Juan C.; Ma, Cheng; Chi, Miaofang; Yoon, Mina; Rouleau, Christopher M.; Kravchenko, Ivan I.; Geohegan, David B.; Xiao, Kai. "Controlled Vapor Phase Growth of Single Crystalline, Two-Dimensional GaSe Crystals with High Photoresponse". *Scientific Reports* 4(2014): 5497.

8. Lei, Sidong; Ge, Liehui; Najmaei, Sina; George, Antony; Kappera, Rajesh; Lou, Jun; Chhowalla, Manish; Yamaguchi, Hisato; Gupta, Gautam; Vajtai, Robert; Mohite, Aditya D.; Ajayan, Pulickel M. "Evolution of the Electronic Band Structure and Efficient Photo-Detection in Atomic Layers of InSe". *ACS Nano* 8(2014): 1263-1272.

9. Late, Dattatray J.; Liu, Bin; Luo, Jiajun; Yan, Aiming; Matte, H. S. S.; Grayson, Matthew; Rao, C. N.; Dravid, Vinayak P. "GaS and GaSe ultrathin layer transistors". *Advanced Materials* 24(2012): 3549-3554.

10. Hu, PingAn; Wen, Zhenzhong; Wang, Lifeng; Tan, Pingheng; Xiao, Kai. "Synthesis of Few-Layer GaSe Nanosheets for High Performance Photodetectors". *ACS Nano* 6(2012): 5988-5994.

11. Novoselov, K. S.; Geim, A. K.; Morozov, S. V.; Jiang, D.; Katsnelson, M. I.; Grigorieva, I. V.; Dubonos, S. V.; Firsov, A. A. "Two-dimensional gas of massless Dirac fermions in graphene". *Nature* 438(2005): 197-200.

12. Balandin, Alexander A.; Ghosh, Suchismita; Bao, Wenzhong; Calizo, Irene; Teweldebrhan, Desalegne; Miao, Feng; Lau, Chun. "Superior Thermal Conductivity of Single-Layer Graphene". *Nano letters* 8(2008): 902-907.

13. Lee, Changgu; Wei, Xiaoding; Kysar, Jeffrey W.; Hone, James. "Measurement of the Elastic Properties and Intrinsic Strength of Monolayer Graphene". *Science* 321(2008): 385-388.

14. Splendiani, A.; Sun, L.; Zhang, Y. B.; Li, T. S.; Kim, J.; Chim, C. Y.; Galli, G.; Wang, F. "Emerging Photoluminescence in Monolayer MoS_2". *Nano letters* 10(2010): 1271-1275.

15. Mak, K. F.; Lee, C.; Hone, J.; Shan, J.; Heinz, T. F. "Atomically Thin MoS_2: A New Direct-Gap Semiconductor". *Physical Review Letters* 105(2010): 136805.

16. Qiu, Diana Y.; da Jornada, Felipe H.; Louie, Steven G. "Optical Spectrum of MoS_2: Many-Body Effects and Diversity of Exciton States". *Physical Review Letters* 111(2013): 216805.

17. Tran, V.; Soklaski, R.; Liang, Y. F.; Yang, L. "Layer-controlled band gap and anisotropic excitons in few-layer black phosphorus". *Physical Review B* 89(2014): 235319.

18. Brown, A.; Rundqvist, S. "Refinement of Crystal Structure of Black Phosphorous". *Acta Crystallographica* 19(1965): 684.

19. Liu, E. F.; Fu, Y. J.; Wang, Y. J.; Feng, Y. Q.; Liu, H. M.; Wan, X. G.; Zhou, W.; Wang, B. G.; Shao, L. B.; Ho, C. H.; Huang, Y. S.; Cao, Z. Y.; Wang, L. G.; Li, A. D.; Zeng, J. W.; Song, F. Q.; Wang, X. R.; Shi, Y.; Yuan, H. T.; Hwang, H. Y.; Cui, Y.; Miao, F.; Xing, D. Y. "Integrated digital inverters based on two-dimensional anisotropic ReS_2 field-effect transistors". *Nature Communications* 6(2015): 6991.

20. Tongay, S.; Sahin, H.; Ko, C.; Luce, A.; Fan, W.; Liu, K.; Zhou, J.; Huang, Y. S.; Ho, C. H.; Yan, J. Y.; Ogletree, D. F.; Aloni, S.; Ji, J.; Li, S. S.; Li, J. B.; Peeters, F. M.; Wu, J. Q. "Monolayer behaviour in bulk ReS_2 due to electronic and vibrational decoupling". *Nature Communications* 5(2014): 3252.

21. Chenet, Daniel A.; Aslan, Burak O.; Huang, Pinshane Y.; Fan, Chris; van der Zande, Arend M.; Heinz, Tony F.; Hone, James C. "In-Plane Anisotropy in Mono- and Few-Layer ReS_2 Probed by Raman Spectroscopy and Scanning Transmission Electron Microscopy". *Nano letters* 15(2015): 5667-5672.

22. Wu, K. D.; Chen, B.; Yang, S. J.; Wang, G.; Kong, W.; Cai, H.; Aoki, T.; Soignard, E.; Marie, X.; Yano, A.; Suslu, A.; Urbaszek, B.; Tongay, S. "Domain Architectures and Grain Boundaries in Chemical Vapor Deposited Highly Anisotropic ReS_2 Monolayer Films". *Nano letters* 16(2016): 5888-5894.

23. Aydinli, A.; Gasanly, N. M.; Uka, A.; Efeoglu, H. "Anharmonicity in GaTe layered crystals". *Crystal Research and Technology* 37(2002): 1303-1309.

24. Sánchez‐Royo, J. F.; Segura, A.; Muñoz, V. "Anisotropy of the refractive index and absorption coefficient in the layer plane of gallium telluride single crystals". *physica status solidi (a)* 151(1995): 257-265.

25. Huang, Shengxi; Tatsumi, Yuki; Ling, Xi; Guo, Huaihong; Wang, Ziqiang; Watson, Garrett; Puretzky, Alexander A.; Geohegan, David B.; Kong, Jing; Li, Ju; Yang, Teng; Saito, Riichiro; Dresselhaus, Mildred S. "In-Plane Optical Anisotropy of Layered Gallium Telluride". *ACS Nano* 10(2016): 8964–8972.

26. Ling, X.; Huang, S. X.; Hasdeo, E. H.; Liang, L. B.; Parkin, W. M.; Tatsumi, Y.; Nugraha, A. R. T.; Puretzky, A. A.; Das, P. M.; Sumpter, B. G.; Geohegan, D. B.; Kong, J.; Saito, R.; Drndic, M.; Meunier, V.; Dresselhaus, M. S. "Anisotropic Electron-Photon and Electron-Phonon Interactions in Black Phosphorus". *Nano letters* 16(2016): 2260-2267.

27. Corbett, C. M.; McClellan, C.; Rai, A.; Sonde, S. S.; Tutuc, E.; Banerjee, S. K. "Field Effect Transistors with Current Saturation and Voltage Gain in Ultrathin ReS_2". *ACS Nano* 9(2015): 363-370.

28. Yu, S.; Zhu, H.; Eshun, K.; Shi, C.; Zeng, M.; Li, Q. L. "Strain-engineering the anisotropic electrical conductance in ReS_2 monolayer". *Applied Physics Letters* 108(2016): 191901.

29. Xu, K.; Deng, H. X.; Wang, Z. X.; Huang, Y.; Wang, F.; Li, S. S.; Luo, J. W.; He, J. "Sulfur vacancy activated field effect transistors based on ReS_2 nanosheets". *Nanoscale* 7(2015): 15757-15762.

30. Huang, Wenjuan; Gan, Lin; Li, Huiqiao; Ma, Ying; Zhai, Tianyou. "2D layered group IIIA metal chalcogenides: synthesis, properties and applications in electronics and optoelectronics". *CrystEngComm* 18(2015): 3968-3984.

31. Terhell, Jcjm; Brabers, V. A. M.; Vanegmond, G. E. "Polytype Phase-Transition in The Series $GaSe_{1-x}X_x$". *Journal of Solid State Chemistry* 41(1982): 97-103.

32. Plucinski, L.; Johnson, R. L.; Kowalski, B. J.; Kopalko, K.; Orlowski, B. A.; Kovalyuk, Z. D.; Lashkarev, G. V. "Electronic band structure of GaSe(0001): Angle-resolved photoemission and ab initio theory". *Physical Review B* 68(2003): 125304.

33. Gillan, E. G.; Barron, A. R. "Chemical vapor deposition of hexagonal gallium selenide and telluride films from cubane precursors: Understanding the envelope of molecular control". *Chemistry of Materials* 9(1997): 3037-3048.

34. Yamamoto, Aishi; Syouji, Atsushi; Goto, Takenari; Kulatov, Erkin; Ohno, Kaoru; Kawazoe, Yoshiyuki; Uchida, Kazuhito; Miura, Noboru. "Excitons and band structure of highly anisotropic GaTe single crystals". *Physical Review B* 64(2001): 035210.

35. Cai, Hui; Chen, Bin; Wang, Gang; Soignard, Emmanuel; Khosravi, Afsaneh; Manca, Marco; Marie, Xavier; Chang, Shery L. Y.; Urbaszek, Bernhard; Tongay, Sefaattin. "Synthesis of Highly Anisotropic Semiconducting GaTe Nanomaterials and Emerging Properties Enabled by Epitaxy". *Advanced Materials* 29(2017): 1605551.

36. Rybkovskiy, D. V.; Arutyunyan, N. R.; Orekhov, A. S.; Gromchenko, I. A.; Vorobiev, I. V.; Osadchy, A. V.; Salaev, Yu E.; Baykara, T. K.; Allakhverdiev, K. R.; Obraztsova, E. D. "Size-induced effects in gallium selenide electronic structure: The influence of interlayer interactions". *Physical Review B* 84(2011): 085314.

37. Fan, Y.; Bauer, M.; Kador, L.; Allakhverdiev, K. R.; Salaev, E. Y. "Photoluminescence frequency up-conversion in GaSe single crystals as studied by confocal microscopy". *Journal of Applied Physics* 91(2002): 1081-1086.

38. Lei, Sidong; Ge, Liehui; Liu, Zheng; Najmaei, Sina; Shi, Gang; You, Ge; Lou, Jun; Vajtai, Robert; Ajayan, Pulickel M. "Synthesis and Photoresponse of Large GaSe Atomic Layers". *Nano letters* 13(2013): 2777-2781.

39. Jung, C. S.; Shojaei, F.; Park, K.; Oh, J. Y.; Im, H. S.; Jang, D. M.; Park, J.; Kang, H. S. "Red-to-Ultraviolet Emission Tuning of Two-Dimensional Gallium Sulfide/Selenide". *ACS Nano* 9(2015): 9585-9593.

40. Liu, F. C.; Shimotani, H.; Shang, H.; Kanagasekaran, T.; Zolyomi, V.; Drummond, N.; Fal'ko, V. I.; Tanigaki, K. "High-Sensitivity Photodetectors Based on Multilayer GaTe Flakes". *ACS Nano* 8(2014): 752-760.

41. Mudd, G. W.; Patane, A.; Kudrynskyi, Z. R.; Fay, M. W.; Makarovsky, O.; Eaves, L.; Kovalyuk, Z. D.; Zolyomi, V.; Falko, V. "Quantum confined acceptors and donors in InSe nanosheets". *Applied Physics Letters* 105(2014): 221909.

42. Mudd, G. W.; Svatek, S. A.; Ren, T.; Patane, A.; Makarovsky, O.; Eaves, L.; Beton, P. H.; Kovalyuk, Z. D.; Lashkarev, G. V.; Kudrynskyi, Z. R.; Dmitriev, A. I. "Tuning the Bandgap of Exfoliated InSe Nanosheets by Quantum Confinement". *Advanced Materials* 25(2013): 5714.

43. Late, D. J.; Liu, B.; Matte, Hssr; Rao, C. N. R.; Dravid, V. P. "Rapid Characterization of Ultrathin Layers of Chalcogenides on SiO_2/Si Substrates". *Advanced Functional Materials* 22(2012): 1894-1905.

44. Coleman, J. N.; Lotya, M.; O'Neill, A.; Bergin, S. D.; King, P. J.; Khan, U.; Young, K.; Gaucher, A.; De, S.; Smith, R. J.; Shvets, I. V.; Arora, S. K.; Stanton, G.; Kim, H. Y.; Lee, K.; Kim, G. T.; Duesberg, G. S.; Hallam, T.; Boland, J. J.; Wang, J. J.; Donegan, J. F.; Grunlan, J. C.; Moriarty, G.; Shmeliov, A.; Nicholls, R. J.; Perkins, J. M.; Grieveson, E. M.; Theuwissen, K.; McComb, D. W.; Nellist, P. D.; Nicolosi, V. "Two-Dimensional Nanosheets Produced by Liquid Exfoliation of Layered Materials". *Science* 331(2011): 568-571.

45. Dines, M. B. "Lithium Intercalation via N-Butyllithium of Layered Transition-Metal Dichalcogenides". *Materials Research Bulletin* 10(1975): 287-291.

46. Zeng, Z. Y.; Yin, Z. Y.; Huang, X.; Li, H.; He, Q. Y.; Lu, G.; Boey, F.; Zhang, H. "Single-Layer Semiconducting Nanosheets: High-Yield Preparation and Device Fabrication". *Angewandte Chemie-International Edition* 50(2011): 11093-11097.

47. Zhou, Y. B.; Nie, Y. F.; Liu, Y. J.; Yan, K.; Hong, J. H.; Jin, C. H.; Zhou, Y.; Yin, J. B.; Liu, Z. F.; Peng, H. L. "Epitaxy and Photoresponse of Two-Dimensional GaSe Crystals on Flexible Transparent Mica Sheets". *ACS Nano* 8(2014): 1485-1490.

48. Li, X. F.; Basile, L.; Huang, B.; Ma, C.; Lee, J. W.; Vlassiouk, I. V.; Puretzky, A. A.; Lin, M. W.; Yoon, M.; Chi, M. F.; Idrobo, J. C.; Rouleau, C. M.; Sumpter, B. G.; Geohegan, D. B.; Xiao, K. "Van der Waals Epitaxial Growth of Two-Dimensional Single-Crystalline GaSe Domains on Graphene". *ACS Nano* 9(2015): 8078-8088.

49. Wang, Z. X.; Safdar, M.; Mirza, M.; Xu, K.; Wang, Q. S.; Huang, Y.; Wang, F. M.; Zhan, X. Y.; He, J. "High-performance flexible photodetectors based on GaTe nanosheets". *Nanoscale* 7(2015): 7252-7258.

50. Zhou, Yubing; Nie, Yufeng; Liu, Yujing; Yan, Kai; Hong, Jinhua; Jin, Chuanhong; Zhou, Yu; Yin, Jianbo; Liu, Zhongfan; Peng, Hailin. "Epitaxy and

photoresponse of two-dimensional GaSe crystals on flexible transparent mica sheets". *ACS Nano* 8(2014): 1485-1490.

51. Jie, Wenjing; Hao, Jianhua. Two-Dimensional Layered Gallium Selenide: Preparation, Properties, and Applications. In: *Advanced 2D Materials* (edited by Tiwari, Ashutosh; Syväjärvi, Mikael). John Wiley & Sons, Inc. (2016).

52. Zhuang, Houlong L.; Hennig, Richard G. "Single-Layer Group-III Monochalcogenide Photocatalysts for Water Splitting". *Chemistry of Materials* 25(2013): 3232-3238.

53. Castellanos-Gomez, A.; Roldan, R.; Cappelluti, E.; Buscema, M.; Guinea, F.; van der Zant, H. S. J.; Steele, G. A. "Local Strain Engineering in Atomically Thin MoS_2". *Nano letters* 13(2013): 5361-5366.

54. Wang, C.; Yang, S. X.; Cai, H.; Ataca, C.; Chen, H.; Zhang, X. Z.; Xu, J. J.; Chen, B.; Wu, K. D.; Zhang, H. R.; Liu, L. Q.; Li, J. B.; Grossman, J. C.; Tongay, S.; Liu, Q. "Enhancing light emission efficiency without color change in post-transition metal chalcogenides". *Nanoscale* 8(2016): 5820-5825.

55. Liu, Shanshan; Yuan, Xiang; Wang, Peng; Chen, Zhi-Gang; Tang, Lei; Zhang, Enze; Zhang, Cheng; Liu, Yanwen; Wang, Weiyi; Liu, Cong; Chen, Chen; Zou, Jin; Hu, Weida; Xiu, Faxian. "Controllable Growth of Vertical Heterostructure $GaTe_xSe_{1-x}$/Si by Molecular Beam Epitaxy". *ACS Nano* 9(2015): 8592-8598.

56. Jung, Chan; Park, Kidong; Shojaei, Fazel; Oh, Jin; Im, Hyung; Lee, Jung; Jang, Dong; Park, Jeunghee; Myoung, NoSung; Lee, Chang-Lyoul; Lee, Jong; Song, Jae; Kang, Hong. "Photoluminescence and Photocurrents of $GaS_{1-x}Se_x$ Nanobelts". *Chemistry of Materials* 28(2016): 5811-5820.

57. Srivastava, Ajit; Sidler, Meinrad; Allain, Adrien V.; Lembke, Dominik S.; Kis, Andras; Imamoğlu, A. "Optically active quantum dots in monolayer WSe_2". *Nature Nanotechnology* 10(2015): 491-496.

58. Koperski, M.; Nogajewski, K.; Arora, A.; Cherkez, V.; Mallet, P.; Veuillen, J. Y.; Marcus, J.; Kossacki, P.; Potemski, M. "Single photon emitters in exfoliated WSe_2 structures". *Nature Nanotechnology* 10(2015): 503-506.

59. He, Yu-Ming M.; Clark, Genevieve; Schaibley, John R.; He, Yu; Chen, Ming-Cheng C.; Wei, Yu-Jia J.; Ding, Xing; Zhang, Qiang; Yao, Wang; Xu, Xiaodong; Lu, Chao-Yang Y.; Pan, Jian-Wei W. "Single quantum emitters in monolayer semiconductors". *Nature Nanotechnology* 10(2015): 497-502.

60. Tonndorf, Philipp; Schmidt, Robert; Schneider, Robert; Kern, Johannes; Buscema, Michele; Steele, Gary A.; Castellanos-Gomez, Andres; van der Zant,

Herre S. J.; de Vasconcellos, Steffen; Bratschitsch, Rudolf. "Single-photon emission from localized excitons in an atomically thin semiconductor". *Optica* 2(2015): 347-352.

61. Tonndorf, Philipp; Schwarz, Stefan; Kern, Johannes; Niehues, Iris; Pozo-Zamudio, Osvaldo; Dmitriev, Alexander I.; Bakhtinov, Anatoly P.; Borisenko, Dmitry N.; Kolesnikov, Nikolai N.; Tartakovskii, Alexander I.; de Vasconcellos, Steffen; Bratschitsch, Rudolf. "Single-photon emitters in GaSe". *2D Materials* 4(2017): 21010.

62. Physical Fundamentals of Chemical Vapour Deposition. In: *Chemical Vapour Deposition: An Integrated Engineering Design for Advanced Materials* (edited by Xu, Yongdong; Yan, Xiu-Tian). Springer London (2010).

63. Synthesis Mechanism: Crystal Growth and Nucleation. In: *Zeolites and Catalysis* (edited by Čejka, Jiři; Corma, Avelino; Zones, Stacey). Wiley VCH (2010).

64. Venables, John A. *Introduction to Surface and Thin Film Processes*. Cambridge University Press (2000).

65. Bonds. In: *The Physics of Semiconductors: An Introduction Including Devices and Nanophysics* (edited by Grundmann, Marius). Springer Berlin Heidelberg (2006).

66. Grundmann, Marius. Defects. In: *The Physics of Semiconductors: An Introduction Including Nanophysics and Applications* (edited by Grundmann, Marius). Springer International Publishing (2016).

67. Zhou, Wu; Zou, Xiaolong; Najmaei, Sina; Liu, Zheng; Shi, Yumeng; Kong, Jing; Lou, Jun; Ajayan, Pulickel M.; Yakobson, Boris I.; Idrobo, Juan-Carlos. "Intrinsic Structural Defects in Monolayer Molybdenum Disulfide". *Nano letters* 13(2013): 2615-2622.

68. Tan Chee, Leong; Mohseni, Hooman. "Emerging technologies for high performance infrared detectors". *Nanophotonics* 7(2018): 169.

69. Holder, Aaron M.; Siol, Sebastian; Ndione, Paul F.; Peng, Haowei; Deml, Ann M.; Matthews, Bethany E.; Schelhas, Laura T.; Toney, Michael F.; Gordon, Roy G.; Tumas, William; Perkins, John D.; Ginley, David S.; Gorman, Brian P.; Tate, Janet; Zakutayev, Andriy; Lany, Stephan. "Novel phase diagram behavior and materials design in heterostructural semiconductor alloys". *Science Advances* 3(2017): e1700270.

70. Kuech, Thomas F.; Babcock, Susan E.; Mawst, Luke. "Growth far from equilibrium: Examples from III-V semiconductors". *Applied Physics Reviews* 3(2016): 40801.

71. Blochl, P. E. "Projector Augmented-Wave Method". *Physical Review B* 50(1994): 17953-17979.

72. Perdew, J. P.; Burke, K.; Ernzerhof, M. "Generalized gradient approximation made simple". *Physical Review Letters* 77(1996): 3865-3868.

73. Grimme, S. "Semiempirical GGA-type density functional constructed with a long-range dispersion correction". *Journal of Computational Chemistry* 27(2006): 1787-1799.

74. Kresse, G.; Furthmüller, J. "Efficient iterative schemes for ab initio total-energy calculations using a plane-wave basis set". *Physical Review B* 54(1996): 11169-11186.

75. Zunger, Alex; Wei, S. H.; Ferreira, L. G.; Bernard, James E. "Special quasirandom structures". *Physical Review Letters* 65(1990): 353-356.

76. van de Walle, Axel. "Multicomponent multisublattice alloys, nonconfigurational entropy and other additions to the Alloy Theoretic Automated Toolkit". *Calphad* 33(2009): 266-278.

77. Kresse, G.; Joubert, D. "From ultrasoft pseudopotentials to the projector augmented-wave method". *Physical Review B* 59(1999): 1758-1775.

78. Vinh, L. T.; Eddrief, M.; Sebenne, C.; Sacuto, A.; Balkanski, M. "Heteroepitaxy of GaSe layered semiconductor compound on Si(111) 7 × 7 substrate: a Van der Waals epitaxy?". *Journal of Crystal Growth* 135(1994): 1-10.

79. Zheng, Y.; Koebel, A.; Petroff, J. F.; Boulliard, J. C.; Capelle, B.; Eddrief, M. "GaSe/Si(111) heteroepitaxy: The early stages of growth". *Journal of Crystal Growth* 162(1996): 135-141.

80. Rudolph, R.; Pettenkofer, C.; Bostwick, A. A.; Adams, J. A.; Ohuchi, F.; Olmstead, M. A.; Jaeckel, B.; Klein, A.; Jaegermann, W. "Electronic structure of the Si(111): GaSe van der Waals-like surface termination". *New Journal of Physics* 7(2005): 20.

81. Bauer, E.; Vandermerwe, J. H. "Structure and growth of crystalline superlattices: From monolayer to superlattice". *Physical Review B* 33(1986): 3657-3671.

82. Morin, S. A.; Forticaux, A.; Bierman, M. J.; Jin, S. "Screw Dislocation-Driven Growth of Two-Dimensional Nanoplates". *Nano letters* 11(2011): 4449-4455.

83. Zhuang, A.; Li, J. J.; Wang, Y. C.; Wen, X.; Lin, Y.; Xiang, B.; Wang, X. P.; Zeng, J. "Screw-Dislocation-Driven Bidirectional Spiral Growth of Bi_2Se_3 Nanoplates". *Angewandte Chemie-International Edition* 53(2014): 6425-6429.

84. Burton, W. K.; Cabrera, N.; Frank, F. C. "The growth of crystals and the equilibrium structure of their surfaces". *Philosophical Transactions of the Royal Society of London Series a-Mathematical and Physical Sciences* 243(1951): 299-358.

85. Lu, P.; Wu, X. J.; Guo, W. L.; Zeng, X. C. "Strain-dependent electronic and magnetic properties of MoS2 monolayer, bilayer, nanoribbons and nanotubes". *Physical Chemistry Chemical Physics* 14(2012): 13035-13040.

86. Zhu, C. R.; Wang, G.; Liu, B. L.; Marie, X.; Qiao, X. F.; Zhang, X.; Wu, X. X.; Fan, H.; Tan, P. H.; Amand, T.; Urbaszek, B. "Strain tuning of optical emission energy and polarization in monolayer and bilayer MoS_2". *Physical Review B* 88(2013): 121301(R).

87. Conley, H. J.; Wang, B.; Ziegler, J. I.; Haglund, R. F.; Pantelides, S. T.; Bolotin, K. I. "Bandgap Engineering of Strained Monolayer and Bilayer MoS_2". *Nano letters* 13(2013): 3626-3630.

88. Mohiuddin, T. M. G.; Lombardo, A.; Nair, R. R.; Bonetti, A.; Savini, G.; Jalil, R.; Bonini, N.; Basko, D. M.; Galiotis, C.; Marzari, N.; Novoselov, K. S.; Geim, A. K.; Ferrari, A. C. "Uniaxial strain in graphene by Raman spectroscopy: G peak splitting, Gruneisen parameters, and sample orientation". *Physical Review B* 79(2009): 8.

89. Weinstein, Bernard A.; Piermarini, G. J. "Raman scattering and phonon dispersion in Si and GaP at very high pressure". *Physical Review B* 12(1975): 1172-1186.

90. Franssen, G.; Gorczyca, I.; Suski, T.; Kaminska, A.; Pereiro, J.; Munoz, E.; Iliopoulos, E.; Georgakilas, A.; Che, S. B.; Ishitani, Y.; Yoshikawa, A.; Christensen, N. E.; Svane, A. "Bowing of the band gap pressure coefficient in $In_xGa_{1-x}N$ alloys". *Journal of Applied Physics* 103(2008): 033514.

91. Welber, B.; Cardona, M.; Kim, C. K.; Rodriguez, S. "Dependence of the direct energy gap of GaAs on hydrostatic pressure". *Physical Review B* 12(1975): 5729-5738.

92. Shan, W.; Ager, J. W.; Yu, K. M.; Walukiewicz, W.; Haller, E. E.; Martin, M. C.; McKinney, W. R.; Yang, W. "Dependence of the fundamental band gap of $Al_xGa_{1-x}N$ on alloy composition and pressure". *Journal of Applied Physics* 85(1999): 8505-8507.

93. Jo, M.; Mano, T.; Abbarchi, M.; Kuroda, T.; Sakuma, Y.; Sakoda, K. "Self-Limiting Growth of Hexagonal and Triangular Quantum Dots on (111)A". *Crystal Growth & Design* 12(2012): 1411-1415.

94. Wu, K.; Torun, E.; Sahin, H.; Chen, B.; Fan, X.; Pant, A.; Wright, D. P.; Aoki, T.; Peeters, F. M.; Soignard, E.; Tongay, S. "Unusual lattice vibration characteristics in whiskers of the pseudo-one-dimensional titanium trisulfide TiS_3". *Nature Communications* 7(2016): 12952.

95. Fonseca, Jose J.; Tongay, Sefaattin; Topsakal, Mehmet; Chew, Annabel R.; Lin, Alan J.; Ko, Changhyun; Luce, Alexander V.; Salleo, Alberto; Wu, Junqiao; Dubon, Oscar D. "Bandgap Restructuring of the Layered Semiconductor Gallium Telluride in Air". *Advanced Materials* (2016): 6465-6470.

96. Wang, Z. X.; Xu, K.; Li, Y. C.; Zhan, X. Y.; Safdar, M.; Wang, Q. S.; Wang, F. M.; He, J. "Role of Ga Vacancy on a Multilayer GaTe Phototransistor". *ACS Nano* 8(2014): 4859-4865.

97. Camassel, J.; Merle, P.; Mathieu, H.; Gouskov, A. "Near-band-edge optical properties of $GaSe_xTe_{1-x}$ mixed crystals". *Physical Review B* 19(1979): 1060-1068.

98. Wan, J. Z.; Brebner, J. L.; Leonelli, R.; Graham, J. T. "Optical properties of excitons in GaTe". *Physical Review B* 46(1992): 1468-1471.

99. Varshni, Y. P. "Temperature dependence of the energy gap in semiconductors". *Physica* 34(1967): 149.

100. Wang, W. M.; Lin, A. S.; Phillips, J. D. "Intermediate-band photovoltaic solar cell based on ZnTe:O". *Applied Physics Letters* 95(2009): 011103.

101. Yang, C. Y.; Qin, M. S.; Wang, Y. M.; Wan, D. Y.; Huang, F. Q.; Lin, J. H. "Observation of an Intermediate Band in Sn-doped Chalcopyrites with Wide-spectrum Solar Response". *Scientific Reports* 3(2013): 1286.

102. Aliev, I. A. "GaS-GaSe-GaTe phase diagram". *Russian Journal of Inorganic Chemistry* 53(2008): 1795-1800.

103. Cai, Hui; Soignard, Emmanuel; Ataca, Can; Chen, Bin; Ko, Changhyun; Aoki, Toshihiro; Pant, Anupum; Meng, Xiuqing; Yang, Shengxue; Grossman, Jeffrey;

Ogletree, Frank D.; Tongay, Sefaattin. "Band Engineering by Controlling vdW Epitaxy Growth Mode in 2D Gallium Chalcogenides". *Advanced Materials* 28(2016): 7375-7382.

104. Li, Xufan; Lin, Ming-Wei; Puretzky, Alexander A.; Idrobo, Juan C.; Ma, Cheng; Chi, Miaofang; Yoon, Mina; Rouleau, Christopher M.; Kravchenko, Ivan I.; Geohegan, David B.; Xiao, Kai. "Controlled Vapor Phase Growth of Single Crystalline, Two-Dimensional GaSe Crystals with High Photoresponse". *Scientific Reports* 4(2014): 5497.

105. Zhou, Dawei; Zhou, Yonghui; Pu, Chunying; Chen, Xuliang; Lu, Pengchao; Wang, Xuefei; An, Chao; Zhou, Ying; Miao, Feng; Ho, Ching-Hwa; Sun, Jian; Yang, Zhaorong; Xing, Dingyu. "Pressure-induced metallization and superconducting phase in ReS_2". *npj Quantum Materials* 2(2017): 19.

106. Wu, Chen-Kuang; Nicol, Malcolm. "Raman spectra of high pressure phase and phase transition of polytetrafluoroethylene (teflon)". *Chemical Physics Letters* 21(1973): 153-157.

107. Klee, Velveth; Preciado, Edwin; Barroso, David; Nguyen, Ariana E.; Lee, Chris; Erickson, Kristopher J.; Triplett, Mark; Davis, Brandon; Lu, I. Hsi; Bobek, Sarah; McKinley, Jessica; Martinez, Joseph P.; Mann, John; Talin, A. Alec; Bartels, Ludwig; Léonard, François. "Superlinear Composition-Dependent Photocurrent in CVD-Grown Monolayer $MoS_{2(1-x)}Se_{2x}$ Alloy Devices". *Nano letters* 15(2015): 2612-2619.

108. Duan, Xidong; Wang, Chen; Fan, Zheng; Hao, Guolin; Kou, Liangzhi; Halim, Udayabagya; Li, Honglai; Wu, Xueping; Wang, Yicheng; Jiang, Jianhui; Pan, Anlian; Huang, Yu; Yu, Ruqin; Duan, Xiangfeng. "Synthesis of $WS_{2x}Se_{2-2x}$ Alloy Nanosheets with Composition-Tunable Electronic Properties". *Nano letters* 16(2016): 264-269.

109. Zhang, Wenting; Li, Xiaodong; Jiang, Tongtong; Song, Jiangluqi; Lin, Yue; Zhu, Lixin; Xu, Xiaoliang. "CVD synthesis of $Mo_{(1-x)}W_xS_2$ and $MoS_{2(1-x)}Se_{2x}$ alloy monolayers aimed at tuning the bandgap of molybdenum disulfide". *Nanoscale* 7(2015): 13554-13560.

110. Li, Xufan; Basile, Leonardo; Huang, Bing; Ma, Cheng; Lee, Jaekwang; Vlassiouk, Ivan V.; Puretzky, Alexander A.; Lin, Ming-Wei; Yoon, Mina; Chi, Miaofang; Idrobo, Juan C.; Rouleau, Christopher M.; Sumpter, Bobby G.; Geohegan, David B.; Xiao, Kai. "Van der Waals Epitaxial Growth of Two-Dimensional Single-Crystalline GaSe Domains on Graphene". *ACS Nano* 9(2015): 8078-8088.

111. Wu, Kedi; Chen, Bin; Yang, Sijie; Wang, Gang; Kong, Wilson; Cai, Hui; Aoki, Toshihiro; Soignard, Emmanuel; Marie, Xavier; Yano, Aliya; Suslu, Aslihan; Urbaszek, Bernhard; Tongay, Sefaattin. "Domain Architectures and Grain Boundaries in Chemical Vapor Deposited Highly Anisotropic ReS_2 Monolayer Films". *Nano letters* 16(2016): 5888-5894.

112. Island, Joshua O.; Biele, Robert; Barawi, Mariam; Clamagirand, José M.; Ares, José R.; Sánchez, Carlos; van der Zant, Herre S. J.; Ferrer, Isabel J.; D'Agosta, Roberto; Castellanos-Gomez, Andres. "Titanium trisulfide (TiS_3): a 2D semiconductor with quasi-1D optical and electronic properties". *Scientific Reports* 6(2016): 22214.

113. Huang, Shengxi; Tatsumi, Yuki; Ling, Xi; Guo, Huaihong; Wang, Ziqiang; Watson, Garrett; Puretzky, Alexander A; Geohegan, David B; Kong, Jing; Li, Ju. "In-Plane Optical Anisotropy of Layered Gallium Telluride". *ACS Nano* (2016):

114. Ling, Xi; Wang, Han; Huang, Shengxi; Xia, Fengnian; Dresselhaus, Mildred S. "The renaissance of black phosphorus". *Proceedings of the National Academy of Sciences* 112(2015): 4523-4530.

115. Pant, Anupum; Torun, Engin; Chen, Bin; Bhat, Soumya; Fan, Xi; Wu, Kedi; Wright, David P.; Peeters, Francois M.; Soignard, Emmanuel; Sahin, Hasan; Tongay, Sefaattin. "Strong dichroic emission in the pseudo one dimensional material ZrS_3". *Nanoscale* 8(2016): 16259-16265.

116. Wang, Xiaomu; Jones, Aaron M.; Seyler, Kyle L.; Tran, Vy; Jia, Yichen; Zhao, Huan; Wang, Han; Yang, Li; Xu, Xiaodong; Xia, Fengnian. "Highly anisotropic and robust excitons in monolayer black phosphorus". *Nature Nanotechnology* 10(2015): 517.

117. Aslan, Ozgur Burak; Chenet, Daniel A.; van der Zande, Arend M.; Hone, James C.; Heinz, Tony F. "Linearly Polarized Excitons in Single- and Few-Layer ReS_2 Crystals". *ACS Photonics* 3(2016): 96-101.

118. Lee, Sangwook; Yang, Fan; Suh, Joonki; Yang, Sijie; Lee, Yeonbae; Li, Guo; Sung Choe, Hwan; Suslu, Aslihan; Chen, Yabin; Ko, Changhyun; Park, Joonsuk; Liu, Kai; Li, Jingbo; Hippalgaonkar, Kedar; Urban, Jeffrey J.; Tongay, Sefaattin; Wu, Junqiao. "Anisotropic in-plane thermal conductivity of black phosphorus nanoribbons at temperatures higher than 100 K". *Nature Communications* 6(2015): 8573.

119. Liu, Huifang; Chang, Luke L. Y. "Phase relations in systems of tin chalcogenides". *Journal of Alloys and Compounds* 185(1992): 183-190.